

[15] Matsumura, M., *Kagaku Kogaku Ronbunshu*, Vol. 2, No. 4, 1976, pp. 399-404.

[16] Knapp, R. T., Daily, J. W., and Hammitt, F. G., *Cavitation*, McGraw-Hill, New York, 1970, p. 43.

DISCUSSION

*F. G. Hammitt*¹ (*written discussion*)—This paper is of special interest because of the comparison between flowing system venturi cavitation damage results and vibratory results, particularly with regard to the "characteristic curves" of time-versus-volume loss rate. However, it would be helpful to the reader not familiar with the Erdmann-Jesnitzer work in Hannover, Germany, where this work was accomplished, if at least a schematic of the flow path geometry used were included.

It would also be helpful, in applying and interpreting the results, if a table were included providing full mechanical property data on the materials tested. Incidentally, in this regard, what specifically is the material NGCI? As a nonmetallurgist, I at least am not familiar with that designation.

Masanobu Matsumura (*author's closure*)—The author is grateful to Professor Hammitt for his kind comments. A schematic of the chamber used for the flow cavitation erosion tests is shown in Fig. 16. Fuller details may be found in Refs 10 and 11.

The mechanical properties of the materials used in the vibratory tests are listed in Table 3. The NGCI used in the flow cavitation erosion tests consists of nearly the same chemical composition as the cast iron in Table 3 except

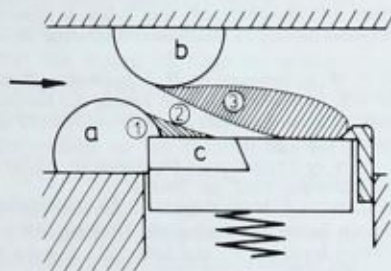


FIG. 16—Schematic diagram of chamber for flow cavitation erosion test. (a) and (b) barriades; (c) test specimen; (1) and (3) stream of bubbles; (2) liquid, devoid of bubbles.

¹Professor of mechanical engineering, University of Michigan, Ann Arbor, Mich. 48109.

TABLE 3—Mechanical properties of specimens.

	Lower Yield Point, MN/m ²	Upper Yield Point, MN/m ²	Tensile Strength, MN/m ²	Elongation, %	Reduction of Area, %	Hv, kg/mm ²
Iron (ferrite)	160	...	283	59.0	78.0	108
Mild steel	326	331	462	35.5	66.9	146
Tool steel	365	371	734	21.7	27.5	229
Cast iron	212	0.5	0.7	171
Stainless steel	667	64.7	73.2	195
Brass	391	15.2	29.1	144
Aluminum	61.4	58.0	92.9	94

Effect of an Air-Injected Shroud on the Breakup Length of a High-Velocity Waterjet

REFERENCE: Eddingfield, D. L. and Albrecht, M., "Effect of an Air-Injected Shroud on the Breakup Length of a High-Velocity Waterjet," *Erosion: Prevention and Useful Applications*, ASTM STP 664, W. F. Adler, Ed., American Society for Testing and Materials, 1979, pp. 461-472.

ABSTRACT: Air-injected shrouds are used to create an airflow parallel to a high-speed waterjet to examine the effect of the air velocity on the breakup length of the waterjet. Eight shrouds having four different lengths and two different diameters are employed in this study. The air velocity was varied from zero to approximately twice the velocity of the waterjet. The waterjet has an exit diameter of 0.766 mm (0.030 in.) and an exit velocity of 266 m/s (874 ft/s) for all the experimental runs.

Of the shrouds tested, the shortest shroud with the smaller diameter produced the best results for the entire air velocity ranges. The breakup length of the waterjet with a shroud compared to that of a waterjet without a shroud ranges from 1.2 for an air-to-water velocity ratio of zero up to a value of approximately 1.7 for a velocity ratio of 2.0.

Cutting tests on a representative material are planned to establish firmly the benefit of utilizing an air-injected shroud in conjunction with a high-velocity waterjet.

KEY WORDS: waterjet, coaxial jets, breakup length, coherent length, standoff distance, erosion

The ability to cut or fragment materials using high-speed waterjets at relatively large standoff distances is desirable for many applications, for example, borehole mining of coal and other minerals. In such cases, the task is usually one of maximizing the effective cutting length of the jet for a given nozzle design and given operating pressure.

There exists an extensive amount of reported work in the literature dealing with nozzle design and operating characteristics. Summers and Zakin² give a

¹ Assistant professor and graduate student, respectively, Engineering Mechanics and Materials Department, Southern Illinois University, Carbondale, Ill. 62901.

² Summers, D. A. and Zakin, J. L., "The Structure of High Speed Fluid Jets and Their Use in Cutting Various Soil and Material Types," Final Report, USAMERDC Contract No. DAAK02-74-C-0006, Rock Mechanics and Explosives Research Center, University of Missouri-Rolla, Rolla, Mo.

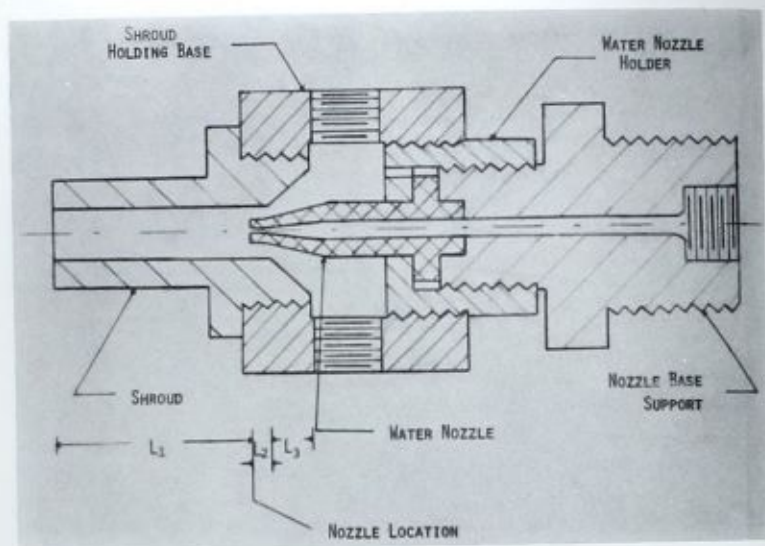


FIG. 2—Water jet nozzle, shroud mounting base, and shroud assembly.

percent of the shroud cross-sectional area for the 4.75-mm-diameter (0.1875 in.) shroud and 0.64 percent for the 9.52-mm-diameter (0.375 in.) shroud, it is felt that this assumption is justified.

The air velocity values vary from 0 to 450 m/s (1476 ft/s) but the waterjet velocity is held constant at a value of 266 m/s (872 ft/s) for all the experimental runs.

For each air shroud and each value of the air velocity, a minimum of three photographs is taken with a 35-mm camera. The camera is positioned so that the field of view is from approximately 5.08 to 43.18 cm (2 to 17 in.) downstream of the waterjet nozzle. Diffused backlighting is employed using two slaved strobes which provide a high-intensity flash of duration 8.0 μ s.

The photographs are analyzed to determine the downstream location at which the coherent core of the waterjet can no longer be detected. The values determined from the three photographs for each test condition are averaged to give the breakup length of the waterjet, $L_{b,r}$.

Results and Discussion

The results of the experimental runs are plotted in Figs. 3 and 4. $L_{b,i}/L_{b,r}$ represents the ratio of the measured breakup length of the waterjet with an air-injected shroud to a reference breakup length. The reference breakup length $L_{b,r}$ is defined as the measured breakup length of the waterjet without

TABLE 1—Air-injected shroud dimensions (refer to Fig. 2 for notations).

Shroud No.	Inside Diameter,		L_1 ,		L_2 ,		L_3 ,	
	mm	(in.)	mm	(in.)	mm	(in.)	mm	(in.)
1A	{ 9.53	{ (0.375)	8.46	(0.333)	{ 2.67	{ (0.105)	{ 7.93	{ (0.312)
2A			38.63	(0.375)				
3A			76.73	(3.02)				
4A			144.83	(4.52)				
1B	{ 4.76	{ (0.188)	8.46	(0.333)	{ }	{ -0	{ 10.90	{ (0.429)
2B			38.63	(1.52)				
3B			76.73	(3.02)				
4B			144.83	(4.52)				

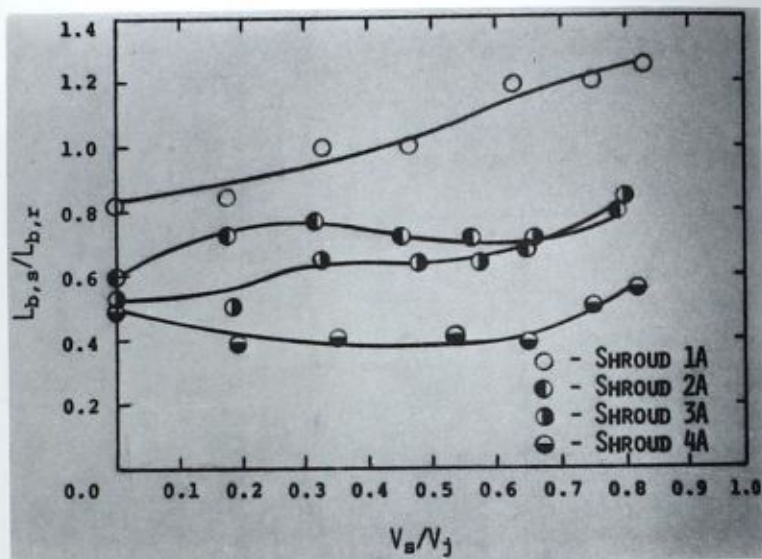


FIG. 3—Breakup length ratio versus air-to-water velocity ratio for four shroud lengths. Shroud diameter = 9.52 mm.

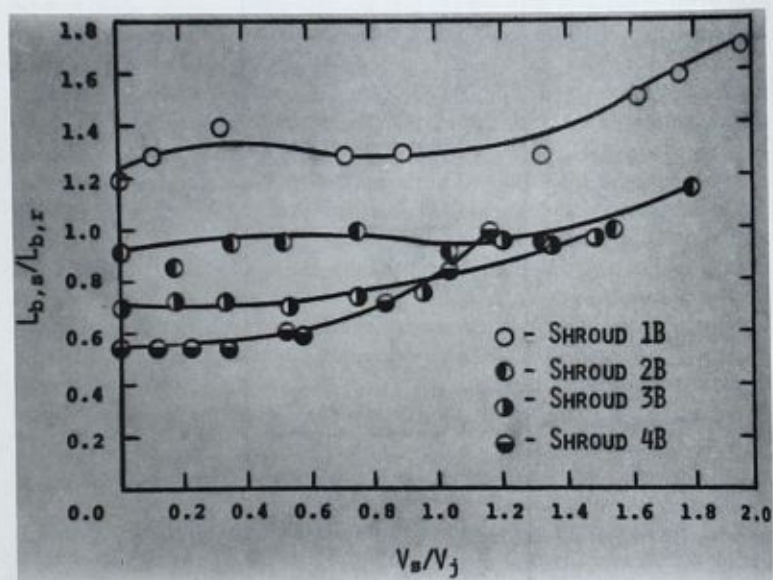


FIG. 4—Breakup length ratio versus air-to-water velocity ratio for four shroud lengths. Shroud diameter = 4.76 mm.

a shroud. $L_{b,r}$ is measured from the exit plane of the nozzle, whereas $L_{b,s}$ is measured from the exit plane of the shroud. Thus, in each case, the breakup length is measured from the position of zero standoff distance. Note that an improvement in the breakup length is indicated when the value of the ratio $L_{b,s}/L_{b,r}$ exceeds one. V_s/V_j represents the ratio of the velocity of the air in the shroud to the velocity of the waterjet at the exit plane of the nozzle. Both $L_{b,r}$ and V_j are constant for all the data collected. $L_{b,r}$ for the waterjet is 140 nozzle diameters.

The data for $V_s/V_j = 0$ are slightly misleading and require an explanation. These data are for the case where no external air supply was connected to the shroud. Consequently the airflow in the shroud is being aspirated by the water flow and the velocity is nonzero but probably very low.

Representative photographs of the waterjet are presented in Figs. 5a-5i. Due to space limitations, only photographs showing the highest relative velocity ratio are presented.

For both series of shrouds, the figures show that the shortest shroud length gives the best results. In Series A, an improvement in the breakup length results for a velocity ratio greater than approximately 0.5. In Series B, the improvement is noted for all values of the velocity ratio.

For Series A, all the shrouds yield a relative breakup length less than one with the singular exception of Shroud 1A, which gives an improvement in the relative breakup length for values of V_s/V_j greater than 0.5, as mentioned previously. Little significance should be given to the crossing of the curves for Shrouds 2A and 3A. This may be due to some extraneous conditions present in these particular experimental runs which altered the jet structure of Shroud 2A to produce lower values of the relative breakup length for the three highest values of the velocity ratio. This is only speculation, however, which must be confirmed by further tests.

For Series B, with the exception of the longest shroud, 4B, the breakup length is insensitive to the velocity ratio up to a value of approximately one. It is interesting to note that for the shortest shroud, 1B, the relative breakup length increases approximately 20 percent even for the case of an aspirating shroud. The rapid increase in the breakup length of Shroud 4B cannot be explained at this time. Unfortunately, the maximum value of the velocity ratio obtainable with this shroud is approximately 1.2 due to the maximum pressure limitations of the compressed-air supply.

One effect of the air-injected shroud is to produce a spray plume surrounding the coherent core which is dispersed more radially but less densely than the plume of the waterjet without a shroud. Alpinieri⁴ found in his experiments with coaxial jets of an inner carbon dioxide jet and an outer airjet that the larger the velocity of the outer jet with respect to that of the inner jet,

⁴Alpinieri, L. J., *American Institute of Aeronautics and Astronautics Journal*, Vol. 2, No. 9, Sept., 1964, pp. 1560-1567.

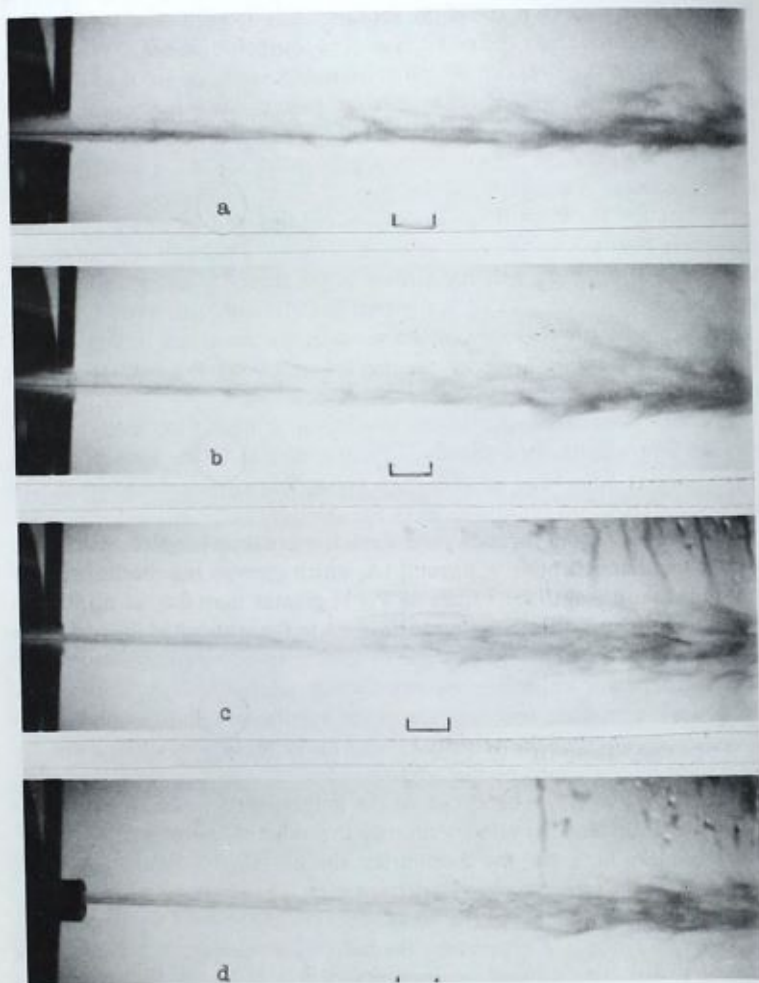


FIG. 5—Photographs of water-jet $V_j = 266$ m/s. The scale indicates a 2-cm length. (a) Water-jet without Shroud (5 cm downstream from nozzle exit). (b) Water-jet with Shroud 1A, $V_s = 224$ m/s (4.4 cm downstream from shroud exit). (c) Water-jet with Shroud 2A, $V_s = 210$ m/s (0.8 cm downstream from shroud exit). (d) Water-jet with Shroud 3A, $V_s = 213$ m/s (shroud exit is shown). (e) Water-jet with Shroud 4A, $V_s = 717$ m/s (shroud exit is shown). (f) Water-jet with Shroud 1B, $V_s = 524$ m/s (3.5 cm downstream from shroud exit). (g) Water-jet with Shroud 2B, $V_s = 477$ m/s (2.3 cm downstream from shroud exit). (h) Water-jet with Shroud 3B, $V_s = 395$ m/s (shroud exit is shown). (i) Water-jet with Shroud 4B, $V_s = 311$ m/s (shroud exit is shown).

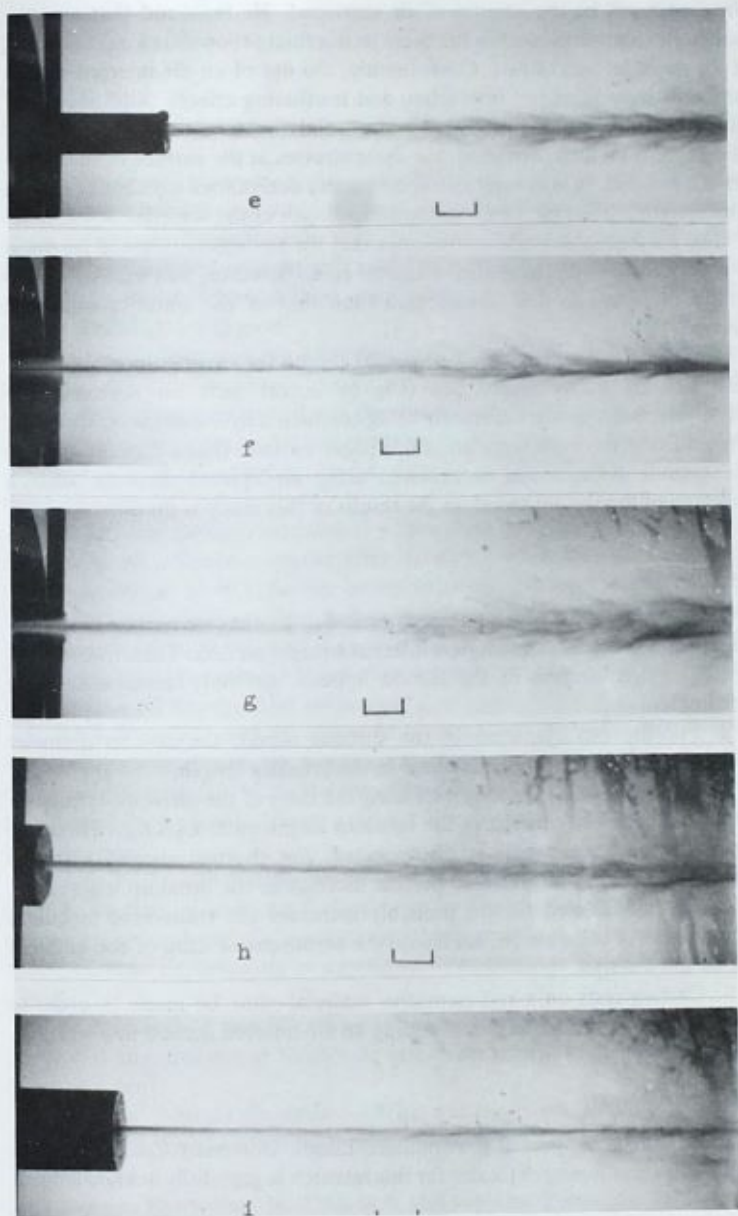


FIG. 5—Continued

the larger will be the amount of air entrained. He reasoned that any turbulent fluctuation present in the outer jet is a fluctuation that would not exist if the outer jet was at rest. Consequently, the use of an air-injected shroud probably introduces two interacting and conflicting effects. Additional turbulent fluctuations are introduced in the radial direction which act to disrupt the jet, but, on the other hand, the shear stresses at the surface of the waterjet are reduced. Which mechanism dominates determines whether or not the air-injected shroud increases the breakup length of the waterjet.

The photographic evidence indicates that the air-injected shroud produces a waterjet which has a smaller-diameter core. However, this smaller core is found to persist farther downstream than that of the waterjet without a shroud.

The benefit of utilizing an air-injected shroud for cutting and fragmentation can be firmly established only by actual tests on representative materials. Such tests are currently being conducted by the authors. However, the results of the work reported in this paper indicate that a modest increase in standoff distance can be achieved using air-injected shrouds. Also, a redesign of the shroud based on the results of this study is planned.

Conclusions

1. In general, the breakup length ratio $L_{b,s}/L_{b,r}$ has its largest values for the shroud which has the shortest internal straight section. Therefore, the internal straight section of the shroud appears not only unnecessary, but detrimental.

2. For the two diameters of the shrouds tested, the smaller-diameter shroud produces the largest increase in the breakup length.

3. For the shortest shroud, increasing the ratio of the air velocity relative to the water velocity increases the breakup length ratio $L_{b,s}/L_{b,r}$. However, even when the air supply is disconnected, the shortest shroud with the smaller diameter produces a 20 percent increase in the breakup length.

4. The air-injected shroud probably increases the transverse turbulent fluctuations of the waterjet but delays the aerodynamic drag of the ambient air on the waterjet.

5. Cutting tests on a representative material must be made in order to firmly establish the usefulness of adding an air-injected shroud to a waterjet.

Acknowledgments

The financial support of the Southern Illinois University Coal Extraction and Utilization Research Center for this research is gratefully acknowledged.

DISCUSSION

*F. J. Heymann*¹ (*written discussion*)—Why is your air shroud nozzle designed with a conical instead of rounded entry? Do you deliberately want to create a vena contracta smaller than the shroud diameter? One difference between the short and long shrouds might then be that for the longer ones the airjet reattaches and for the short one it does not, resulting in an effectively smaller-diameter air shroud.

D. L. Eddingfield and M. Albrecht (*authors' closure*)—The conical cross section of the air shroud was chosen for ease of machining. Because these were the initial experiments, it was the simplest geometry to use even though the best cross-sectional shape will probably be of a more streamlined shape.

Your comment about reattachment of the airjet is pertinent and bears further investigation.

*B. P. Selberg*² (*written discussion*)—Your data indicates that the greatest increase in jet coherence occurs after the shrouded airflow chokes. Once choking occurs at $M = 1$, further increases in stagnation pressure will cause both a favorable shear gradient and an increase in the air exit pressure. This increased air pressure will tend to confine the jet. Do you have a physical feeling as to whether the velocity shear effect or the pressure effect is dominating in the measured improved jet coherence?

D. L. Eddingfield and M. Albrecht (*authors' closure*)—By speculation, the velocity shear effect is the dominant mechanism. Note that Shroud 1B for the aspirating case ($V_s/V_j = 0$) gave approximately 20 percent improvement over that of the waterjet without a shroud. For this case, the air exit pressure is atmospheric.

*J. P. Barber*³ (*written discussion*)—The basic premise of your program appears to be that jet breakup is dominated by Helmholtz instabilities. Have you done any analyses of Helmholtz instability growth in waterjets? Are the results of your experiments in agreement with classical Helmholtz predictions?

D. L. Eddingfield and M. Albrecht (*authors' closure*)—No, we have not performed any analyses of Helmholtz instability growth in conjunction with our experiments.

*A. F. Conn*⁴ (*written discussion*)—What was the length, in terms of nozzle diameters, for your baseline jet breakup distance?

¹Westinghouse Electric Corp., P. O. Box 9175, Mail Stop A204, Philadelphia, Pa. 19113.

²University of Missouri-Rolla, Mechanical and Aerospace Engineering, Rolla, Mo. 65401.

³University of Dayton, Research Institute, 300 College Park Ave., Dayton, Ohio 45469.

⁴Hydronautics, Inc., Pindell School Road, Laurel, Md. 20810.

D. L. Eddingfield and M. Albrecht (authors' closure)—Approximately 140 diameters.

A. Lichtarowicz⁵ (written discussion)—Looking at your Fig. 4 showing the effect of a small-diameter shroud on the velocity ratio, it appears that the increased effectiveness of the shortest shroud starts to rise at the point where the airflow becomes sonic. Is this so?

I would be interested in seeing your result when the airflow becomes supersonic. The nozzle arrangement as shown in Fig. 2 indicates that you have a rather crude convergent-divergent nozzle.

D. L. Eddingfield and M. Albrecht (authors' closure)—Yes, this is true. We are currently pursuing further studies with a supersonic air shroud.

P. D. Lohn⁶ (written discussion)—With regard to the possibility of supersonic effects: the air-water interface is a two-phase region where the sound speed may be extremely small. Supersonic effects must be suspected on the edge of any waterjet in air whether or not the jet is shrouded.

⁵University of Nottingham, University Park, Nottingham, U. K. NG7 2RD.

⁶TRW System and Energy, Inc., Redondo Beach, Calif. 90278.

Adaptation of Jet Accumulation Techniques for Enhanced Rock Cutting

REFERENCE: Mazurkiewicz, M., Barker, C. R., and Summers, D. A., "Adaptation of Jet Accumulation Techniques for Enhanced Rock Cutting," *Erosion: Prevention and Useful Applications*, ASTM STP 664, W. F. Adler, Ed., American Society for Testing and Materials, 1979, pp. 473-492.

ABSTRACT: The velocity of a waterjet can be increased when the jet impacts a target material or another waterjet. A theory describing such augmentation in terms of velocity, mass, and energy change is considered. The phenomenon is sensitive to jet structure and the jet velocity profile. Jet velocity profiles do not remain constant over great distances from the nozzle, and ultimately disrupt into droplets. Within the droplet the profile is more regular and the velocity constant. The theory is extended to cover the case of droplet collisions, and experimental evidence of jet augmentation and its effects is presented.

KEY WORDS: impact pressure distribution, fluid jet augmentation, droplet impact, erosion, rock, converging nozzle

The use of the high-pressure waterjet as a cutting tool has, within the past five years, become a commercial reality. The range of application has covered a spectrum from cardboard and wood through coal and rubber to metal.

Research investigators have carried out test programs at pressure levels up to 40 kbar, well above the 2.5 to 4 kbar level of commercially available equipment. Such research has shown that under certain circumstances, there can be benefits to working at these higher pressures. Equipment for this type of work is, however, generally only of the "one-of-a-kind" research tool variety, and results of test findings at the higher pressure levels have indicated relatively short lives for the generating pressure systems and particularly the nozzles in which the transition to cutting speed occurs.

¹Assistant professor, Instytut Technologii Budowy Maszyn, Politechnika Wroclawska, Poland.

²Senior investigator and director, respectively, Rock Mechanics and Explosives Research Center, University of Missouri-Rolla, Rolla, Mo.

Because of the problems associated with creating pressures within a piece of equipment, consideration has turned to the possibility of generating high velocities beyond the nozzle by the use of interacting jets or jet impact on a solid surface.

This approach has already proved successful in the development of shaped charges, particularly for military applications during World War II [1-3].³ Theoretical and experimental analysis of this phenomenon has shown that directional cumulative jet accelerations to velocities of the order of 1000 to 2500 m/s can be achieved. The velocity achieved is a function of the charge size and the shape and material composition of the liner which, upon collapse, will create the cutting jet.

This paper examines the related field where an augmented velocity jet or "fast jet" is produced by the impact between two identical waterjets or of a single waterjet with a rigid flat surface. The paper extends the existing theory developed for shaped explosive charges to describe the formation and nature of the secondary waterjets formed when two identical jets meet. The secondary jets move in opposing directions along the line bisecting the angle between the original jets. The motion of the secondary jets must satisfy the principles of conservation of mass, energy, and momentum. Calculations are thereupon described which govern the mass and velocity of these secondary jets.

Particular considerations are given to the case where one of the secondary jets is of sufficient velocity to have the capability of cutting a target material.

In the passage of a waterjet from the nozzle into a surrounding fluid, the effect on the jet of the surrounding fluid is to cause a change in the pressure profile (velocity profile) of the jet (Fig. 1). The initial condition with a constant velocity across the profile changes to a Gaussian distribution with increasing distance from the nozzle as the water on the outside of the core is removed. The initial analysis is based on those portions of the curve where the primary jet still retains a constant velocity across the profile, and finally the case where the jet is broken into droplets is considered.

Analytical Model

Consider an original primary fluid jet in the region close to the nozzle where it retains an even pressure profile across its section. Let such a jet have a square cross section of area $b \times b$ with a leading edge which is a flat surface, and consider the initial stages of impact. If it is assumed that all portions of the original jet are approaching a rigid flat surface with the same velocity vector inclined at angle α relative to the flat surface and with the leading edge of the primary jet inclined at angle γ to plane A_1A_2 , the first portion of the leading edge of the primary jet will contact the plane 00 at

³The italic numbers in brackets refer to the list of references appended to this paper.

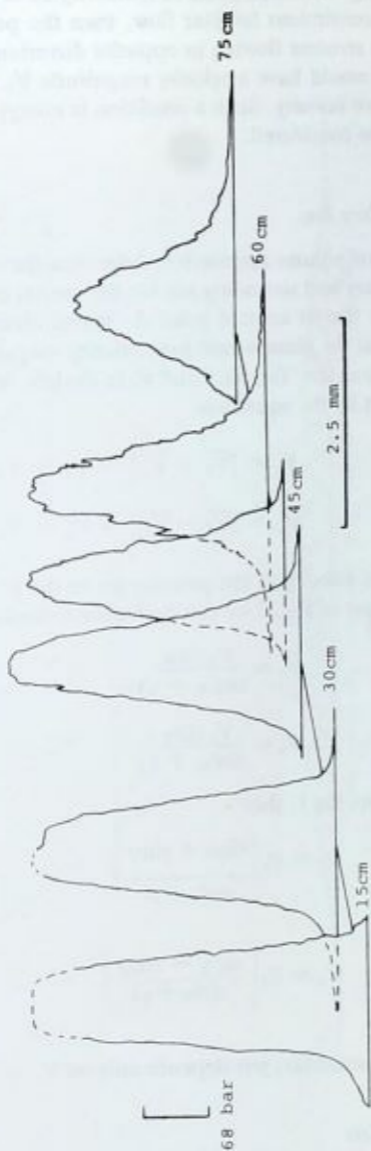


FIG. 1—Impact pressure profiles at various distances along a waterjet issuing from a 1.5-mm nozzle diameter at 545 bar.

Point A_1 (Fig. 2). This simulation is equivalent to the intersection of two similar jets approaching a common plane of symmetry 00 at angle γ (Fig. 3).

If the flow were a continuous laminar flow, then the primary jet would divide to produce two streams flowing in opposite directions along the surface 00 . Each stream would have a velocity magnitude V_o , where V_o is the magnitude of the inflow velocity. Such a condition is nontypical and a more generalized case will be considered.

Velocity of the Secondary Jets

Sims [4] used a control volume approach to determine the velocity relationship between the primary and secondary jets for the special case $\gamma = 90$ deg. He concluded that, as the jet contact point A_1 moves along plane 00 at a speed V_A , jets created at the plane would have velocity magnitudes (V_{ff} to the right, herein referred to as the "fast jet," and V_{sj} to the left, herein referred to as the "slow jet") given by the equations

$$V_{ff} = |\bar{V}_R + \bar{V}_A| = V_R + V_A \quad (1)$$

$$V_{sj} = |\bar{V}_A - \bar{V}_R| = V_A - V_R$$

where V_R is the relative velocity of the primary jet to the jet contact point. From the velocity polygon in Fig. 2 we can derive the following

$$V_R = \frac{V_o \sin \alpha}{\sin(\alpha + \gamma)} \quad (2)$$

$$V_A = \frac{V_o \sin \gamma}{\sin(\alpha + \gamma)}$$

If Eq 2 is substituted into Eq 1, then

$$V_{ff} = V_o \left[\frac{\sin \alpha + \sin \gamma}{\sin(\alpha + \gamma)} \right] \quad (3)$$

$$V_{sj} = V_o \left[\frac{\sin \gamma - \sin \alpha}{\sin(\alpha + \gamma)} \right] \quad (4)$$

Hence, the speed of the secondary jets depends only on V_o , α , and γ .

Mass of the Secondary Jets

The mass of the secondary waterjets can be estimated by applying the equations for conservation of momentum and mass at Point A_1 (Fig. 2)

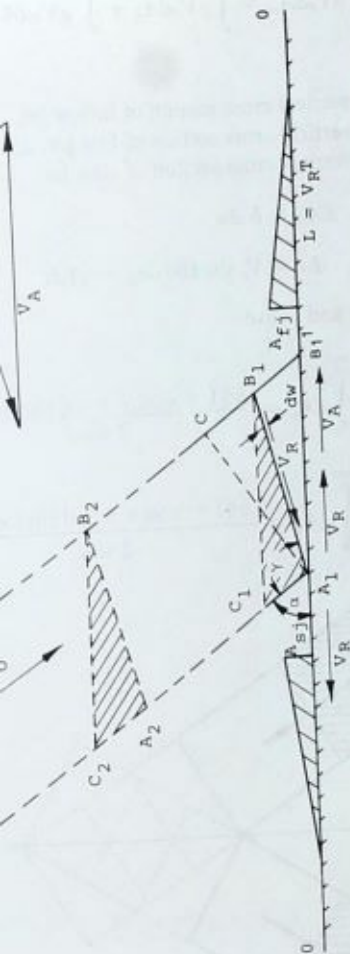


FIG. 2—Geometric representation of the stages of impact of a flat-faced waterjet on an oblique plane.

$$\int \rho V_R^2 \cos[180 \text{ deg} - (\alpha + \gamma)] dA_{in} = - \int \rho V_R^2 dA_{fj} + \int \rho V_R^2 dA_{sj}$$

and

$$\int \rho V_R dA_{in} = \int \rho V_R dA_{fj} + \int \rho V_R dA_{sj}$$

where

dA_{in} = elemental vertical cross section of inflow jet,

dA_{fj} = elemental vertical cross section of fast jet, and

dA_{sj} = elemental vertical cross section of slow jet.

$$dA_{in} = b dw$$

$$dw = V_o \sin(180 \text{ deg} - \gamma) dt$$

substituted into Eqs 5 and 6 give

$$(A_{fj})_{\max} = \int_0^{\max} dA_{fj} = \frac{b^2[1 + \cos(\alpha + \gamma)] \sin(\alpha + \gamma)}{2 \sin \alpha}$$

$$(A_{sj})_{\max} = \int_0^{\max} dA_{sj} = \frac{b^2[1 - \cos(\alpha + \gamma)] \sin(\alpha + \gamma)}{2 \sin \alpha}$$

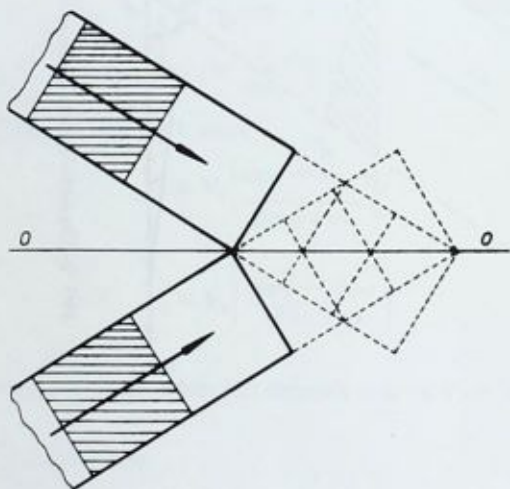


FIG. 3—Collision of two flat-faced square jets.

The area of the vertical cross section of the secondary waterjet impacting on the surface increases linearly from 0 to the value $(A_{\beta})_{\max}$. This occurs during the time T that Point B_1 moves to B_1' . If we let distance B_1B_1' be x and consider triangles A_1CB_1 and $A_1B_1B_1'$, then

$$T = \frac{x}{V_o} = \frac{b \sin(\alpha + \gamma)}{V_o \sin \alpha \sin \gamma} \quad (9)$$

The length of the secondary jet is therefore

$$l = V_R T \quad (10)$$

From Eqs 2 and 9 this gives

$$l = \frac{b}{\sin \gamma} \quad (11)$$

Secondary jets will have a wedge shape with an area of the base of $(A_{\beta})_{\max}$ and $(A_{\gamma})_{\max}$, width b , and length l . Letting the mass density of the water be ρ , the mass of the secondary jets will be

$$(M_{\beta})_{\max} = \frac{\rho b^3 [1 + \cos(\alpha + \gamma)] \sin(\alpha + \gamma)}{4 \sin \alpha \sin \gamma} \quad (12)$$

$$(M_{\gamma})_{\max} = \frac{\rho b^3 [1 - \cos(\alpha + \gamma)] \sin(\alpha + \gamma)}{4 \sin \alpha \sin \gamma}$$

The total mass that participates in the formation of the secondary waterjets is the sum of $(M_{\beta})_{\max}$ plus $(M_{\gamma})_{\max}$

$$M_{in} = \frac{\rho b^3 \sin(\alpha + \gamma)}{2 \sin \alpha \sin \gamma} \quad (13)$$

Energy of the Secondary Jets

Using Eqs 3, 4, and 12, the kinetic energy of the secondary waterjets can be derived

$$EK_{\beta} = \frac{\rho b^3 V_o^2}{8} \frac{[1 + \cos(\alpha + \gamma)] (\sin \alpha + \sin \gamma)^2}{\sin \alpha \sin \gamma \sin(\alpha + \gamma)} \quad (14)$$

$$EK_{\gamma} = \frac{\rho b^3 V_o^2}{8} \frac{[1 - \cos(\alpha + \gamma)] (\sin \alpha + \sin \gamma)^2}{\sin \alpha \sin \gamma \sin(\alpha + \gamma)}$$

The kinetic energy of the secondary jets is a function of V_o , b , and angles α and γ .

Concentration of Energy

Even more significant than the energy ratio is the concentration of energy. This information, important in estimating the cutting potential of the secondary jets, is obtained by dividing the kinetic energy by the cross-sectional area of the secondary jets. Hence

$$K_{\beta} = \frac{EK_{\beta}}{(A_{\beta})_{\max}} = \frac{\rho b V_o^2}{4} \frac{(\sin \alpha + \sin \gamma)^2}{\sin \gamma \sin^2(\alpha + \gamma)} \quad (15)$$

$$K_{\gamma} = \frac{EK_{\gamma}}{(A_{\gamma})_{\max}} = \frac{\rho b V_o^2}{4} \frac{(\sin \alpha - \sin \gamma)^2}{\sin \gamma \sin^2(\alpha + \gamma)}$$

The concentration of energy for the primary jet can be written as

$$K_{in} = \frac{EK_{in}}{A_{in}} = \frac{\rho b V_o^2}{4} \frac{\sin(\alpha + \gamma)}{\sin \alpha \sin \gamma} \quad (16)$$

where $A_{in} = b^2$, the area of the cross section of the primary jet. The concentration of energy ratio is then obtained from Eqs (15) and (16) as

$$\frac{K_{\beta}}{K_{in}} = \frac{(\sin \alpha + \sin \gamma)^2 \sin \alpha}{\sin^3(\alpha + \gamma)} \quad (17)$$

$$\frac{K_{\gamma}}{K_{in}} = \frac{(\sin \alpha - \sin \gamma)^2 \sin \alpha}{\sin^3(\alpha + \gamma)}$$

Analysis of the Theoretical Results

It is obvious from studying the foregoing equations that the values of α and γ are very important in determining the characteristics of the secondary jets. Figure 4 was computed by dividing Eq (3) by V_o . Note that the actual value of α and γ is not as critical as the sum $(\alpha + \gamma)$. The velocity ratio is high as $(\alpha + \gamma)$ approaches 180 deg.

The potential to generate extremely high velocities with a relatively low driving pressure can be illustrated by the following example. Suppose that $\alpha = 80$ deg and $\gamma = 90$ deg and that the driving pressure P_o is 1000 bar. Then from the relation $V_o \approx 14\sqrt{P_o}$, V_o is 440 m/s. But the velocity augmentation from Eq 3 is 11.4, so that V_{β} is 5000 m/s. To produce a jet velocity of this magnitude by conventional extrusion methods would require a driving

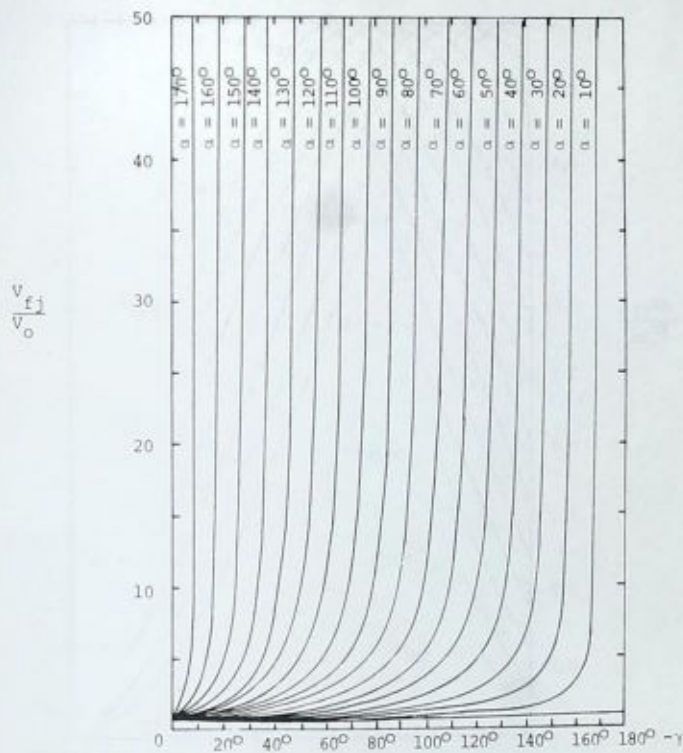


FIG. 4—Velocity augmentation ratio as a function of the impact angles α and γ .

pressure of 130 000 bar, 130 times that required if the augmentation is produced.

Figure 5 is a plot of the kinetic energy ratio EK_{β}/EK_{in} for various values of α and γ . From this figure it can be seen that the kinetic energy ratio is at a maximum value of 1 when α and γ are equal. Three types of flow can be identified based on the relationship between α and γ (Fig. 5). When $\gamma = \alpha$, all the energy is possessed by the fast secondary jet and the slow jet has none. In the region where $\gamma < \alpha$, the slow secondary jet moves to the left. In the region where $\gamma > \alpha$, the secondary slow jet moves to the right along with the fast secondary jet. Figure 6 is a plot of the concentration of energy ratio. This figure is very similar to Fig. 4 and the same comments apply. Based on the information that the kinetic energy ratio is maximum for $\alpha = \gamma$ (Fig. 5), the optimum condition for energy concentration can be plotted as a dashed line on Fig. 6.

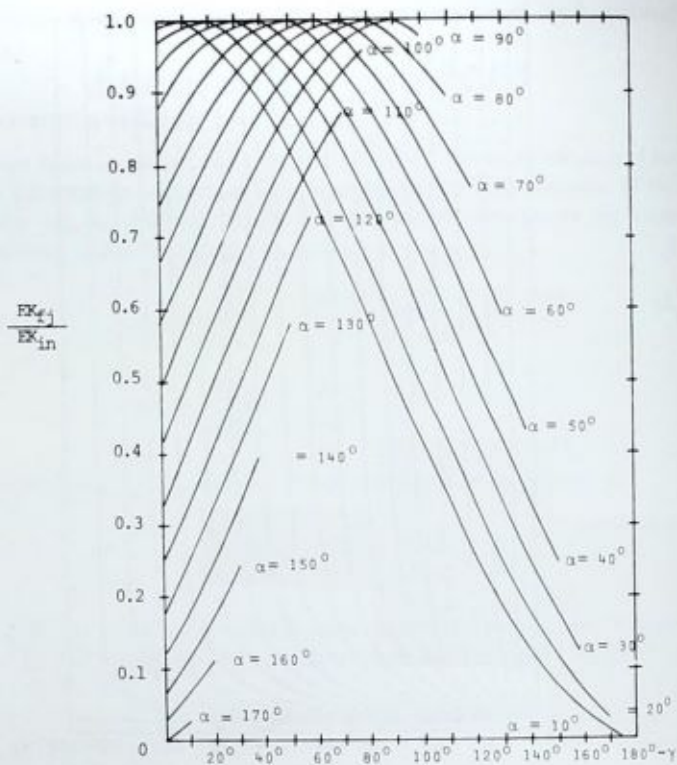


FIG. 5—Kinetic energy augmentation ratio as a function of the impact angles α and γ .

Experimental Applications

Under normal circumstances it is extremely difficult to obtain a flat leading edge to a waterjet or to maintain a uniform velocity across the jet profile. The surface or profile is generally curved (Fig. 1) or more severely distorted by jet movement relative to the surrounding medium.

At the point where the jet breaks into droplets, however, the contour of the leading surface will stabilize and the velocity will be sensibly constant within the droplet. This set of conditions allows the foregoing analysis to be extended to cover this case. Analysis of this phenomenon has been carried out in Cambridge [5] and therefore only a comparative relation will be made.

Figure 7 shows a central element sliced from a spherical droplet, of radius R and moving at speed V_0 toward the flat surface 00 at an angle α . Every phase of the collision can be considered using the previously derived equa-

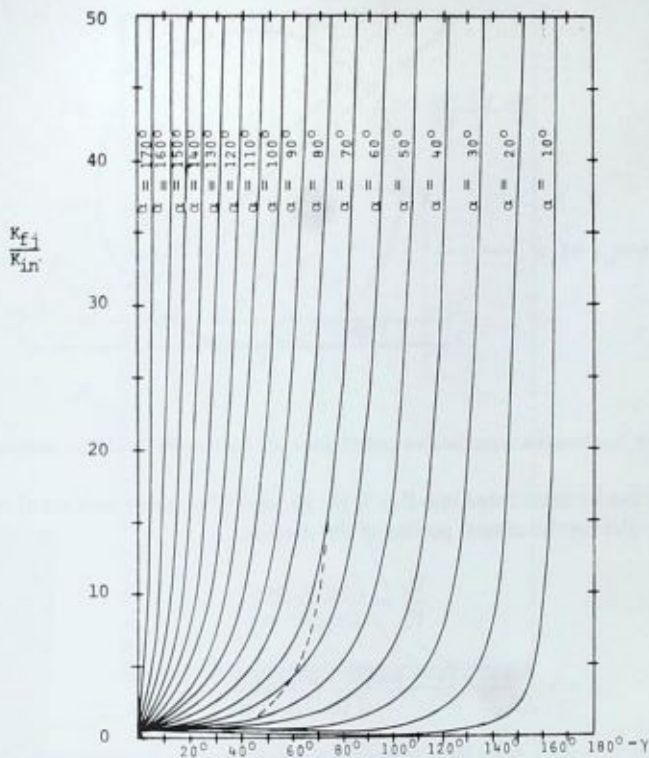


FIG. 6—Energy intensification ratio as a function of the impact angles α and γ .

tions with suitable transformations to adapt them to the present geometry. For example, when the face of the element from M' to M'' contacts the flat surface, the geometry is the same as that of Fig. 2. The droplet first contacts the plane 00 at M_1 and the analysis ends when the contact point moves along the arc to the point M_n . The value of β will vary from α to 180 deg in the interval

$$0 \leq t \leq \frac{R(1 + \sin\alpha)}{V_o \sin\alpha}$$

and

$$\gamma = 180 - \beta$$

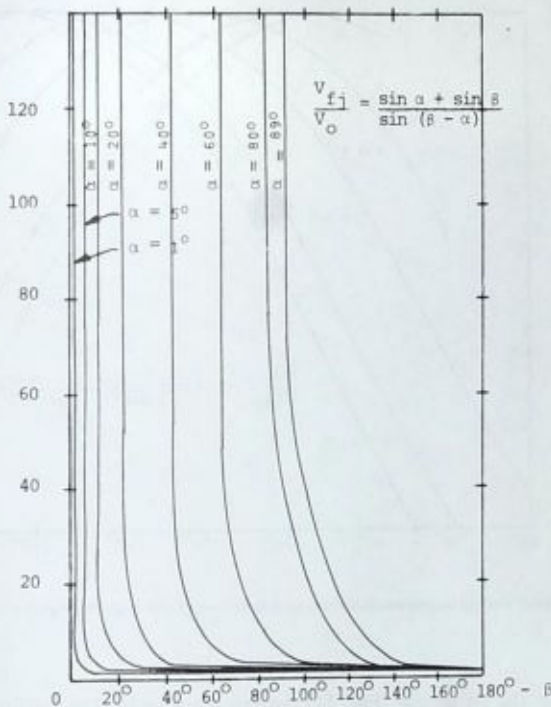


FIG. 8—Velocity augmentation ratio for a droplet impact as a function of the angles α and β .

The concentration of energy ratio shown plotted in Fig. 10 is similar to that for a flat-faced jet (Fig. 6). It is again found that, as α approaches β , so the energy ratio tends to infinity. Where values of α are small, the range of β over which the jet energy is highly concentrated is also small, but as α increases, so the width of the angle β over which a highly intensified jet is produced is also increased. It is interesting to note that the kinetic energy augmentation is at an optimum where $\alpha = \gamma$ and that the energy intensification is at an optimum where $\alpha = \beta$. Since $\gamma = 180 - \beta$, this suggests that the optimum energy augmentation with the most concentrated jet might occur when $\alpha = \beta = \gamma = 90$ deg. Under such circumstances the fast jet would be at greatest damage potential when the vertically impacting drop is at its maximum contact diameter. In this regard, investigators at Cambridge [5] have found that damage from impacting droplets is confined to the periphery of the droplet impact zone. The equivalence of the relationship between droplet flow and continuous jet flow is suggested by a corresponding result obtained at Rolla with a high-pressure continuous jet directed at an aluminum target located

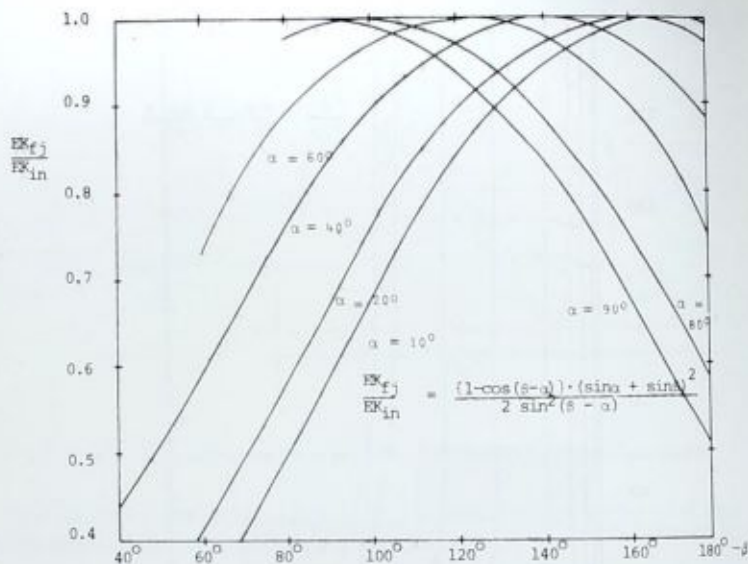
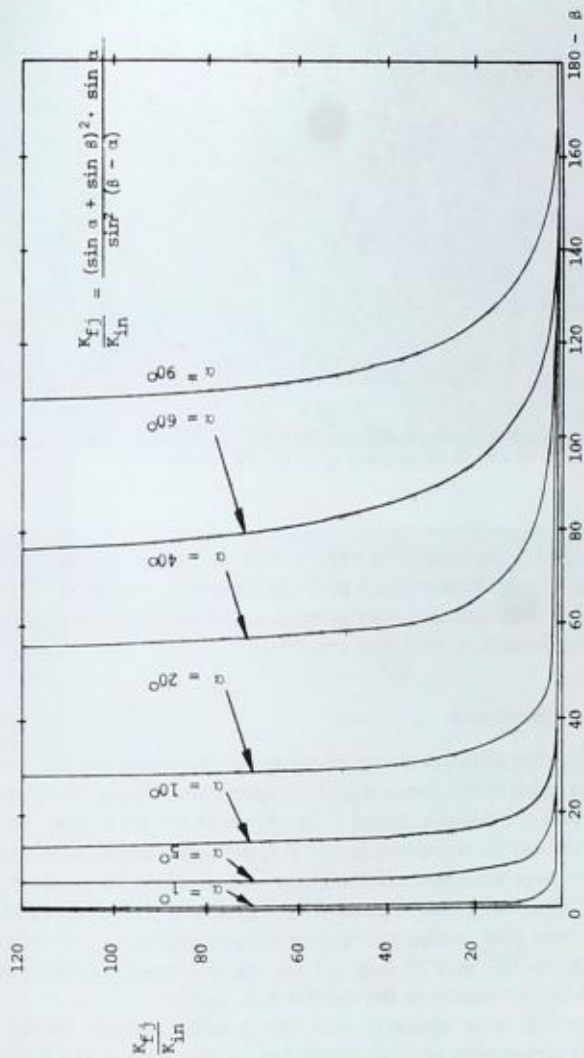


FIG. 9—Kinetic energy augmentation ratio as a function of the impact angles α and β for a droplet.

2.5 cm from the jet nozzle (Fig. 11), where damage is also confined to the region at and beyond the jet impact periphery.

Experiments have, however, concentrated on examining the zone of jet interaction farther down the jet stream where the flow has disrupted into droplets. Figure 12 shows a photograph of such a jet collision with an impact angle of $\alpha = 10$ deg at 4 bar obtained by the strobe flash technique [10]. All the droplet components of each jet do not impact other droplets since there is no control over their spatial distribution and velocity. When two droplets do collide, however, the shock wave generated by the fast jet is clearly visible. The results are similar to those of a collapsing cavitation bubble, which produces a Monroe jet with accompanying shock waves [6]. It is similar to the photographs obtained by Edney [7] of the explosive extrusion of the waterjet in a vacuum.

In practice the structure of a high-pressure waterjet, particularly at velocities of the order of 300 m/s, is extremely sensitive to interference from adjacent bodies. For this reason, while waterjet impact on solid bodies can be used to generate augmented velocities, the diffuse structure around two continuous jets will interfere with the jet structure prior to impact and negate much of the proposed augmentation. Conversely, once the jet has disintegrated into droplets, this is no longer the case, although the target

FIG. 10—Energy intensification ratios as a function of the impact angles α and β for a droplet impact.

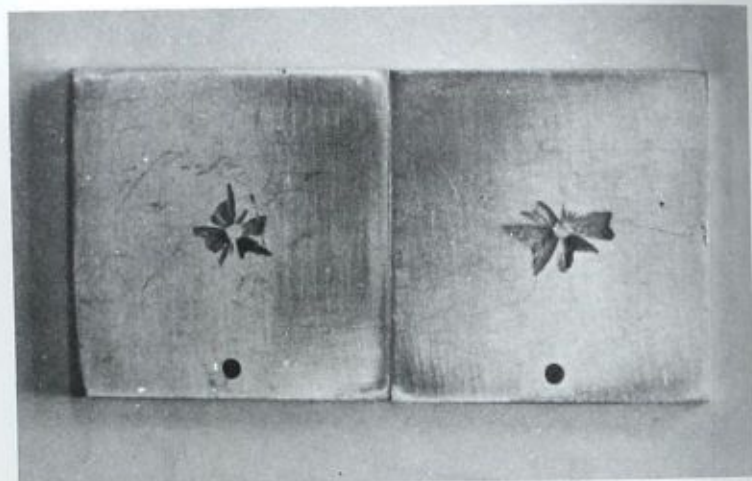


FIG. 11—Aluminum targets after continuous jet impact at 680 bar stagnation pressure; damage is confined to an area on the periphery of the jet and beyond.

location should be in the immediate vicinity of the impact point since the fast jets produced are extremely small and thus rapidly disrupted. Further research on the effectiveness of interfering jets, designed to interact beyond the jet collapse distance, is therefore required.

Rock Cutting Experiments

As a practical test of the potential effectiveness of converging jets, an experiment was carried out on Berea sandstone specimens, 15 cm diameter and 30 cm long, with test nozzles placed 1.25 cm above the specimen. The jet pressure was 680 bar for this study, in which approximately 20 different nozzle geometries were examined. Nozzles were constructed to produce two parallel jets of diameter 1 mm, separated by distances of 1.27, 1.78, and 3.0 mm. Nozzles were also constructed to produce converging jets at included angles 1, 2, 5, 10, 15, and 20 deg. All the nozzles were machined from brass and the inside surfaces of the nozzles were lapped.

The best results were obtained with the parallel nozzles having the 1.27- and 1.78-mm spacing and the convergent nozzles with 1- and 2-deg included angle. The results from the 5, 10, 15, and 20-deg angle were poor, no cumulative effect being observed. The sandstone specimens were split after an exposure time of 10 to 15 s when either the 1- or 2-deg nozzles were tested (Fig. 13).



FIG. 12—Views of water jets at a pressure of 4 bar converging at an angle of 10 deg at the point where the jet turns into droplets: (a) top view showing the angle of impact, (b) side view showing shock waves generated by the small augmented jet velocity.

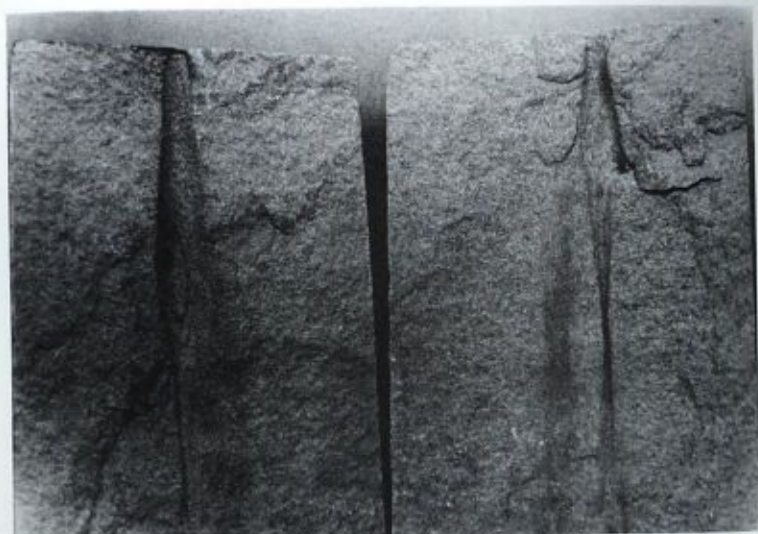


FIG. 13—Cavity cut into Berea sandstone by a converging jet showing the narrow cut made by secondary jet action.

Figure 14 shows one of the convergent nozzles located just above the sandstone. Using the parallel nozzles with 1.27- and 1.78-mm spacing gave results similar to those of the 1- and 2-deg convergent nozzles. One reason postulated for this is the Coanda effect by which two jets flowing close together tend to merge into one jet [9].

Subsequent to the conclusion of this experiment the authors were engaged in research on a hydraulic mining unit in a surface mine in northern Missouri [8]. The seam of coal was being mined by waterjets at a pressure of 680 bar when it was discovered that the coal was interlayered with pyrite lenses, with a compressive strength of the order of 2000 bar. Under normal conditions the jets would not cut this material, so a set of converging jet nozzles was inserted into the cutting head. The jets produced cut the pyrite satisfactorily, allowing the mining machine to advance at a rate of 1.7 m/min.

Conclusions

The use of external augmentation techniques to improve waterjet cutting ability has been demonstrated to be an effective way of improving the cutting of rock and is a means of generating higher pressures than those extant within the preexisting flow. Because of the problems which arise in bringing two flat-ended jets together exactly symmetrically, it is proposed herein that

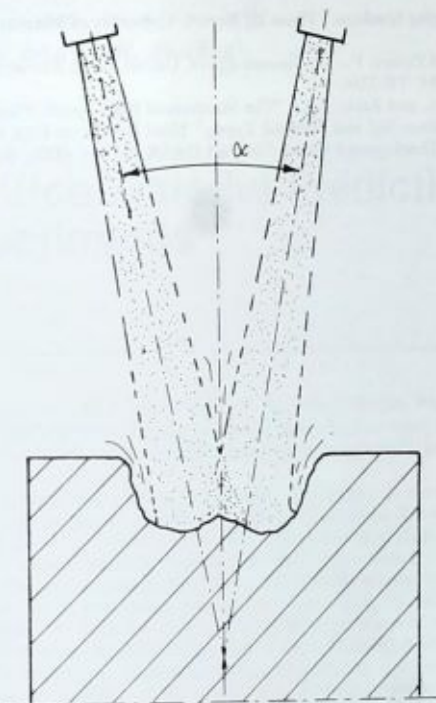


FIG. 14—Proposed geometry for augmented cutting using the enhanced velocity effects from colliding droplets.

a more effective technique would be to converge the jets at a point where they have just broken into droplets. Photographic evidence of such an event shows that large velocity augmentation is possible.

References

- [1] Birkhoff, G. et al, *Journal of Applied Physics*, Vol. 19, June 1948.
- [2] Walsh, T. M. et al, *Journal of Applied Physics*, Vol. 27, No. 3, March 1953.
- [3] Eichelberg, R. J. and Pugh, E. M., *Journal of Applied Physics*, Vol. 23, No. 5, May 1952.
- [4] "Externally Augmented Hypervelocity Jet Program," Bowles Engineering Corporation, Final Report R-10-31-69, Contract DOT-FR-9-0015, Silver Springs, Md. 1969.
- [5] Brunton, J. M., *Philosophical Transactions of the Royal Society*, Series A, Vol. 260, pp. 79-85, 28 July, 1966.
- [6] Summers, D. A. and Bushnell, D. J., *Proceedings*, Workshop on the Application of High Pressure Water Jet Cutting Technology, University of Missouri-Rolla, Rolla, Mo., 1975.
- [7] Edney, B. E., "Experimental Studies of Pulsed Water Jets," 3rd International Symposium on Jet Cutting Technology, Chicago, May 1976.
- [8] Summers, D. A., Barker, C. R., and Mazurkiewicz, M., "Development of a Longwall

Water Jet Mining Machine," Phase III Report, University of Missouri-Rolla, Rolla, Mo., 1977.

- [9] Metral, A. and Zerner, F., *The Coanda Effect*, United States Atomic Energy Commission Publication AEC-TR-3386.
- [10] Summers, D. A. and Zakin, J. L., "The Structure of High Speed, Fluid Jets and Their Use in Cutting Various Soil and Material Types," Final Report on USA Mobility Equipment Research and Development Center Contract DAAK 02-74-C-0006, April 30, 1975.

Dual-Orifice Waterjet Predictions and Experiments

REFERENCE: Selberg, B. P. and Barker, C. R., "Dual Orifice Waterjet Predictions and Experiments," *Erosion: Prevention and Useful Applications*, ASTM STP 664, W. F. Adler, Ed., American Society for Testing and Materials, 1979, pp. 493-511.

ABSTRACT: A simplified dual-orifice circular jet analysis is developed to predict maximum velocity and pressure profile capabilities of waterjets. The analysis is applied to nozzles having total exit diameters of 1.016 mm operating at stagnation pressures of 2.812 MN/m². These conditions result in flow rates of less than $2.27 \times 10^{-1} \text{ m}^3/\text{s}$ of water. Dual-orifice converging nozzles with 2- and 10-deg included convergence angles are analyzed as well as dual-orifice diverging nozzles with 8, 10, and 20-deg included divergence angles. The control-volume form of the conservation of mass and the conservation of momentum equations is applied to the converging dual-jet case. Velocity profiles prior to jet mixing, after Schlichting and Tollmien, are used as profile input to the conservation equations. Profile shapes after Schlichting are used downstream of the jet mixing process. Linear jet diameter growth laws are applied to predict jet diameters before and after the mixing process. The merged jet profiles are calculated downstream of the nozzle at representative stations and compared with a single-orifice jet profile of the same energy input. Diverging dual-orifice jet profiles are generated using the same profile and diameter growth equations as for the converging dual-orifice nozzle jet. Velocity and pressure profiles, generated at representative stations downstream of the nozzle exit, are compared with single-orifice nozzle profiles of the same total energy input. Experimental comparisons are made with 2- and 10-deg included-convergence-angle converging nozzles and with 8, 10, and 20-deg included angle diverging nozzles at 2.812 MN/m² stagnation pressure. All nozzle shapes consist of a 13-deg converging cone followed by a straight section of length 2.5 exit diameters. A pressure transducer, fixed to the traveling carriage of a lathe and oriented so that the nozzle axis is in line with the transducer axis, is used for profiling studies. A hardened steel shield with a 5.00×10^{-1} mm central hole protects the transducer for the pressure profile studies. These pressure profile measurements are made at the same representative stations as the analytical results. Discussion of the agreement between analytical and experimental results is made with emphasis on limitations of the analytical model, the experimental tests, and on suggested improvements in nozzle design which will bring the analytical predictions and experimental results closer together.

KEY WORDS: waterjets, dual-orifice jets, converging jets, diverging jets, nozzle surface roughness, jet coherence, jet cutting, erosion

¹ Associate professor of aerospace engineering; associate professor of mechanical engineering and research associate, respectively, University of Missouri-Rolla, Rolla, Mo. 65401.

Many researchers have investigated both theoretically and experimentally single-orifice waterjets [1-8].² From this work the most widely accepted nozzle has a conic convergent section with a 13-deg angle followed by a straight section of length 2.5 exit diameters. Generally, these single-orifice nozzles are capable of producing waterjets that remain coherent for a distance of 100 to 250 nozzle diameters [9]. Some improvement in these jet coherence lengths can be obtained by adding long-chain polymers to the water [10] or by changing nozzle geometry [3, 11].

Whereas single-orifice nozzle design is well understood, there has been comparatively little work conducted on dual- or multiple-orifice design. Some work has been carried out by Nikonov [12] and Summers [13] et al. Nikonov found that a 15-deg-included-angle dual-orifice nozzle gave the most effective jet action whereas Summers et al obtained the best results with a 20-deg-included-angle dual-orifice diverging nozzle. It is the purpose of this paper to further develop the multiple-orifice nozzle base by investigating dual-orifice nozzles that are being fed by the same supply pipe.

Theoretical Analysis

A simplified turbulent-jet theory, due first to Tollmien [14], was applied to axisymmetric circular jets. This theory is for an airjet into air or a waterjet into water and does not take into account the two-phase flow which will occur at the waterjet-air boundary. However, the application of this simplified turbulent-jet theory is consistent with the intent of trying to predict maximum possible pressure and velocity profiles prior to significant jet-air mixing or jet breakup. The theory assumes the jet width is proportional to axial length of the jet, x , and that the centerline velocity is proportional to $1/x$. The linear jet width growth is in agreement with most experimental data of turbulent axisymmetric jets of water into air. Recent measurements of Yanaida [15] show a $x^{1/2}$ growth of the jet width. In addition, the kinematic momentum is taken a constant along the jet axis. These assumptions imply a constant virtual kinematic viscosity, ϵ_0 , as well as identical differential equations as for laminar jet flow. Schlichting's solution of these equations is

$$\begin{aligned}
 u &= \frac{3}{8\pi} \frac{K}{\epsilon_0 x} \frac{1}{(1 + 1/4\eta^2)^2} \\
 v &= \frac{1}{4} \sqrt{\frac{3}{\pi}} \sqrt{\frac{K}{x}} \frac{\eta - 1/4\eta^2}{(1 + 1/4\eta^2)^2} \\
 \eta &= \frac{1}{4} \sqrt{\frac{3}{\pi}} \sqrt{\frac{K}{\epsilon_0 x}}
 \end{aligned}
 \tag{1}$$

²The italic numbers in brackets refer to the list of references appended to this paper.

where

- u = axial velocity component,
- v = velocity component perpendicular to jet axis,
- x = distance in axial direction of jet,
- r = distance in direction perpendicular to axis,
- K = jet kinematic momentum divided by fluid density, and
- ϵ_0 = virtual kinematic viscosity.

These solutions were used to generate velocity profiles at various jet locations downstream of the nozzle exit. Input conditions to these profiles were obtained by first using Bernoulli's equation for incompressible flow to predict the maximum velocity point u_{max} at the center of the jet and exit of the nozzle. Along the jet axis, the centerline velocity u_{cl} was determined utilizing a form suggested by Hinze [16]

$$\frac{u_{cl}}{u_{max}} = A \left(\frac{d}{x+B} \right) \quad (2)$$

where d is the jet diameter at the nozzle and A and B are constants. The constants A and B were solved for in Eq 2 from experimentally determined centerline velocity measurements at the $x/d = 25$ and $x/d = 50$ stations. For each axial location, u_{cl} is calculated from the foregoing and then used with the u from Eq 1 to solve for the correct value of virtual kinematic viscosity, ϵ_0 , at each axial location. With the proper ϵ_0 's, profiles of u can then be generated. System design constraints necessitated having a pipe 6.35 mm inside diameter and 762 mm long upstream of the nozzle. With this supply pipe-nozzle configuration the flow into the nozzle would be fully developed pipe flow. Although the acceleration in the nozzle would thin the boundary layer and flatten the velocity profile at the nozzle exit, the exit flow conditions would more nearly be approximated by a modified pipe flow. Therefore a one-seventh power velocity profile was taken at the velocity exit. This compares well with turbulent smooth-pipe data for the Reynolds number in question [2]. The mean velocity can then be obtained from the one-seventh power law, $\bar{u} = 0.816 u_{max}$. The volume flow rate, Q , then becomes

$$Q = \pi R^2 \bar{u} = 0.816 \pi R^2 u_{max} \quad (3)$$

The kinematic momentum can be calculated at the nozzle exit and is

$$K = 2\pi \int_0^R u^2 r dr = 2\pi u_{max}^2 \int_0^R \left(\frac{r}{R} \right)^{2.7} r dr \quad (4)$$

The kinematic momentum is then available as input into the foregoing velocity profile equations. Utilizing these equations, velocity data have been generated for the dual diverging jets and then transformed to nozzle axis, x , and to the coordinate normal to the nozzle axis, r . With the control-volume form of the momentum equation, the force on transducer orifice can be calculated. This force is then divided by the transducer orifice area to obtain the pressure.

These same velocity profiles are used as input for the converging dual-jet analysis. The converging dual-jet analysis utilizes the control form of the momentum and mass equations. The momentum equation for a non-moving control volume is

$$\Sigma \mathbf{F} = \int_{cs} \int \rho \mathbf{V}(\mathbf{V} \cdot \boldsymbol{\eta}) dA + \frac{\partial}{\partial t} \int_{cv} \int \int \rho \mathbf{V} dR \quad (5)$$

where

$\Sigma \mathbf{F}$ = summation of external forces on control volume,

ρ = fluid density,

\mathbf{V} = fluid velocity,

$\boldsymbol{\eta}$ = outward normal unit vector of dA ,

dA = elemental surface element of control surface, cs ,

t = time, and

dR = elemental volume element of control volume, cv .

For steady flow the last term on the right-hand side is zero and for a free jet the pressure forces cancel, leaving

$$\int_{cs} \int \rho \mathbf{V}(\mathbf{V} \cdot \boldsymbol{\eta}) dA = 0 \quad (6)$$

This term, which is the momentum flux through the control surface, is nonzero only where the jet crosses the control surface. Figure 1 shows a typical merging jet with the control surface. The merging jets, 1 and 2, use the velocity profile due to Schlichting, given previously. The momentum equation can be rewritten for axisymmetric jets as

$$\int_0^{\infty} \rho V_3 V_3 r dr = \int_0^{\infty} \rho V_1 V_1 r dr + \int_0^{\infty} \rho V_2 V_2 r dr \quad (7)$$

Since the form of velocity is known, and the density remains constant for the pressure range considered, Eq 7 can be solved for V_3 .

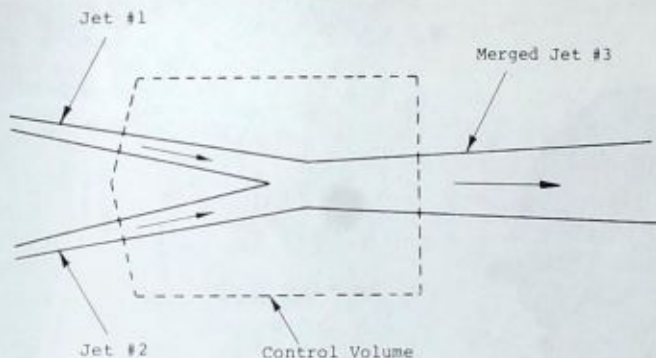


FIG. 1—Merging jets with control volume.

Experimental Apparatus and Procedure

The pressure profiling experiments were conducted on a modified lathe bed. The nozzle supply pipe was mounted onto the lathe chuck with the stagnation chamber located directly upstream of the lathe. Stagnation supply pressures were measured in this chamber. The stagnation chamber was connected to the 5.58×10^4 J/s pump by a flexible high-pressure hose. The strain gage pressure transducer was mounted to a vertical milling attachment which in turn was mounted to the carriage of the lathe for axial and transverse movement. Transverse location was monitored with a linear potentiometer in conjunction with one channel of a chart recorder, with pressure recorded on the second channel of the recorder, yielding a plot of pressure versus transverse distance for each nozzle axial location of the transducer. The experimental setup is shown in Fig. 2.

The pressure transducer itself was mounted inside a steel plug whose front surface was flat and about 38.1 mm in diameter. The surface of the plug was hardened with a small centered hole, 5.00×10^{-1} mm in diameter, leading to the transducer. The transducer system was capable of measuring pressures up to 2.81 MN/m^2 . All nozzle tests, in which data close to the nozzle were to be taken, were conducted at a stagnation pressure of 2.81 MN/m^2 .

Test procedures involved aligning the pressure transducer in the vertical direction to maximize the signal from the water jet at a stagnation pressure of $4.22 \times 10^3 \text{ N/m}^2$, to ensure that the pressure orifice was at the maximum velocity plane in the vertical direction. The test runs were then conducted at the desired operating stagnation pressure. For each jet and axial location a minimum of two jet traverses were made to ensure data repeatability.

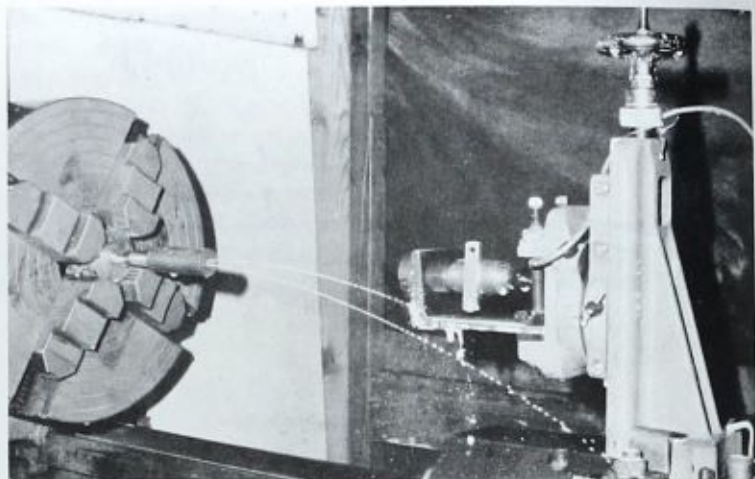


FIG. 2—Pressure profiling apparatus.

Results and Discussion

All the dual-orifice nozzles were the same shape, a 13-deg converging cone followed by a 2.5-exit-diameter straight section. Each orifice had an exit diameter of 1.016 mm. Four of the nozzles—the 10 and 20-deg diverging dual-orifice nozzles and the 10 and 2-deg converging nozzles—were machined out of brass and then nickel plated to prevent surface erosion effects. All the brass nozzles were machined by one technician using the same technique and were polished before plating. The 8-deg dual-orifice diverging jet nozzle is an electroformed nickel nozzle in which the nozzle is electroformed around a machined mandrel. The general contour of all the nozzles tested is shown in Fig. 3. Pressure-profiling results are presented in Fig. 4 for the 20-deg diverging nickel-plated dual-orifice nozzle that was machined of brass. The experimental profiles are the solid lines while the theory is shown by the solid circles. There is good agreement between theory and experiment at $x/d = 25$ and $x/d = 50$; however, at axial locations of $x/d = 125$ and larger, there is a rapid deterioration of the experimental data. Both jets are deteriorating at about the same rate, which is caused by an accelerated breakup of the jet core. This premature core breakup is due to some upstream perturbation on the jet which is setting up jet instabilities.

Figure 5 shows theoretical and experimental pressure-profiling results for the 10-deg nickel-plated brass dual-orifice jet. The experimental results, solid line, agree with theory only for the $x/d = 25$ station. The jets are

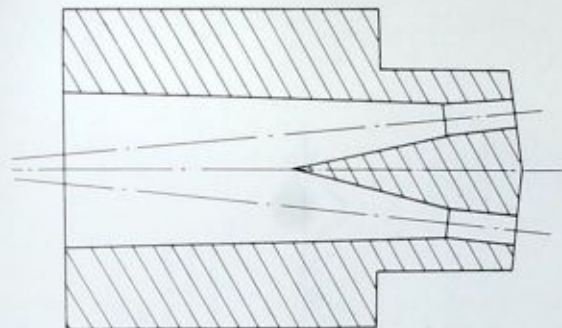
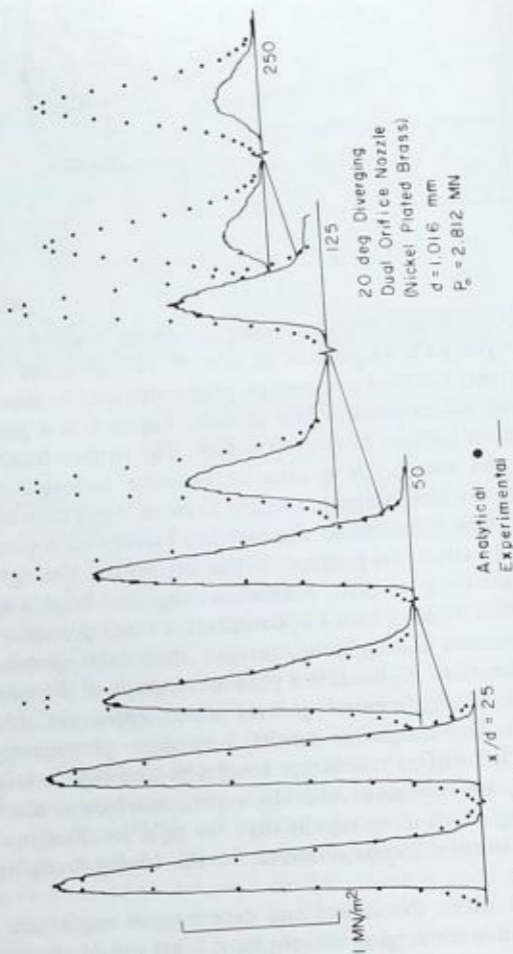


FIG. 3—Generalized nozzle design.

decaying rapidly, with the left jet 11 percent of its initial value and 25 percent of the right jet's magnitude at $x/d = 125$. In order to explain this poor agreement, electron microscope photomicrographs were taken of the inside of both nickel-plated brass orifices. Figure 6 is a photomicrograph of the interior surface of the left orifice. The surface finish appears to be uniform and rough. A qualitative estimate indicates roughness heights of 10^{-2} mm, which is approximately 33 times larger than acceptable typical nozzle finishes for nominal-size nozzles. Figure 7 is a photomicrograph of the right orifice. In contrast to the left orifice, the right orifice interior finish is relatively smooth. Maximum roughness heights appear to be on the order of 5×10^{-3} mm but constitute a small percentage of the total surface. However, the right orifice does show faint grooves in the circumferential direction. Figure 8 is a photomicrograph of the entire right orifice. The same circumferential grooves which appear in this figure appear in Fig. 7. The roughness results from these photomicrographs, namely, that the left orifice has larger roughness and that it exists over the entire surface, are consistent with the experimental data, which show the left jet decaying much more rapidly than the right jet. Roughness thus explains the experimental trends observed for the 10-deg diverging dual-orifice brass nozzle.

Converging dual-orifice theoretical and experimental results are shown in Fig. 9 for the 2-deg converging nickel-plated brass nozzle. Again agreement is excellent at $x/d = 50$. At $x/d = 125$ the right jet shows good agreement while the left jet is already breaking up. At $x/d = 175$ the two jets have merged and the agreement is good considering one of the converging jets was breaking up. Likewise at $x/d = 250$ the agreement is good. By $x/d = 375$, however, the merged jet is breaking up rapidly. The narrower experimental results can be attributed to the insufficient momentum input from the left jet to the final merged jet. Although the

EROSION: PREVENTION AND USEFUL APPLICATIONS



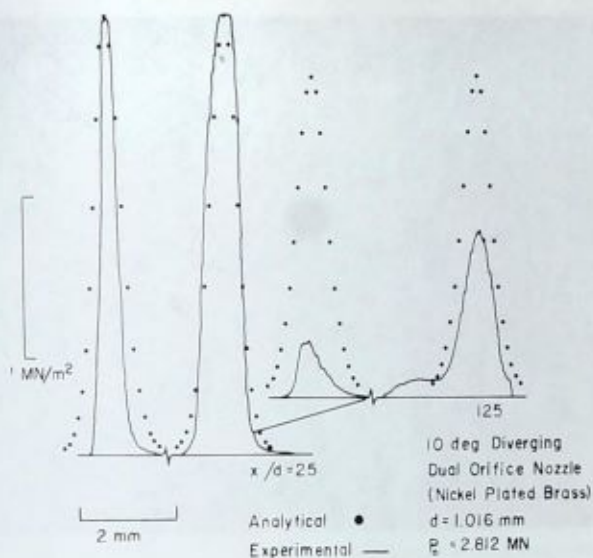


FIG. 5—Pressure profiles for 10-deg diverging dual-orifice nickel-plated brass nozzle.

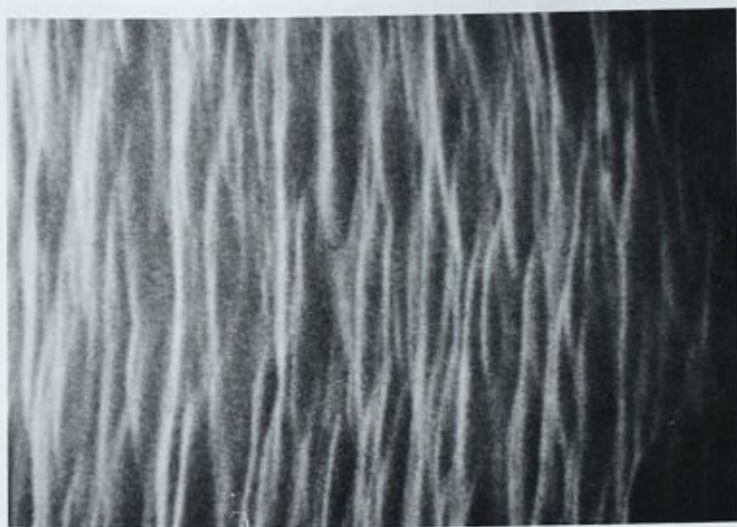


FIG. 6—Photomicrograph of 10-deg dual-orifice nozzle—left orifice ($\times 675$).



FIG. 7—Photomicrograph of 10-deg dual-orifice nozzle—right orifice ($\times 675$).

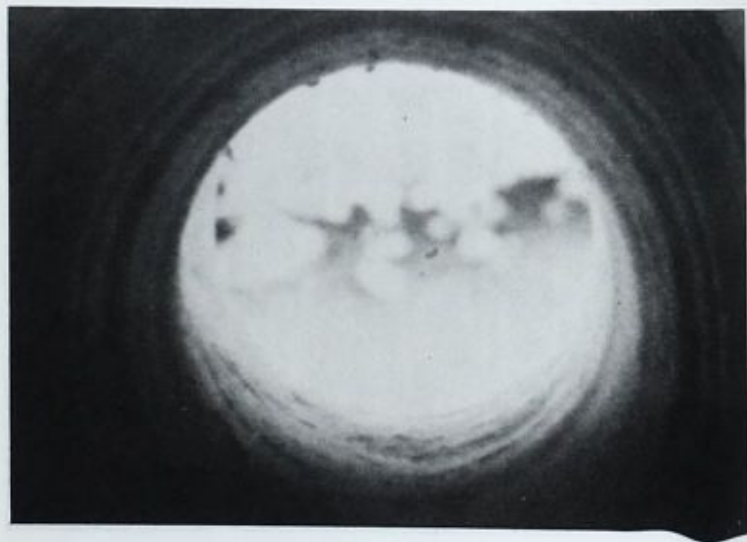


FIG. 8—Photomicrograph of 10-deg dual-orifice nozzle—right orifice ($\times 56$).

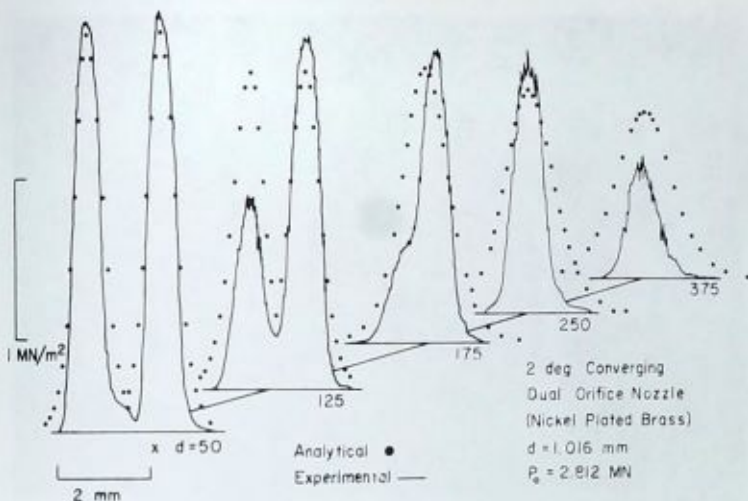


FIG. 9—Pressure profiles for 2-deg converging dual-orifice nickel-plated brass nozzle.

merged jet is broader than each of the individual jets, it does not appear to be as broad as a single jet of the same initial mass flow would be. A more significant observation is that the peak velocity of the merged experimental jet exceeds the analytical prediction at both $x/d = 125$ and $x/d = 250$, indicating a slower center velocity decay rate for the merged jet. This may partially explain why merged dual-orifice waterjets are more effective in actual material cutting tests than diverging dual-orifice jets. Figure 10 is a photomicrograph of the right orifice interior surface. The majority of the surface is relatively smooth with a few large protrusions on the order of 10^{-2} mm and a few minor grooves. In contrast, Fig. 11 shows the left orifice surface, which is rough all over, having roughness heights on the order of 10^{-2} mm with a large circumferential groove on the order of 4×10^{-2} mm high by at least an equal width. This circumferential groove along with others are shown clearly in Fig. 12, a photomicrograph of the entire interior surface of the left orifice exit. Each of these grooves, which lie transverse to the flow direction, will perturb the boundary-layer flow and tend to cause temporary boundary-layer separation or flow oscillations, which will result in early jet breakup. Again there is consistency between the rough surface of the left jet and its early decay, and the smoother surface of the right jet and its good agreement with theory.

Results of the 10-deg converging jet are shown in Fig. 13. At $x/d = 25$ the jets are already merged. While good agreement exists initially, there is a rapid decay of the experimental jet. This rapid decay, which may in



FIG. 10—*Photomicrograph of the 2-deg dual-orifice nozzle—right nozzle ($\times 675$).*

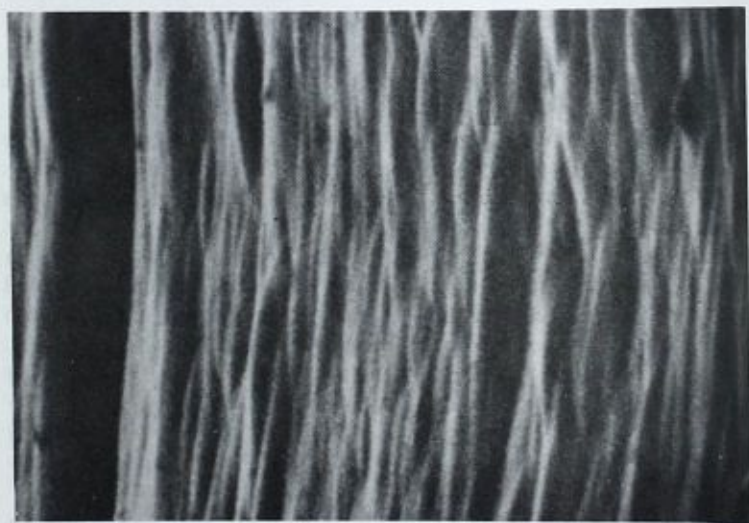


FIG. 11—*Photomicrograph of the 2-deg dual-orifice nozzle—left orifice ($\times 675$).*

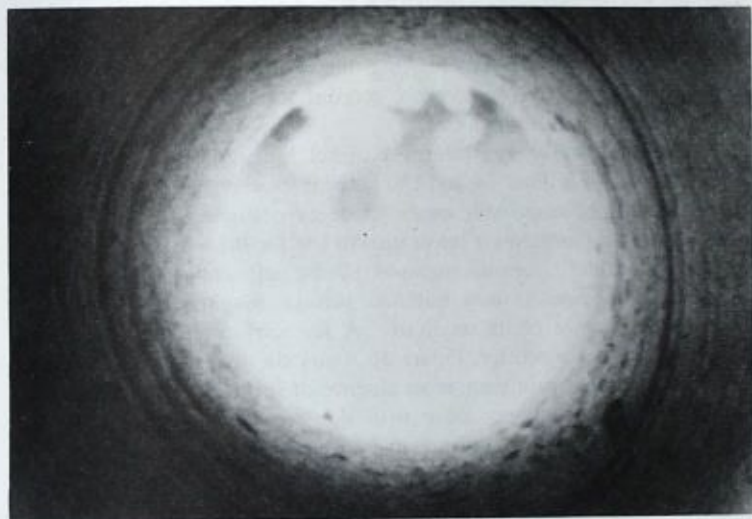


FIG. 12—Photomicrograph of the 2-deg dual orifice nozzle—left orifice ($\times 56$).

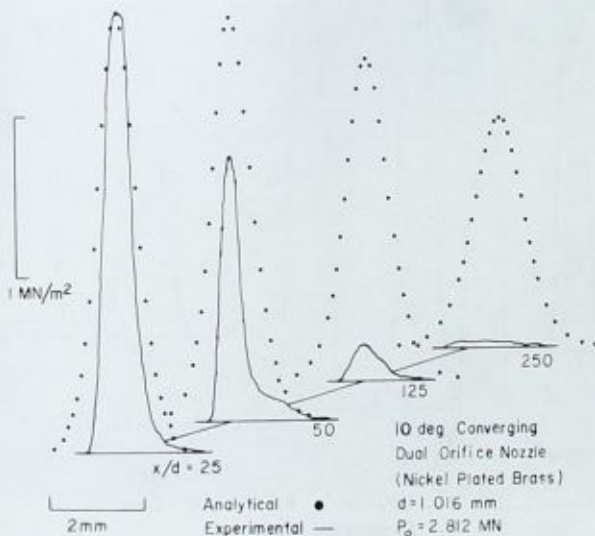


FIG. 13—Pressure profiles for 10-deg converging dual-orifice nickel-plated brass nozzle.

part be due to the surface finish of the nickel-plated brass nozzle, is probably also caused by the larger amount of momentum exchange that the two colliding jets are experiencing due to the larger converging angle between them. The theory does not account for this mixing in the sense of the resulting momentum losses.

The results for the electroformed nickel 8-deg diverging dual-orifice nozzle are shown in Figs. 14 and 15. There is excellent agreement between theory and experiment, with minor jet decay occurring in the left jet at $x/d = 375$, substantiating a linear growth law for the wake width. Figures 16 and 17 exhibit photomicrographs of the left and right jet interior surfaces. Both figures show minimal surface roughness, which is not estimatable because of its small size. A few surface imperfections exist but these are not repetitive. Figure 18 shows the left side with a view of the entire orifice. Again there is an absence of surface imperfections. This lack of surface roughness along with the excellent agreement between theory and experiment confirms the postulation that excessive surface roughness in the nickel-plated brass nozzles was causing the boundary layer to locally separate or instabilities to be set up within the jet which led to its early decay, or both.

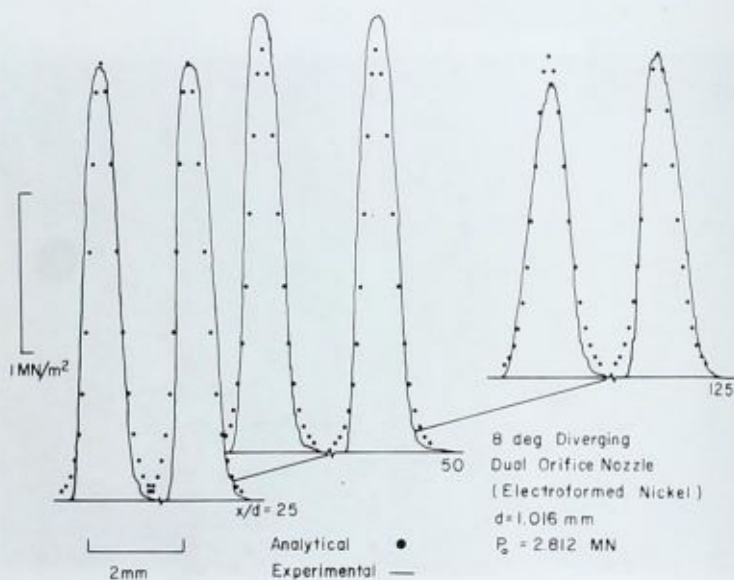


FIG. 14—Pressure profiles for 8-deg diverging dual-orifice electroformed nozzle.

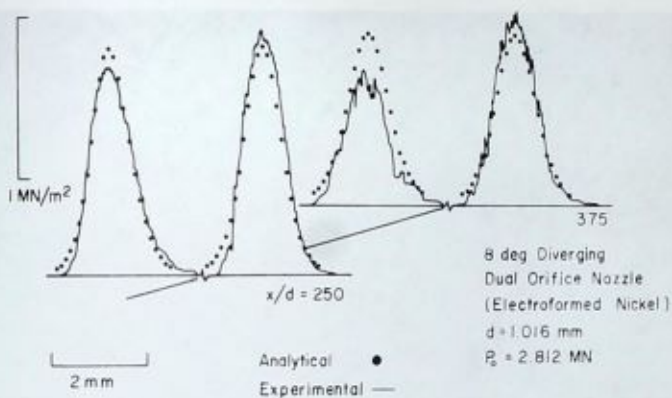


FIG. 15—Pressure profiles for 8-deg diverging dual-orifice electroformed nozzle.



FIG. 16—Photomicrograph of 8-deg electroformed nickel dual-orifice nozzle—left side ($\times 675$).

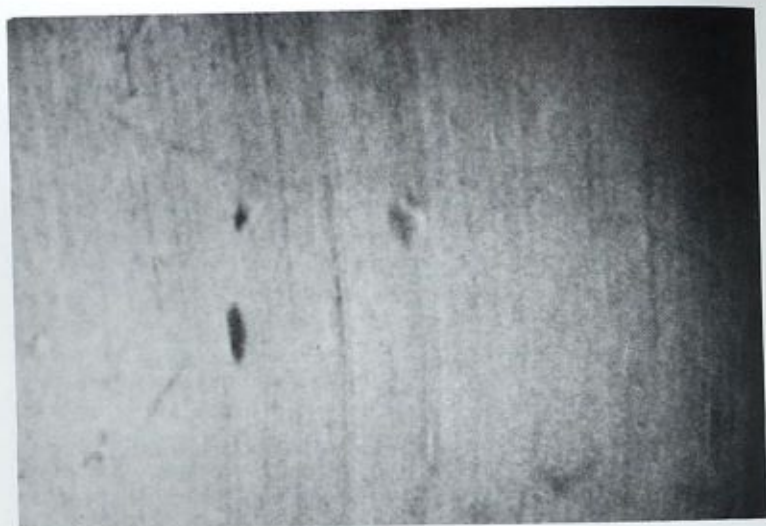


FIG. 17—*Photomicrograph of 8-deg electroformed nickel dual-orifice nozzle—right side ($\times 675$).*

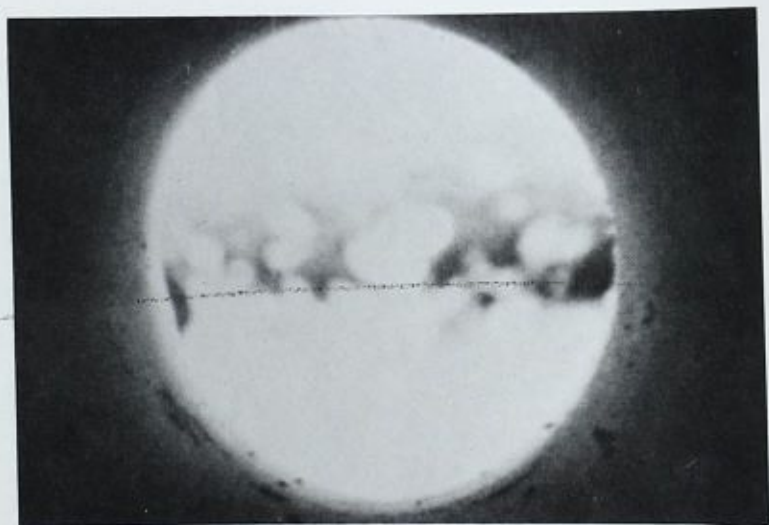


FIG. 18—*Photomicrograph of the 8-deg electroformed nickel dual-orifice diverging nozzle—left side ($\times 67$).*

Conclusions

The following conclusions are made concerning dual-orifice high-pressure waterjet predictions and experiments.

1. The simplified theoretical analysis is capable of predicting waterjet pressure profiles for dual-orifice diverging nozzles prior to jet breakup.
2. The control-volume analysis shows good promise of being a valid prediction technique for converging waterjets with small convergence angles prior to jet breakup.
3. The experimental results reinforce the importance of manufacturing nozzles to close tolerances such that interior nozzle surface finishes are free of blemishes.
4. Small-angle converging dual-orifice data indicate slower centerline maximum velocity decay rates than diverging jets, which explains the apparent superiority of converging jets to diverging jets in material cutting tests.
5. The electroformed 8-deg dual-orifice nozzle tests substantiate a linear growth rate for the wake width.

References

- [1] Leach, S. J. and Walker, G. I., *Proceedings of the Royal Society*, London, Vol. 260A, 1966, pp. 295-308.
- [2] Schlichting, H., *Boundary Layer Theory*, McGraw-Hill, New York, 1968.
- [3] Lohn, P. D. and Walker, D. A., "Improved Mineral Excavation Nozzle Design Study," Bureau of Mines Report 33-77, 1976.
- [4] Hokao, J., *Journal of the Japan Mining Association*, Vol. 81, No. 930, Oct. 1965, pp. 907-912.
- [5] Fowkes, R. S. and Wallace, J. J., "Hydraulic Coal Mining Research-Assessment of Parameters Affecting the Cutting Rate of Bituminous Coal," Bureau of Mines Report 7090, 1968.
- [6] Summers, D. A., unpublished data, 1974.
- [7] Voitsekhevsky, V. B. et al., "On the Destruction of Rocks and Metals by High Pressure Jets of Water," *Proceedings, 1st International Symposium on Jet Cutting Technology*, Coventry, U. K., Paper G8, 1972.
- [8] Daniel, I. M., Rowlands, R. E., and Labus, T. J., "Photoelastic Study of Water Jet Impact," *Proceedings, 2nd International Symposium on Jet Cutting Technology*, Cambridge, U. K., Paper A1, 1974.
- [9] Cooley, W. C., "Correlation of Data on Liquid Jet Cutting of Rock and Other Materials," for National Science Foundation, Research Applied to National Needs, Jan. 1975.
- [10] Franz, N. C., "The Influence of Standoff Distance on Cutting with High Velocity Fluid Jets," *Proceedings, 2nd International Symposium on Jet Cutting Technology*, Cambridge, U.K., Paper B3, 1974.
- [11] Flow Research, Inc., sales literature, 1975.
- [12] Nikonov, G. P., "Research into the Cutting of Coal by Small Diameter High Pressure Water Jets," *Proceedings, 12th Symposium on Rock Mechanics*, Rolla, Mo., 1970.
- [13] Summers, D. A. et al., "Excavation of Coal Using a High Pressure Water Jet System," Final Report, USDI H023064, U.S. Department of the Interior, 1974.
- [14] Tollmien, W., "Berechnung Turbulenter Ausbreitungsvorgänge," NACA TM 1085, National Advisory Committee for Aeronautics, 1945.

- [15] Yanaida, K., "Flow Characteristics of Water Jets, *Proceedings, 2nd International Symposium on Jet Cutting Technology, Cambridge, U.K., Paper A2, 1974.*
- [16] Hinze, J. O., *Turbulence*, McGraw-Hill, New York, 1959.

DISCUSSION

*P. D. Lohn*¹ (written discussion)—How were A and B chosen? Would normalizing to the merged jet diameter (in the convergent case) be more meaningful? Could the imperfections in the finish trigger a bistable flow favoring the smoother nozzle? (One of the diverging cases appeared not to be due to a bistable effect but to accelerated breakup.)

B. P. Selberg and C. R. Barker (authors' closure)—The centerline velocity was determined experimentally at the $x/D = 25$ and the $x/D = 50$ stations and these values were then used to calculate A and B from the centerline velocity decay equation.

While normalizing to the merged jet might be useful in discussing jet properties, it would be difficult to apply since both different convergent angles and different initial converged jet diameters would provide different baseline diameters, which in turn would make the normalizing of jet data difficult to understand and compare. A more interesting approach might be normalizing to a jet equivalent diameter based on the total jet areas of the two converging jets at the nozzle exit. This would allow all converging nozzles to be compared to the equivalent-area single-orifice nozzle.

One would expect that if surface finish imperfections were triggering a bistable flow condition, the smooth nozzles (orifice) would have a coherent jet for a greater distance than without the bistable flow. Subsequent tests with single-orifice nozzles having the same surface finish indicated a longer coherent jet than for the good orifice side of the diverging nozzle; hence the bistable hypothesis is not substantiated.

*A. F. Conn*² (written discussion)—Typical jet breakup lengths seen in the literature are in the range of 100 to 200 nozzle-orifice diameters, yet you report jets which have broken up by 375 diameters. Do you attribute these large stable distances to the very smooth surfaces inside the nozzle?

B. P. Selberg and C. R. Barker (authors' closure)—Our nozzles, from which we achieved the 375 x/D coherent jet lengths, were the standard Leach-Walker design which have been used and reported on by many

¹TRW Systems & Energy, Inc., Redondo Beach, Calif.

²Hydronautics, Inc., Pindell School Road, Laurel, Md. 20810.

investigators. The only difference is the new nozzle manufacturing process that yields extremely uniform and smooth nozzle surface finishes which are not attainable by standard manufacturing techniques for small nozzles. These coherent jet lengths may have been further increased if more attention had been given to better flow conditioning upstream of our nozzle.

A Study of Erosion by High-Pressure Cavitating and Noncavitating Waterjets

REFERENCE: Vijay, M. M. and Brierley, W. H., "A Study of Erosion by High-Pressure Cavitating and Noncavitating Waterjets," *Erosion: Prevention and Useful Applications, ASTM STP 664*, W. F. Adler, Ed., American Society for Testing and Materials, 1979, pp. 512-529.

ABSTRACT: A study was made of erosion by high-pressure noncavitating and cavitating waterjets issuing from five different arrangements of nozzles, consisting of (A) jet in air, (B) submerged jet, (C) jet surrounded by another of lower velocity, (D) jet from long nozzles, and (E) jet from a nozzle containing a cylindrical body insert. The purpose was to evaluate the two methods of erosion for jet cutting applications.

Simple visual examination of the craters on specimens of copper showed distinct type (size, shape, depth, etc.) of erosion. However, microscopic examination did not reveal clearly any characteristics peculiar to cavitating or noncavitating jets.

Quantitative experimental results were obtained by measuring the mass loss of lead specimens as a function of time of exposure for the conditions where either the nozzle pressure or the standoff distance was held constant. By comparing the different arrangements on the basis of material loss, it is concluded that Arrangement B performed best for all periods of exposure and standoff distances followed by Arrangement C for short periods of exposure, smaller standoff distance, and for certain flow conditions.

KEY WORDS: erosion, high pressure, cavitating, noncavitating, water jet, jet cutting applications, nozzle, crater, mass loss, lead and copper specimens, time of exposure, nozzle pressure, nozzle diameter, standoff distance, submerged jet, arrangement, evaluation, comparison, material removal, penetration

The application of waterjets for mining and other problems is well known and is quite well documented [1].² However, because of the requirement of high pressures, waterjets alone are not adequate to fracture hard rocks which are encountered in tunneling and other operations. To overcome this

¹Research officer and technical officer, respectively, Gas Dynamics Laboratory, Mechanical Engineering Division, National Research Council of Canada, Ottawa, Ontario, Canada.

²The italic numbers in brackets refer to the list of references appended to this paper.

problem of high pressures, methods recently have been proposed whereby the erosive power of a waterjet could be augmented by the generation of cavitation bubbles within the jet [2]. It was argued that since these bubbles create intense transient pressures at the points of collapse (thus fracturing the material), the actual pressure of waterjets could be reduced. While reports claiming their success in certain applications have appeared [3,4], some doubts regarding their usefulness have also been reported [5]. This investigation was undertaken to study the erosion caused by noncavitating and cavitating jets in detail and to compare their performance with regard to jet cutting applications.

Qualitative and quantitative results are given to support the views expressed in the paper.

Experimental Facility and Procedure

The high-pressure experimental facility in our laboratory for jet cutting studies has been described in detail in an earlier publication [6]. The pump used for the tests was the Union Quintuplex pump rated at 69 MPa (10 000 psia) and 50 litre/min (13 gal/min). All the experiments were conducted in a Plexiglas tank and the arrangements used to identify the tests are shown in Fig. 1. The nozzles employed (Fig. 1) were designed to meet the present requirements. The general features of each arrangement are as follows:

(A) The tests done in this arrangement (with Type A nozzle) constitute the conventional noncavitating tests.

(B) Submerged jet, Type A nozzle: the cavitating characteristics of a submerged jet have been clearly shown by Rouse [7] and Lichtarowicz [3].

(C) This arrangement was developed to simulate either (A) or (B) depending upon the velocity (V_s) of the outer stream. As in Type (B), due to the high shear stress between the two jets, cavitation bubbles are expected to be generated at the interface of the two jets.

(D) The long or straight nozzles (Type B) in this case have been investigated by Pearce and Lichtarowicz [8] and their cavitating characteristics are shown to depend on the ratio L/D . In the present study, nozzles of $L/D = 5$ to 50 were used for qualitative tests, whereas nozzles of $L/D = 5$ to 20 were used for quantitative tests. The discharge coefficients of these nozzles were measured in the laboratory and were found to range from 0.58 to 0.77 (depending on L/D). These were much lower than the value of 0.98 measured for the Type A nozzles, suggesting the possibility of cavitation in the jet.

(E) In this arrangement, nozzles of Type C were tested. That these nozzles cavitate the jet has been shown by Johnson [2] and Beutin [5]. The results reported here are for a nozzle with a cylindrical pin insert across the flow. The cavitating characteristics of such flows were investigated extensively by Shal'nev et al [9].

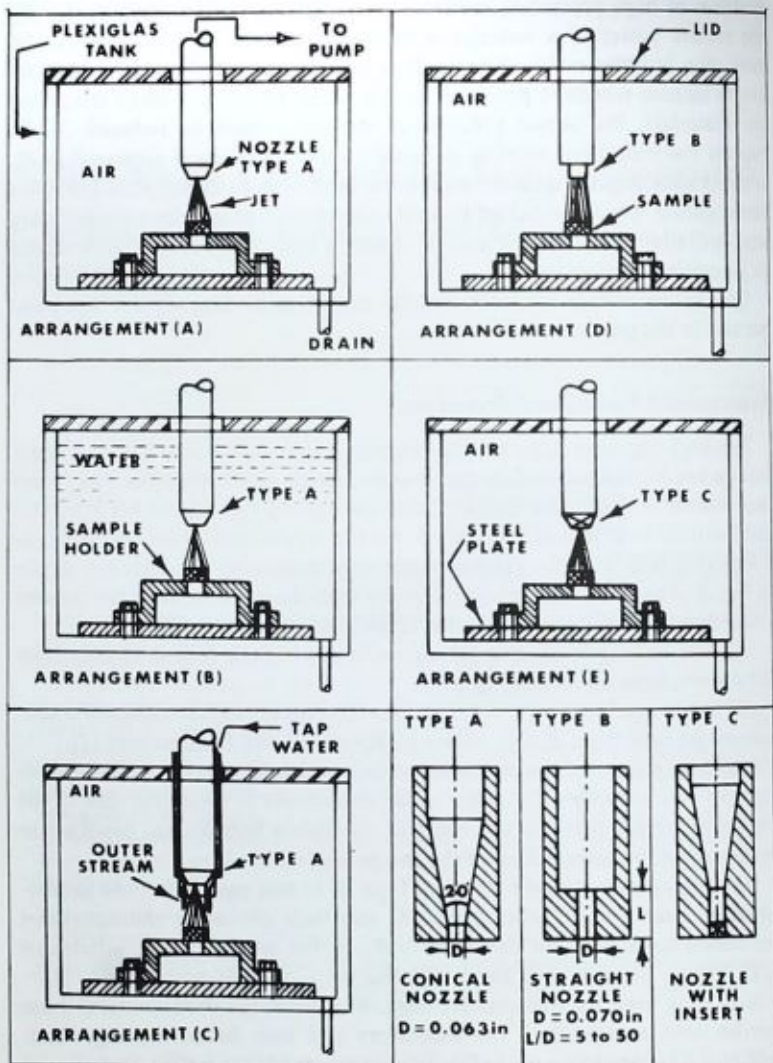


FIG. 1—Arrangement and type of nozzles.

Initial trials were devoted to qualitative study of the erosion caused by these jets. Specimens of cold-rolled annealed copper (Rockwell hardness, B scale = 46 ± 2), aluminium, and brass plates of 2.29-mm (0.090 in.) thickness were used for this purpose. Since these materials work-harden

and also since the measured values of mass loss were small, for quantitative tests, cylindrical specimens of lead (Brinell hardness number = 4HB) of size 3.8 (diameter) by 3.6 cm (1.5×1.4 in) were employed. The homogeneity of these specimens was ascertained by measuring the density (11.36 ± 0.21 g/cm³). The range of experimental variables is summarized in Table 1.

The temperature of the jet was measured by a copper-constantan thermocouple which was located at about 0.76 m (2.5 ft) upstream of the nozzles. Though the temperature varied from day to day (depending on the season), it was maintained at a constant value during the period of the tests.

The main dependent variable which was used to compare the performance of the nozzles was the mass loss, which was obtained by measuring the mass of the specimen before and after exposure to the jet.

Experimental Results and Discussion

The type (size, shape, depth, etc.) of erosion caused by the jets on copper and lead specimens is shown in Fig. 2A-R and Fig. 3A-R. As for the performance, comparison was made on the basis of mass loss with respect to time, taking Arrangement A as reference. This is plotted in Figs. 4 to 7.

Figures 2 and 3 clearly show that each arrangement produces a distinct type of erosion, depending on the material and to a certain extent on the standoff distance (*SD*). For standoff distances less than 2.5 cm (1.0 in.), none of the arrangements produced any perceptible erosion on the copper plates. In such cases the flow was purely radial on the surface of the specimen. The erosion started to become appreciable for values of *SD* > 5 cm (2 in.), as shown in Fig. 2A-D. The flow in this instance was initially radial, then changing instantaneously to conically upward flow, the pattern depending on the type of crater formed. Figure 2A, D, E, R and Fig. 3A show that the irregular or the ring type of erosion, well known in the case of brittle materials [10, 11], also occurs for metals. This type of erosion of metals has also been observed by other investigators [12, 13]. Although exact reasons are as yet unknown, it appears that it is caused by shear due to high-velocity radial flow on the surface of the deformed (due to jet impact) specimen. A closer examination of the crater in Fig. 2D, however, reveals the presence of erosion at the point of impact. It is argued that this is caused by the cavitation bubbles which are generated within the jet due to the vena contracta effect. This is strongly supported by the fact that the same type of craters appeared for tests done in Arrangements B (Figs. 2B and 3C, 3D), C (Figs. 2C, H and 3E, F), and E (Fig. 3Q, R). For standoff distances greater than about 13 cm (5 in.), quite different results were obtained as shown in Figs. 2G—2M and Fig. 3B. What exactly happens in these cases is hard to explain, but it appears that the liquid drops which form due to the breakup of the jet at large standoff distances contribute to the process of

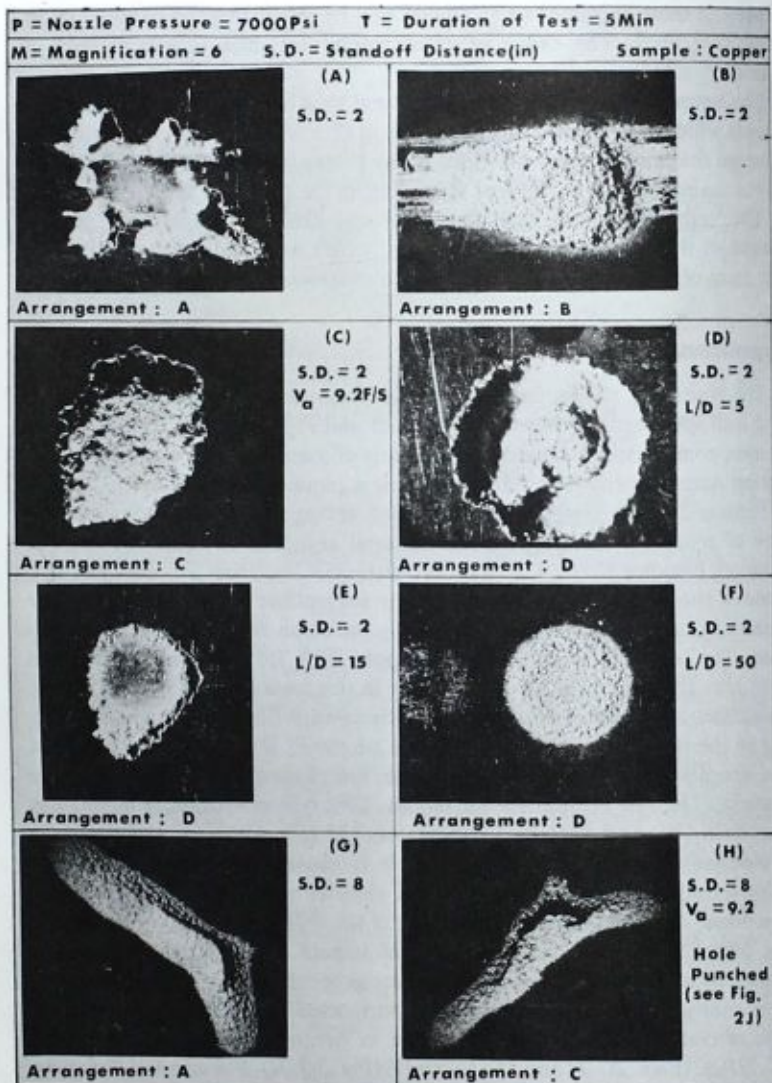


FIG. 2—Photographs of craters caused by different arrangements.

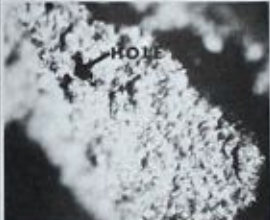





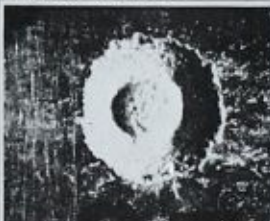

P = 7000Psi		T = 5 Min		M = 6	
Sample : Copper			S.D. (in)		
	(J) Same as 2H except M = 50		(K) S.D. = 8 $V_a = 17.7$	Arrangement : C	
	(L) S.D. = 8 L/D = 15		(M) S.D. = 8 L/D = 50	Arrangement : D	
	(N) S.D. = 7 L/D = 15		(P) S.D. = 5 L/D = 15	Arrangement : D	
	(Q) S.D. = 4 L/D = 15		(R) S.D. = 3 L/D = 15	Arrangement : D	

FIG. 2—(Continued).









$D=0.070$ (1.78mm) } EXCEPT WHERE NOTED $T=4$ min.		$P=5000$ ($3.45 \times 10^7 \text{ N/m}^2$)	
S.D.=3.0 (7.62 cm)		S.D.=6.0 (15.24 cm)	
	(A) ARRANGEMENT : <u>A</u> TYPE : <u>A</u>		(B) <u>A</u> <u>A</u>
	(C) $T=0.5$ <u>B</u> <u>A</u> PENETRATED		(D) <u>B</u> <u>A</u> PENETRATED
	(E) <u>C</u> <u>A</u> $V_a=3.40$ (1.04m/s) PENETRATED		(F) <u>C</u> <u>A</u> $V_a=3.40$ (1.04m/s) PENETRATED
	(G) <u>C</u> <u>A</u> $V_a=9.45$ (2.88m/s)		(H) <u>C</u> <u>A</u> $V_a=9.45$ (2.88m/s)

FIG. 3—Erosion of lead specimens by different arrangements.









$D = 0.070$ (1.78 mm) } EXCEPT WHERE NOTED $T = 4$ min.		$P = 5000$ ($3.45 \times 10^7 \text{ N/m}^2$)	
S.D. = 3.0 (7.62 cm.)		S.D. = 6.0 (15.24 cm.)	
 <p>(J) ARRANGEMENT: $\frac{C}{A}$ TYPE: $\frac{A}{A}$ $V_0 = 18.2$ (5.55) PENETRATED.</p>	 <p>(K) $\frac{C}{A}$ $V_0 = 18.2$ (5.55)</p>		
 <p>(L) $\frac{D}{B}$ $L/D = 5$</p>	 <p>(M) $\frac{D}{B}$ $L/D = 5$</p>		
 <p>(N) $\frac{D}{B}$ $L/D = 20$</p>	 <p>(P) $\frac{D}{B}$ $L/D = 20$</p>		
 <p>(Q) $\frac{E}{C}$ $D = 0.120$ (3.05 mm)</p>	 <p>(R) $\frac{E}{C}$ DIA OF PIN = 0.0625 (1.59)</p>		

FIG. 3—(Continued).

TABLE 1—Range of experimental variables.

P , MPa (psi)	V_0 m/s (ft/s)	SD , cm (in.)	T , min	V_w m/s (ft/s)	Jet Temperature, °C	Comments
34.4 (5000)	26.3 (860)	2.5 to 20.3 (1.0 to 8.0)	5	2.7 to 10.7 (9 to 35)	10	$D = 1.60, 1.78$ mm (0.063, 0.070 in.) $L/D = 2$ to 50
48.3 (7000)	311 (1020)	2.5 to 20.3 (1.0 to 8.0)	5	2.7 to 10.7 (9 to 35)	10	qualitative tests
6.0 (1000)	117 (385)	7.6 (3.0)	0.25 to 10	1.0 to 15.4 (3.4 to 50.6)	12.8 to 24.4	quantitative tests, Temperature was constant for tests done on any particular day
13.8 (2000)	166 (545)	7.6 (3.0)	0.25 to 10	1.0 to 15.4 (3.4 to 50.6)	12.8 to 24.4	
34.4 (5000)	262 (860)	7.6 and 15.2 (3 and 6)	0.25 to 10	1.0 to 15.4 (3.4 to 50.6)	12.8 to 24.4	

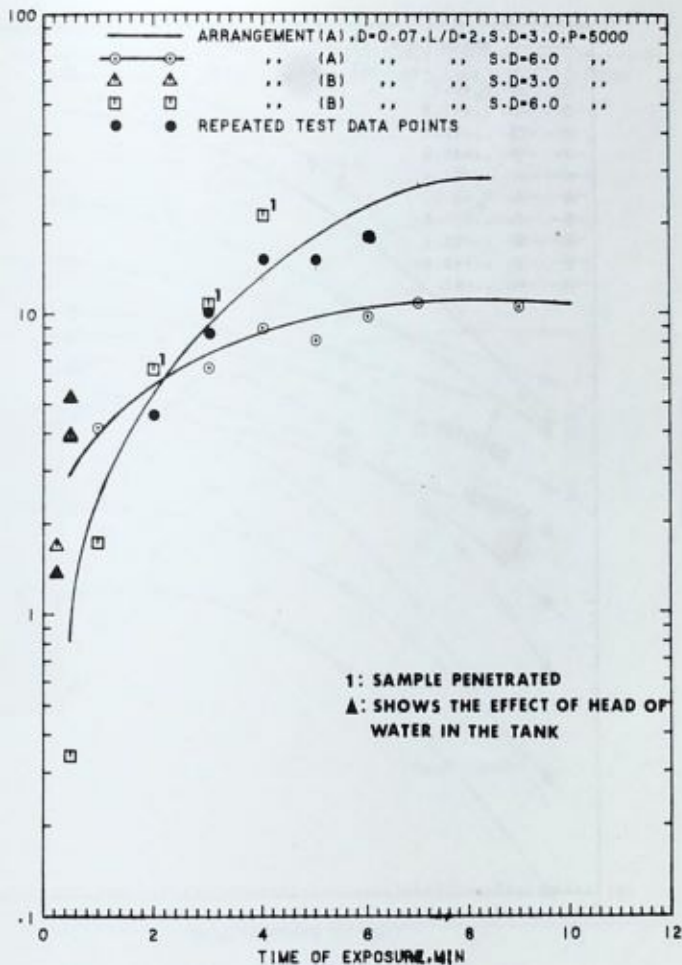


FIG. 4—Comparison of Arrangements B and A.

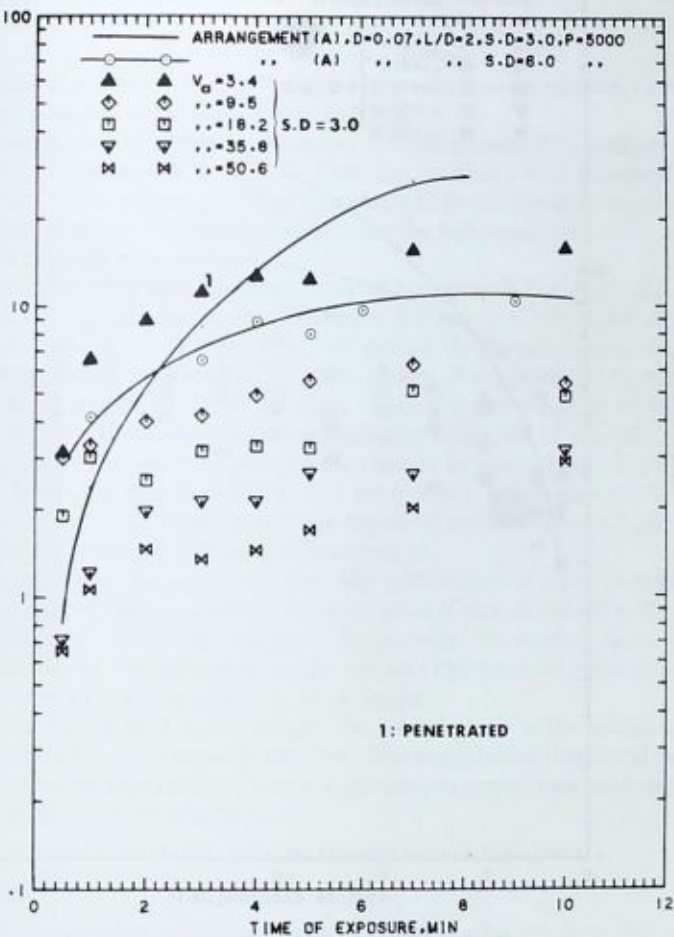


FIG. 5b—Comparison of Arrangements C and A.

EROSION: PREVENTION AND USEFUL APPLICATIONS

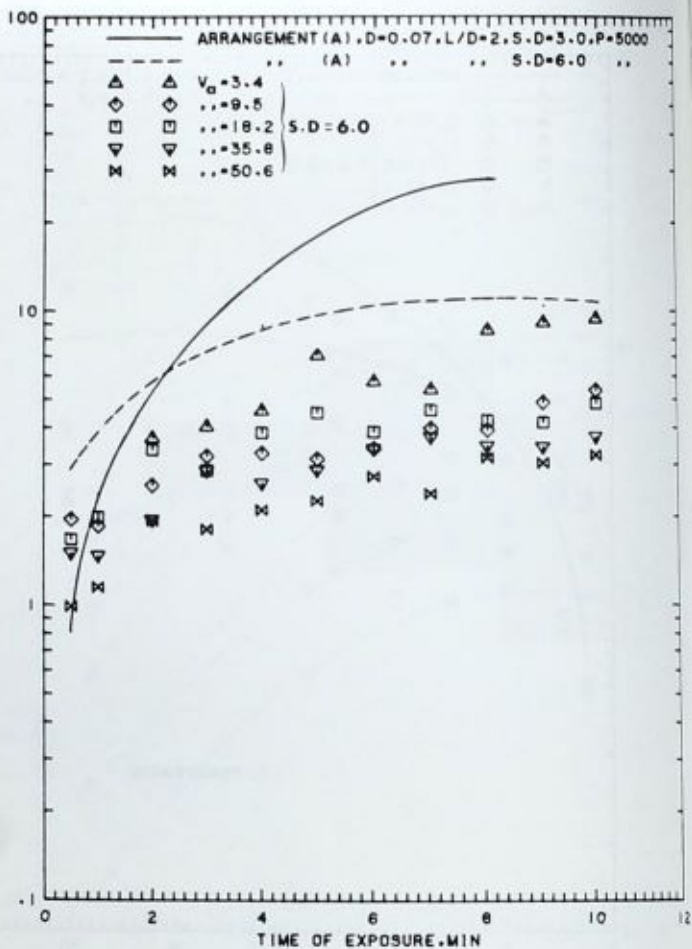


FIG. 5c—Comparison of Arrangements C and A.

erosion (see Fig. 2M for shape of the dents on the surface). Figure 2E, R, Q, P, N, L shows vividly the effect of SD on the nature of the craters produced.

Figure 2J shows a magnified ($\times 50$) view of the crater shown in Fig. 2H. Such microscopic examinations did not reveal clearly any characteristics peculiar to cavitating or noncavitating jets. It should be mentioned, however, that the crater produced by a cavitating jet was much rougher than that caused by a noncavitating jet.

Figure 2H, K and Fig. 3E, G, J show the effect of V_0 on erosion. Since the probability of generation of the cavitation bubbles is a function of the interfacial shear stress, higher V_0 implies lower shear stress and hence less bubbles in the jet, resulting in reduced erosion.

The mass loss of the lead specimens in Arrangement B is compared against Arrangement A in Fig. 4. Since the specimens were completely penetrated within a short period of time, the data do not represent the true mass loss; however, the figure, clearly shows the high destructive power of the cavitating jet.

Figure 5a-c compares the performance of Arrangement C with Arrangement A. In Fig. 5a, the results obtained at 6.9 and 13.8 MPa (1000 and 2000 psi) and $SD = 7.6$ cm (3.0 in.) are plotted. As discussed earlier, the plots show increased mass loss for short periods of exposure and for low values of V_0 . Figure 5b shows the same trends at a pressure of 34.5 MPa (5000 psi). In this instance many specimens were penetrated as indicated in the figure and therefore the true mass loss would be much higher. Plotted in Fig. 5c are the results of $SD = 15.2$ cm (6.0 in.). In this case, though the mass losses were much lower, the depths of penetration were higher compared with the conventional noncavitating jet.

Figure 6a, 6b and Fig. 7 compare the performance of Arrangements D and E against Arrangement A. From the point of view of mass loss, they were inferior to the noncavitating jet. Surprisingly, the standoff distance did not have any significant effect on erosion. The depth of penetration caused by these jets was, as before, much deeper.

The results obtained show strongly that erosive power of the cavitating jets is intense for short times of exposure. This suggests that they would be very effective for applications where it is necessary to employ high traversing speeds of the jet or the specimens.

Conclusions

Tests conducted at moderate standoff distances (≈ 7.6 cm) show that it is possible to recognize the cavitating or noncavitating nature of jets by a visual examination of the craters formed on metals. Erosion was imperceptible for standoff distances less than about 2.5 cm. At standoffs greater than about 15 cm, erosion by droplets was predominant.

On the basis of material loss, Arrangement B performed best for all

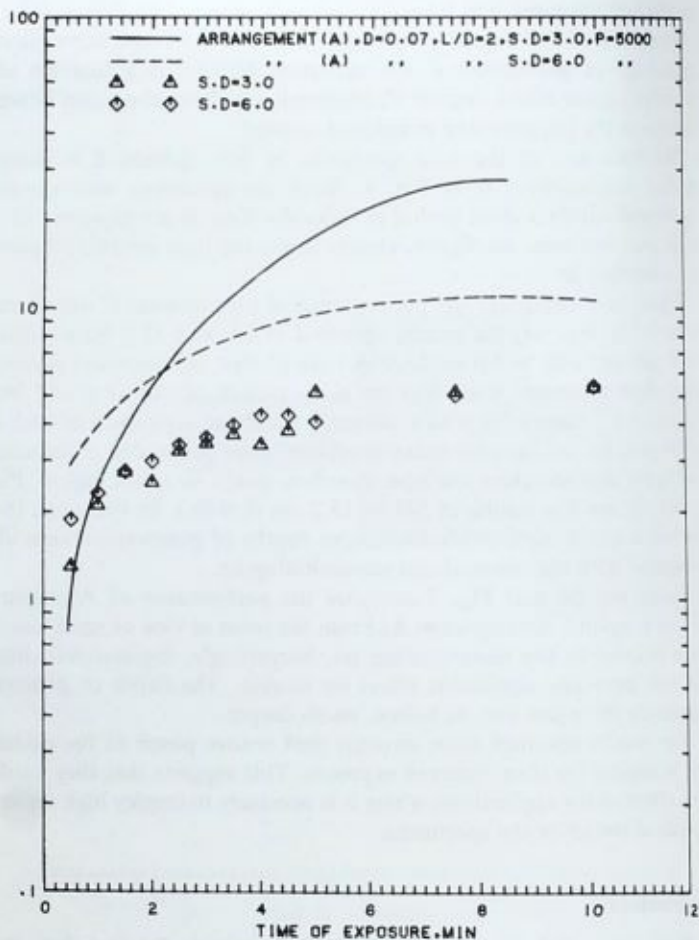
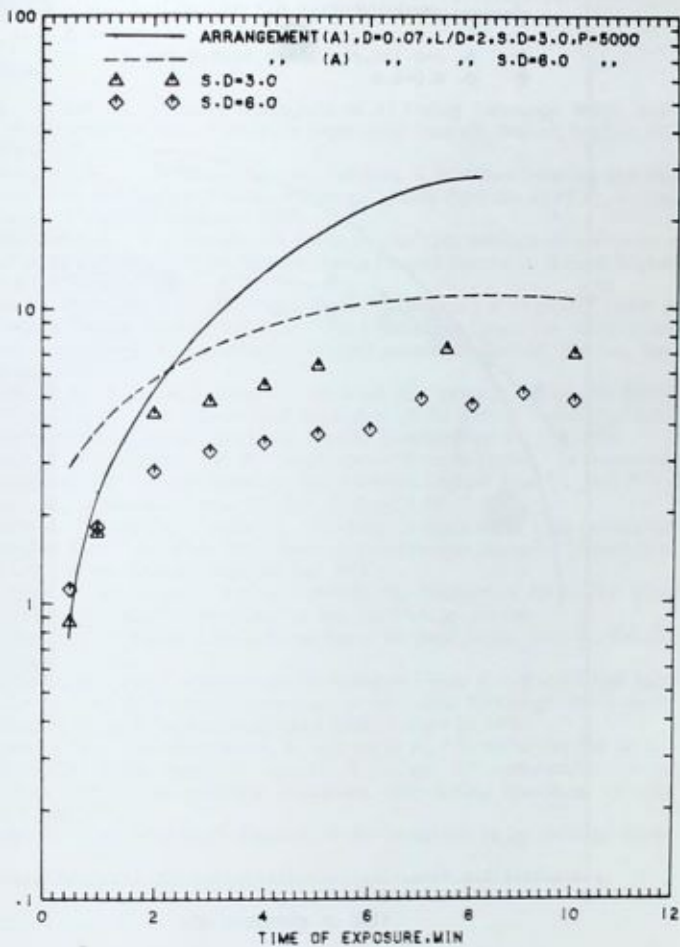


FIG. 6a—Comparison of Arrangements D and A, $L/D = 5$.

FIG. 6b—Comparison of arrangements D and A, $L/D = 20$.

EROSION: PREVENTION AND USEFUL APPLICATIONS

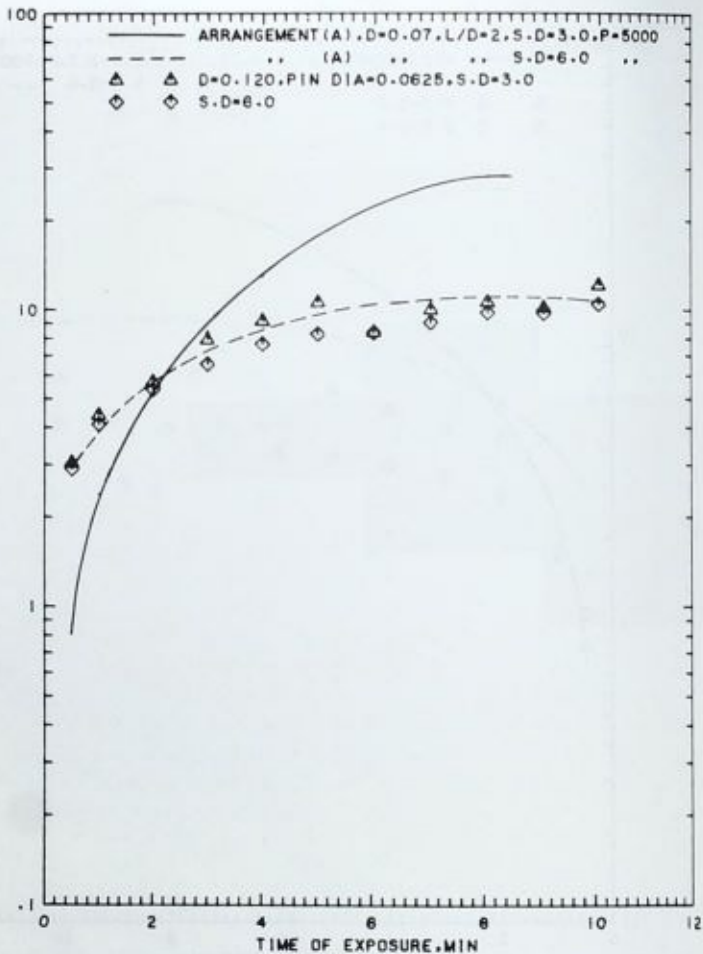


FIG. 7—Comparison of Arrangements E and A.

periods of exposure and standoff distances. This was followed by Arrangement C for short periods of exposure, smaller standoffs, and for low values of V_s .

The results suggest that the cavitating jets would be attractive for material removal or for deeper penetration at high traverse speeds. However, to fully assess their capabilities, further study on erosion of brittle materials is required.

References

- [1] 1st, 2nd and 3rd International Symposia on Jet Cutting Technology, British Hydromechanics Research Association, Fluid Engineering, Cranfield, Bedford, England, 1972, 1974, and 1976.
- [2] Johnson, V. E., Jr., Thiruvengadam, A., and Kohl, R. E., "Rock Tunneling with High-Speed Water Jets Utilizing Cavitation Damage," ASME Paper No. 68-FE-42, American Society of Mechanical Engineers, 1968.
- [3] Lichtarowicz, A., "Experiments with Cavitating Jets," 2nd International Symposium on Jet Cutting Technology, British Hydromechanics Research Association, Bedford, England, Paper D1, April 1974.
- [4] Conn, A. F., Rudy, S. L., and Mehta, G. D., "Development of a CavijetTM System for Removing Marine Fouling and Rust," 3rd International Symposium on Jet Cutting Technology, British Hydromechanics Research Association, Bedford, England, Paper G4, May 1976.
- [5] Beutin, E. F., Erdmann-Jesnitzer, F., and Louis, H., "Influence of Cavitation Bubbles in Cutting Jets," 2nd International Symposium on Jet Cutting Technology, British Hydromechanics Research Association, Bedford, England, Paper D3, April 1974.
- [6] Harris, H. D. and Brierley, W. H., "Application of Water Jet Cutting," 1st International Symposium on Jet Cutting Technology, BHRA Bedford, England, Paper G1, April 1972.
- [7] Rouse, H., *La Houille Blanche*, Jan.-Feb. 1953, pp. 9-19.
- [8] Pearce, I. D. and Lichtarowicz, A., "Discharge Performance of Long Orifices with Cavitating Flow," 2nd Fluid Power Symposium British Hydromechanics Research Association, Bedford, England, Paper D2, Jan. 1971.
- [9] Shal'nev, K. K., Varga, I. I., and Sebestyen, D., *Philosophical Transactions of the Royal Society*, London, Series 1110, Vol. 260, July 1966, pp. 256-266.
- [10] Bowden, F. P. and Field, J. E. in *Proceedings of the Royal Society*, Series A., Vol. 282, 1964, pp. 331-352.
- [11] Rehbinder, G., "Some Aspects on the Mechanism of Erosion of Rock with a High Speed Water Jet," 3rd International Symposium on Jet Cutting Technology, British Hydromechanics Research Association, Bedford, England, Paper E1, 1976.
- [12] Beutin, E. F., Erdmann-Jesnitzer, F., and Louis, H., "Studies of Material Surfaces Subjected to Single Liquid Jet Impact," *Proceedings*, 4th International Conference on Rain Erosion and Associated Phenomena, Neus Schloss, Meersburg, Germany, Vol. 1, May 1974.
- [13] Smith, D. G. and Kinslow, R., *Experimental Mechanics*, Vol. 16, Jan. 1976, pp. 21-25.

Cavitating Jet Apparatus for Cavitation Erosion Testing

REFERENCE: Lichtarowicz, A., "Cavitating Jet Apparatus for Cavitation Erosion Testing," *Erosion: Prevention and Useful Applications, ASTM STP 664*, W. F. Adler, Ed., American Society for Testing and Materials, 1979, pp. 530-549.

ABSTRACT: A submerged cavitating jet is used to erode a specimen placed in its path. The erosion depends primarily on the jet velocity, the downstream pressure, and the standoff distance of the specimen. An apparatus for erosion testing based on this principle is described. Results are presented showing the effect of these parameters on erosion. They indicate that scaling should be carried out on the basis of constant cavitation number. The results show that the method is suitable for cavitation erosion testing and that testing time and jet velocity (and hence the upstream pressure) can be traded one against the other provided that the cavitation number remains constant. In this method, all of the variables can be controlled independently. The method offers the advantages associated with flow-induced cavitation together with the short testing time offered by magnetostriction devices.

KEY WORDS: erosion, cavitation, liquid jet cutting, scaling

Various test techniques are used to investigate the resistance of materials to cavitation erosion. In one of these, a test specimen is vibrated at a high frequency (20 kHz) in an appropriate fluid. Cavitation occurs at the surface of the specimen as a result of the high accelerations produced. In this test the cavitation number (σ) cannot be defined, because the velocity is not involved at all. This method provides a simple and not very expensive way for relative grading of different materials, but the results are difficult to correlate with flow situations usually met in practice. The testing times are relatively short and are measured in hours. In other methods, cavitation is produced in a low-pressure region of a venturi, or behind a bluff object placed in a water tunnel or even on a rotating disk immersed in a chamber which can be pressurized. In these methods both the velocity and the surrounding pressure

¹Senior lecturer, Department of Mechanical Engineering, University of Nottingham, Nottingham, U.K.

can be changed independently so that the cavitation number can be controlled at will. The test conditions are much more closely related to the conditions occurring in practice. The flow velocities are not very high (up to say 40 to 50 m/s); consequently tests take a long time and the apparatus tends to be bulky. This paper describes a new method of testing recently proposed by the author [1,2]² which uses a high-velocity (greater than 100 m/s) submerged liquid jet. In such a jet, cavitation occurs in shear layers provided that the velocity is sufficiently high, and the back pressure not too large. If a target is placed within this cavitating region, considerable cavitation erosion will occur.

For the past three years, work has been going on at Nottingham University to develop this new method. Some of the results are given by Nolan [3], Stawski [4] and Munton [5]. Recently Kleinbreuer [6] published a paper in which a similar testing technique is proposed.

Principle of Operation

In a long orifice (or a short tube) the flow after separation at the sharp inlet corner reattaches itself to the orifice bore and encloses a separation region. As the pressure difference across the orifice is increased, the pressure in the separated region decreases until eventually cavitation occurs when the vapor pressure is reached. As the pressure difference is further increased, the now cavitating separation region will extend in length till eventually it will outgrow the orifice length and will emerge as a cavitation tail outside the orifice. The flow is now choked, because it depends only on the upstream pressure (and on the vapor pressure, which is constant and usually very small) and is independent of the downstream pressure [7]. The orifice is said to be "supercavitating." As the upstream pressure is increased or the downstream pressure is reduced, cavitation intensity increases.

It should be noted here that since the cavitation bubbles collapse downstream of the nozzle there is no damage to the orifice. This is confirmed by the fact that the same nozzle has been used throughout all the tests carried out at Nottingham and, as yet, no detectable change in the nozzle characteristics have been found.

The cavitating tail emerging from the orifice appears to the eye to be very steady in both space and time. Its appearance and the noise produced depend very much on the cavitation number and on the air content of the liquid used. A full discussion of these effects is given by Lichtarowicz and Pearce [8].

A specimen placed in the region where cavitation bubbles collapse will be quickly eroded and the erosion can be quantified by measuring the mass lost in a given time.

²The italic numbers in brackets refer to the list of references appended to this paper.

The cavitation number is usually defined as

$$\sigma = \frac{p_d - p_v}{\frac{1}{2} \rho v^2}$$

and can be modified to

$$\sigma = \frac{p_d - p_v}{p_u - p_d} = \frac{p_d - p_v}{\Delta p}$$

where

p_u, p_d, p_v = upstream, downstream, and vapor pressures, respectively,
 v = velocity through the orifice, and
 ρ = density of the fluid.

All pressures are absolute. In many cases the vapor pressure is negligibly small when compared with other pressures, so that the cavitation number reduces to

$$\sigma = \frac{p_d}{p_u}$$

The function of the orifice bore, which must be at least one diameter long, is to stabilize the cavitation bubble especially at high cavitation numbers near cavitation inception [7].

Apparatus

Figure 1 shows an arrangement of the test chamber. A cavitating jet supplied from a pressure source p_u discharges into the test chamber held at the required constant pressure p_d . A circular specimen (Fig. 2) is mounted coaxially with the jet in such a way that the separation between the nozzle and the target can be set to any desired value by adjusting the screws locating the holder. The nozzle itself (Fig. 3) consists of a synthetic sapphire orifice jewel clamped in position by the nozzle holder. The sapphire was chosen as it provides cheaply a well-finished nozzle. The conical entry increases its discharge coefficient without affecting its general cavitating performance.

Windows were provided on both sides of the chamber so that cavitation could be observed. The whole assembly was designed to withstand 35-MPa pressure, and it is suitable for use with water or with oil.

Pressures were measured by appropriate test gages while the temperature was measured by a mercury in glass thermometer located in a well just downstream of the chamber exit.

A test chamber assembly which would be required for routine test work

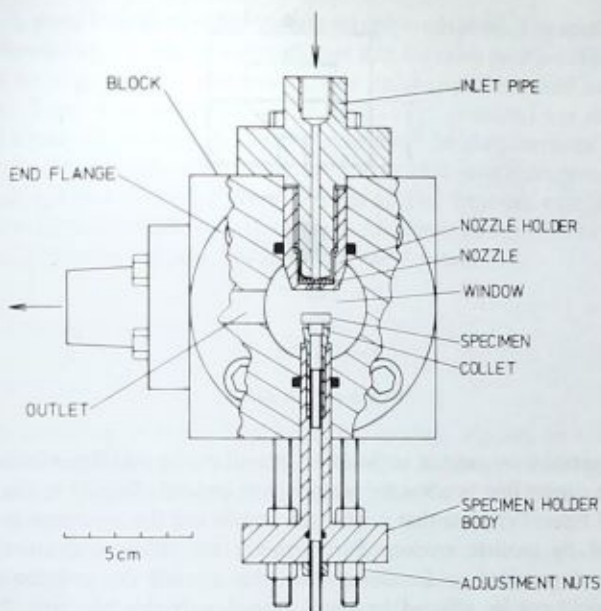
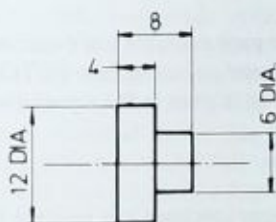


FIG. 1—Jet cavitation erosion rig.

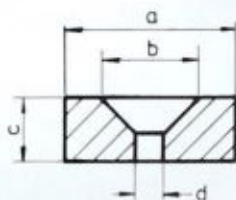


ALL DIMENSIONS ARE mm

FIG. 2—Specimen for cavitation erosion.

can be considerably simplified, as the existing unit incorporated additional features that enabled it to be used for other purposes.

The unit was supplied from an existing laboratory facility; hence only the essential features of the system will be specified. Both upstream and downstream pressures are held constant during the test, but their settings



$$a = 3.64 \text{ mm}$$

$$b = 1.83 \text{ ''}$$

$$c = 1.50 \text{ ''}$$

$$d = 0.477 \text{ ''}$$

FIG. 3—Nozzle details.

may be varied from one test to the other. An oil cooler was fitted in the high-pressure supply line to allow for temperature control. Supply to the nozzle was well filtered (5μ) so that neither the nozzle nor the specimen would be damaged by particle erosion. Furthermore, an efficient debris-removal system was provided on the downstream side so that the pressure control valve would not be affected by small eroded particles blocking the flow passages. A fine wire mesh was found to be sufficient on the rig used. Facilities for a quick buildup and cutoff of the supply to the test chamber and for automatic test timing were provided to enable short test runs to be made.

As the hydraulic power pack available could use only hydraulic oil, all the tests to date have been carried out using Esso NUTO H32 hydraulic oil. The exact specification of the oil is given in the Appendix.

Testing Procedure

Before each test a dummy specimen was inserted in the test chamber and the machine run so that all the controls could be preset to the desired values and a steady temperature could be reached. A previously weighed specimen was then inserted, the automatic timing was preset, and the rig started up with the flow to the test chamber shut off. As soon as the required pressure built up, the valve was opened and the timer started. Usually, small adjustments had to be made to the settings. Some adjustments were also required to the cooling water flow since there was no thermostatic control. After the machine had stopped the specimen was weighed again to determine mass loss and the cumulative erosion rate (CER). CER is defined as the total mass loss divided by the elapsed time t .

All specimens were weighed down to 0.1 mg, but in a few cases a machine capable of weighing down to 0.01 mg was used to determine the initial ero-

sion. In some tests the eroded surface was photographed. The specimen then was inserted again, taking care to locate it in the same position. This was ensured by alignment of two marks, one on the specimen and one on the holder. Tests were also made where the standoff distance l was altered.

All testing so far has been done to determine the characteristics of the apparatus; consequently aluminium specimens were used throughout to keep the testing times shorter. A few specimens of other materials were tested to illustrate the practicability of the method. All aluminium specimens were heat treated to ensure uniform hardness (see the Appendix).

Experimental Work

Test program

The cavitation intensity, and hence the erosion, depends on a number of parameters which can be conveniently divided into a number of groups. As the number of parameters is large, it was possible to test the effects of only some of them.

The first group of variables consists of geometrical parameters describing the size of the unit. These comprise the nozzle diameter d , standoff distance l , specimen diameter D , and the chamber size. The nozzle size was determined mainly by the capacity of the available pumping equipment and was kept constant throughout all the work. Only the standoff distance l was changed to test for optimum distance. The chamber size (Fig. 1), that is, both the diameter and width, were made sufficiently large so as not to affect the flow pattern as the standoff distance was altered or the flow pattern changed as the erosion of the test specimen progressed. It was hoped that the 10-mm-diameter specimens would be sufficiently large for erosion not to be affected by the specimen diameter, but it was found later that at higher upstream pressures the eroded area covered the whole of the specimen face. Additional tests were made which indicated that the diameter had to be increased to 12 mm.

The second group of variables describes operating conditions and comprises the upstream and downstream pressures as well as the operating temperature and the air content of the liquid. Air content was not investigated here at all. It is known that, for vibratory tests, erosion rate peaks with a relatively flat plateau between 40 and 70°C; thus most of the current tests were carried out within this temperature range.

The main part of this work describes the effects of various pressure changes on erosion. Tests were made at

1. constant cavitation number $= p_d/p_u$,
2. constant downstream pressure, and
3. constant upstream pressure.

The last group comprises "materials" parameters, that is, the variation of

the specimen material and its state and the type of liquid used. As mentioned previously, only one aluminium and one liquid were used. A few steel specimens were tested to demonstrate that the method is suitable for other materials.

Experimental Results

As the jet leaves the nozzle, cavitation is confined to its circumference and, as it travels along, cavitation spreads both into and out of the jet. Eventually it will decay. When a jet strikes a plate target placed normal to its axis, the flow is deflected radially outward and a stagnation region is formed at the center. Thus erosion on a target will occur in a ring around the central uneroded area. If the standoff distance l is increased, the central area will diminish. Similar effects can be obtained by increasing σ and holding l constant. Figure 4 shows the test rig in operation. The jet is made visible by the cavitation cloud surrounding it. The erosion pattern can be seen in Fig. 5, which shows various stages of erosion of an aluminium specimen. Machining marks at the center remain visible for a very long time and they disappear only as the center region is slowly eroded away from the rim inwards as the specimen surface geometry changes. The absence of cavitation at the center was confirmed by viewing a similar, but scaled up, cavitating jet through a transparent Perspex specimen mounted in a rig used for other tests.

Figure 6 shows the mass loss (Δm) and the cumulative erosion rate (CER) time graph for Specimen 7. The shape of both curves is very typical of all the results obtained. Figure 5 shows the photographs of the eroded surface of this specimen at various stages of erosion. The feature already mentioned is the ring pattern of erosion which gradually extends inwards and outwards. At longer erosion times, deep pits are visible and the central noneroded core has disappeared, leaving a rather large hole in the center. Under these circumstances the flow pattern around the specimen is affected, because the flow no longer leaves the surface radially but is deflected backwards. This occurs after approximately 1200 s exposure in this particular case. The effective standoff distance has by now increased, but as this occurs at the exposure times considerably longer than the time required to reach the peak erosion rate, it does not further affect correlations. For example, the mean depth of erosion for Specimen 7 shown in Figs. 5 and 6 is only the order of 0.15 mm at the time of peak erosion rate.

Figure 7 shows a set of cumulative erosion rate curves obtained at constant cavitation number $\sigma = 0.025$. As the upstream pressure is increased from 8 MPa upwards, the flat plateau associated with the steady-state zone becomes shorter until eventually it disappears altogether, leaving a peak which becomes more pointed as the pressure is further raised. It should be noted here that the maximum pressure used in all this work was only 20 MPa, while the ultimate tensile strength of aluminium is 67 MPa.

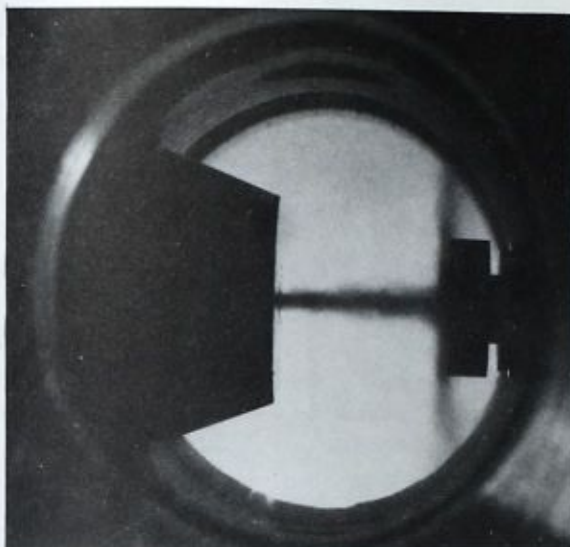


FIG. 4—Cavitating jet in operation.

Figure 8 shows initial mass loss for two specimens. In both these cases a more sensitive weighing machine was used to illustrate that, in the incubation zone, material loss occurs at very early stages. A photograph of the specimen (No. 19) in the early stages of erosion is shown in Fig. 5. Here σ is larger and consequently the central uneroded area is much smaller.

As suggested by Thiruvengadam [9], the erosion rate versus time curves were normalized, taking as the reference values the peak erosion rate and the time to reach that peak. All of the relevant erosion rate curves obtained in this study were so correlated. Figure 9 shows most of the results plotted in this way. Other data which are not shown also fall within the two bounding curves drawn around these points. Table 1 gives the peak erosion rates and the actual times to reach that peak. Thus, it is possible from the graph and the erosion rate table to calculate the actual time taken to reach that rate and hence the mass lost. The region around the incubation zone is not sufficiently well covered, since the balance used in most of the tests was not sufficiently sensitive at these small erosion rates.

Tests at Constant Cavitation Number and at Constant Back Pressure

The peak erosion rate for two constant values of the cavitation number is shown plotted against the upstream pressure in Fig. 10, and Fig. 11 shows

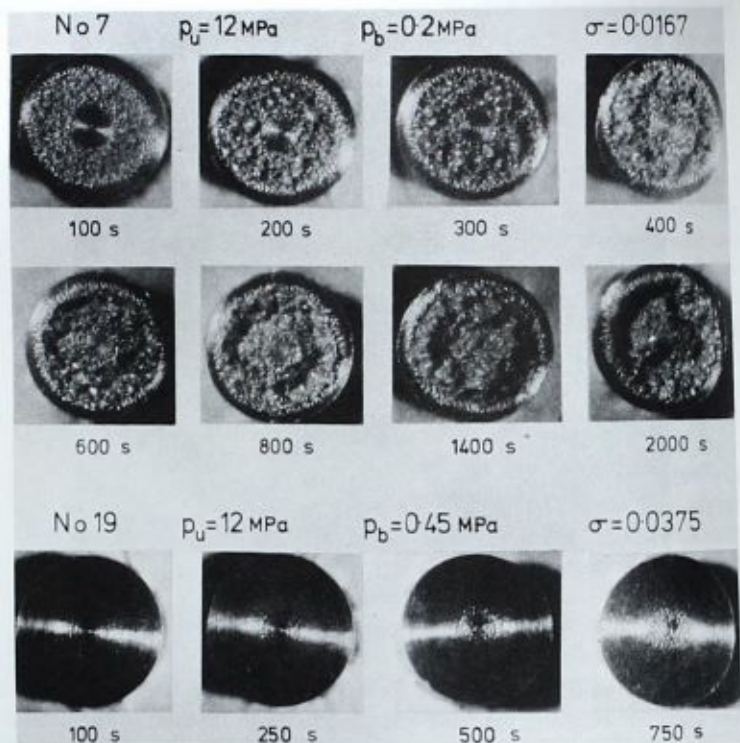


FIG. 5—Stages of erosion in aluminum specimens.

the time to reach the peak, plotted also against the upstream pressure. It can be seen that

$$\text{peak erosion rate} \propto \text{upstream pressure}^n \propto \text{jet velocity}^{2n}$$

and that the time to reach the peak T is nearly linearly related to the upstream pressure. The value of n and the slope of the linear graph both depend on the cavitation number. The present tests show that for pure aluminium

$$n = 4.2 \quad \text{for} \quad \sigma = 0.0143$$

$$n = 3.5 \quad \text{for} \quad \sigma = 0.025$$

On the same graphs the corresponding values obtained at constant back pressure are also shown. These do not form simple relationships, because

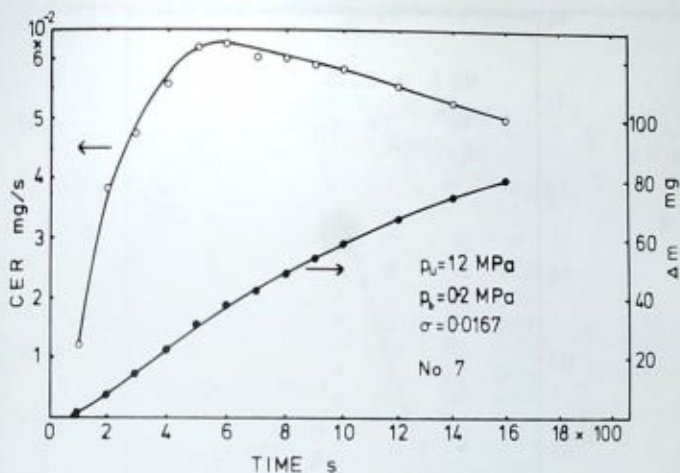
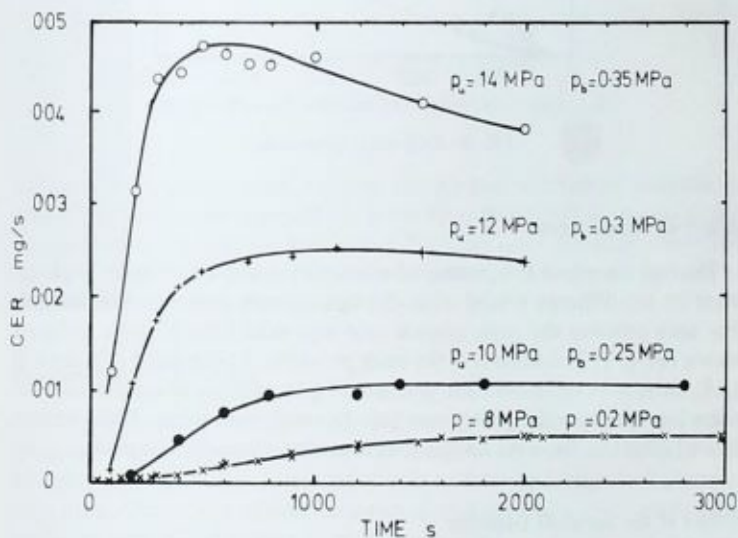


FIG. 6—Typical mass loss and cumulative erosion rate time graphs.


 FIG. 7—Cumulative erosion rate for various pressures at constant $\sigma = 0.025$.

they were not taken under dynamically similar conditions and because some scale effects are present.

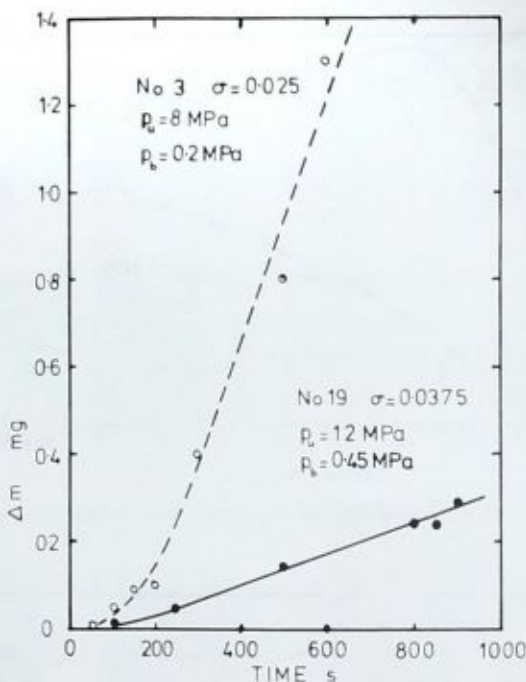


FIG. 8—Early stages of erosion.

Effect of Back Pressure

The next two sets of tests were conducted with upstream pressure kept constant (at two different values) while the downstream pressure was changed. For each pressure the peak erosion rate was established; these rates are shown in Fig. 12 as functions of the back pressure. As expected (Knapp et al [10]), there is an optimum back pressure to give maximum erosion rate and there is a corresponding minimum time to reach that peak. These results, like all others so far, were obtained at a constant standoff distance.

Effect of the Standoff Distance

A number of tests were also made where pressures were kept constant and the standoff distance was varied from 5 to 18 mm. The peak erosion rate obtained at each standoff distance is shown plotted against the standoff distance in Fig. 13. As expected, there is an optimum separation at which the erosion rate is a maximum, but this distance depends on flow conditions as shown by Kleinbreuer [5]. Kleinbreuer kept the upstream pressure constant

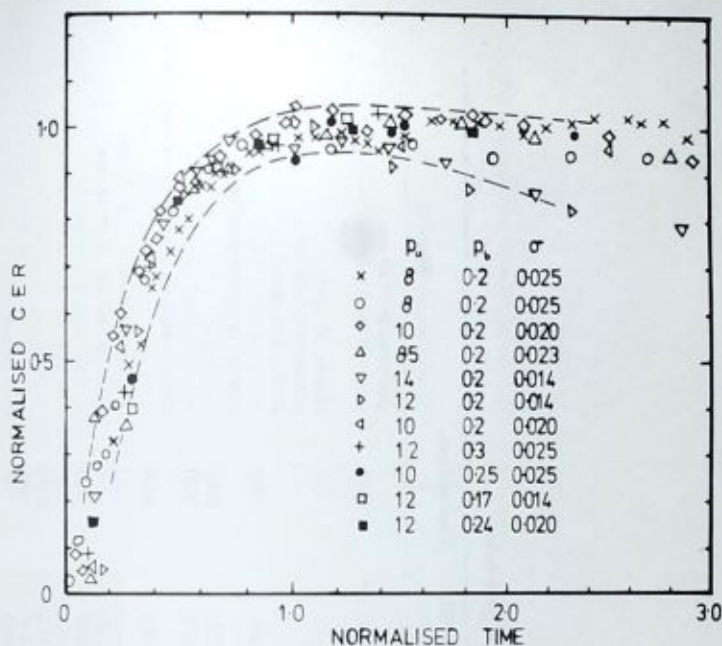


FIG. 9—Normalized cumulative erosion rates—time graph.

and altered the downstream pressure, and for each value of the downstream pressure he varied the standoff distance. At each distance he measured the material loss occurring in a fixed time (17 h in his case). His results show that for each value of the standoff there is an optimum downstream pressure to give maximum erosion in a specified time.

Tests on Other Materials

To show that the test rig is suitable for use with other materials, a few specimens of mild steel (EN3) were tested; the results are shown in Fig. 14. In 8 h, about 62 mg of steel were eroded with a jet having a stagnation pressure of 20 MPa. Tests on a similar material carried out elsewhere in a vibratory apparatus working at its maximum power resulted in a mass loss of less than 50 mg in the same time.

Discussion

The tests described show some of the characteristics of the cavitating jet testing apparatus. They indicate that the method is suitable for testing of

TABLE 1—Summary of test results.

Specimen No.	p_{uc} , MPa	p_b , MPa	σ	Peak ER, mg/s	Time to Peak, s	Remarks
1	8	0.2	0.025	specimen: $D = 10$ mm
2	8	0.2	0.025	0.0053	2400	...
3	8	0.2	0.025
4	8	0.4	0.050	erosion too small
5	8	0.3	0.0375	erosion too small
6						dummy specimen
7	1.2	0.2	0.167	0.062	600	...
8-14						erosion outgrowing specimen
15	10	0.2	0.02	0.034	1800	...
16	10	0.2	0.02	0.034	1800	...
17-23						erosion outgrowing specimen—abandoned
24	85	0.2	0.0235	0.055	3000	...
25
26	dummy specimen
27	14	0.2	0.0143	0.061	750	specimen size test, $D = 12$ mm
28	12	0.2	0.0167	0.051	550	...
29	10	0.2	0.020	0.032	2000	...
30	14	0.35	0.025	0.048	600	...
31	14	0.2	0.0143	0.059	750	...

 $D = 18$ mm

32	14	0.35	0.025
33	12	0.3	0.025	0.0254	1200	...
34	10	0.25	0.025	0.0107	1800	...
35-39	various check specimens
40	12	0.172	0.0143	0.027	1000	$D = 12$ mm
41	12	0.240	0.020	0.054	800	from this test down: $D = 12$ mm grain size and heat treatment checks
42-50	14	0.35	0.025	check runs at different standoff distances abandoned
52-55	14	0.35	0.025	tests at 10, 13, 5, 11.5, 18 mm standoff
57-61	14	0.35	0.025	heat treatment checks
62-65	14	0.35	0.025	no measurable erosion after 1000 s
66	10	0.48	0.05	no measurable erosion after 1000 s
67	12	0.6	0.05
68	10	0.14	0.0143	0.012	1200	...
69	16	0.23	0.0143	0.108	550	...
70	8	0.35	0.0437
71	10	0.35	0.035	no measurable erosion after 1000 s
72	16	0.35	0.022	0.095	350	error in weighing
73	16	0.112	0.007	Δm to σ small to weigh
74	16	0.4	0.025	0.079	700	...
77	20	2.86	0.0143	0.174	320	...
78	18	2.57	0.0143	0.134	400	...

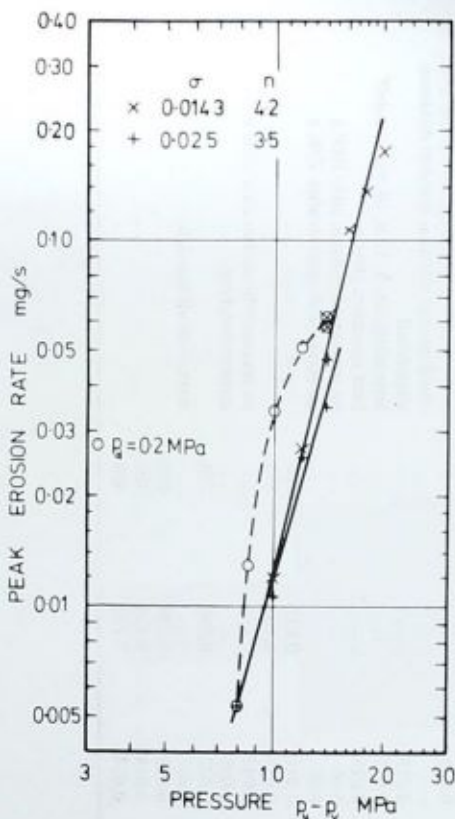


FIG. 10—Peak erosion rate pressure relationships.

materials for their resistance to cavitation erosion. The method offers many advantages over existing methods. The apparatus is small and utilizes flow effects to produce cavitation; hence it offers all the advantages of venturi and tunnel-type devices without their main drawbacks of size and long testing times. The testing times can easily be adjusted by choosing a suitable upstream pressure, and the results can then be scaled up or down easily as long as the cavitation number is kept constant.

Care must be taken, however, not to use too high pressures for erosion testing, as the material can be damaged by the jet or even cut by it. If one is in doubt, cavitation can easily be suppressed by raising both the upstream and downstream pressures. It must be remembered, however, that since in jet cutting it is the velocity which is important, the velocities under non-cavitating and cavitating conditions should be the same. This results in

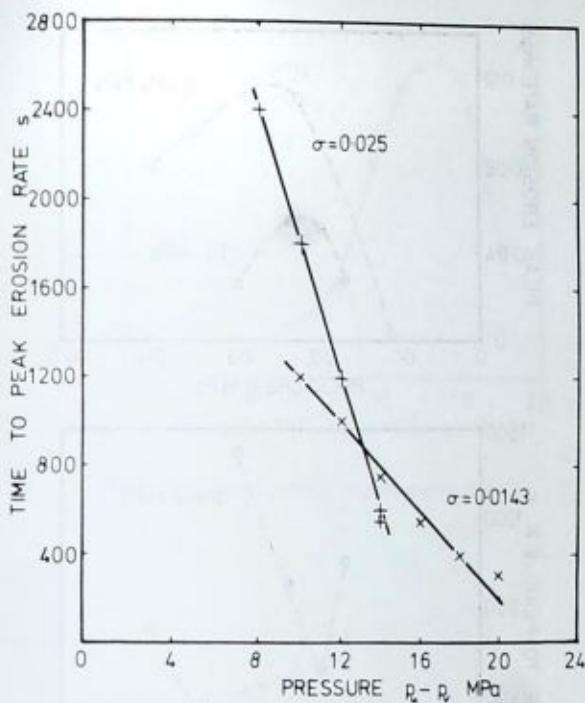


FIG. 11—Time to reach peak erosion rate.

$$\begin{aligned} (p_u - p_d)_{\text{noncavitating}} &= (p_u - p_v)_{\text{cavitating}} \\ &\approx p_u_{\text{cavitating}} \end{aligned}$$

The importance of scaling laws has been emphasized by the constant-cavitation-number and constant-back-pressure tests (Fig. 10).

Further tests should be carried out to extend the range of the test results and to investigate the effect of nozzle size. This is especially important since the power required to drive the rig is proportional to the nozzle cross-sectional area. In the present unit the maximum power dissipated by the jet was only 620 W. Thus a 2-kW power pack would be sufficient to drive the unit.

As a testing device, the unit should be simple to use and preferably the number of variable parameters should be minimized. Therefore, it is suggested that testing be done at a fixed standoff distance as was done in these tests, irrespective of whether it is optimum or not for the particular flow condition. The geometrical similarity essential for scaling is also retained.

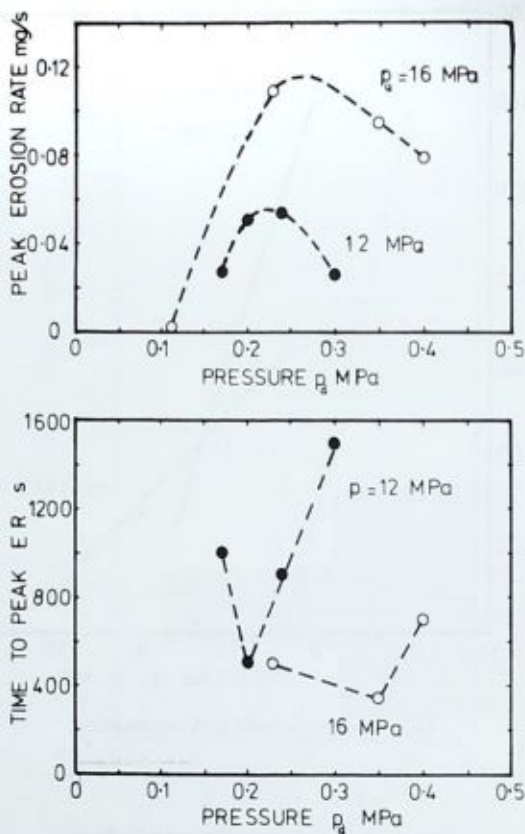


FIG. 12—Effect of downstream pressure on peak erosion rate and on time to reach the peak.

Good-quality pressure-regulating valves must be used in the testing because the erosion is very sensitive to changes in both pressures.

Conclusions

The tests described show that the cavitating jet method of testing provides a viable alternative to the existing methods of cavitation erosion testing. The apparatus is simple, pressures required are within current industrial practice (20 MPa) and, above all, the flow parameters can be easily controlled independently.

The importance of testing at a constant cavitation number to avoid scale effects was clearly demonstrated.

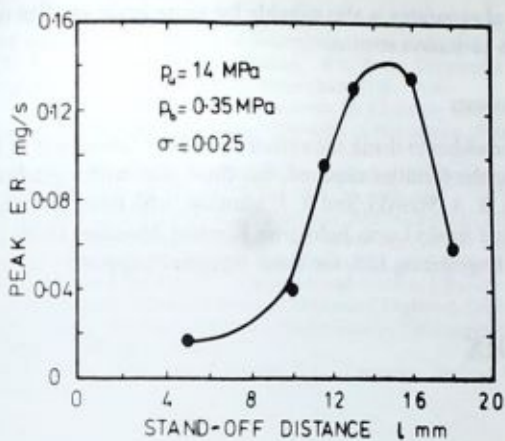


FIG. 13—Effect of standoff on peak erosion rate.

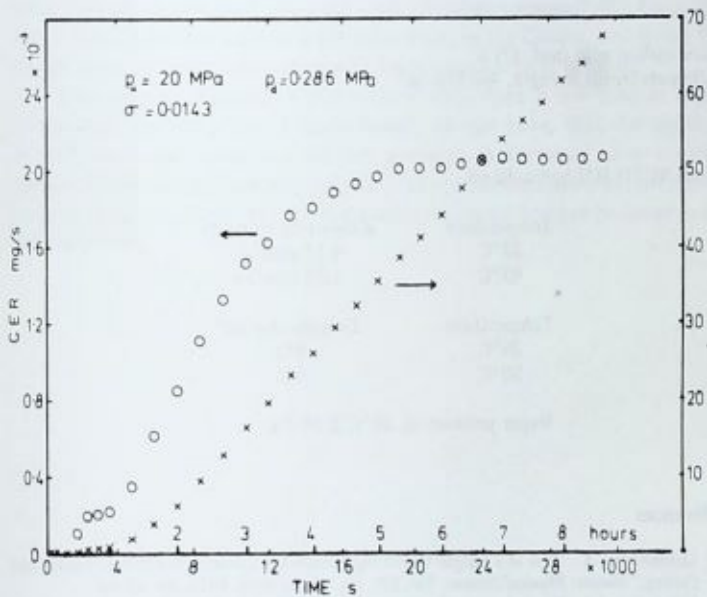


FIG. 14—Tests on EN 3 mild steel.

This type of apparatus is also suitable for more basic studies on cavitating flows and on cavitation erosion.

Acknowledgments

The author wishes to thank the authorities of the University of Nottingham for providing the facilities required, his final year undergraduate students M. D. Nolan, T. S. Stawski, and R. J. Munton, who have carried out most of these tests, and finally Lucas Industries Kinnear Moodie (1973) Ltd. and the Hamworthy Engineering Ltd. for some financial support.

APPENDIX

Properties

Aluminium (99.6 percent pure)

Ultimate tensile strength, 67.4 MN/m²
 Vickers Hardness Number range, 21.5 to 23.8
 Heat treatment: heat for 2 h @ 400°C. Cool in air.

Steel

Low-carbon mild steel, EN 3
 Ultimate tensile strength, 460 MN/m²

Oil

Esso NUTO H32 hydraulic oil

Temperature	Kinematic viscosity
38°C	4.53 mm ² /s
93°C	1.55 mm ² /s

Temperature	Density, kg/m ³
30°C	843
50°C	831

Vapor pressure @ 38°C 2.26 Pa

References

- [1] Lichtarowicz, A., "Use of a Simple Cavitating Nozzle for Cavitation Erosion Testing and Cutting," *Nature: Physical Science*, Vol. 239, No. 91, 25 Sept. 1972, pp. 63-64.
- [2] Lichtarowicz, A., "Experiments with Cavitating Jets," *Proceedings, Second International Symposium on Jet Cutting Technology*, Paper D1, British Hydromechanics Research Association, Fluid Engineering, Cambridge, U.K., 1974.

- [3] Nolan, M. D., "New Methods of Cavitation Erosion Testing," B.S. thesis, Department of Mechanical Engineering, University of Nottingham, Nottingham, U.K., 1975.
- [4] Stawski, T. S., "Cavitation Erosion Testing," B.S. thesis, Department of Mechanical Engineering, University of Nottingham, Nottingham, U.K., 1976.
- [5] Munton, R. J., "The Effect of Flow Parameters on Cavitation Erosion," B.S. thesis, Department of Mechanical Engineering, University of Nottingham, Nottingham, U.K., 1977.
- [6] Kleinbreuer, W., "Werkstoffzerstörung durch Kavitation in Ölhydraulischen Systemen," *Industrie-Anzeiger*, Vol. 98, No. 61, 28 July 1976, pp. 1096-1100.
- [7] Pearce, I. D. and Lichtarowicz, A., "Discharge Performance of Long Orifices with Cavitating Flow," *Proceedings*, Second Fluid Power Symposium, Paper D2, British Hydromechanics Research Association, Fluid Engineering, Guildford, U.K., 1971.
- [8] Lichtarowicz, A. and Pearce, I. D., "Cavitation and Aeration Effects in Long Orifices," Conference on Cavitation, The Institution of Mechanical Engineers, London, U.K., 1974.
- [9] Thiruvengadam, A., "Scaling Laws for Cavitation Erosion," Hydronautics Inc. Technical Report 233-15, Laurel, Md., Dec. 1971.
- [10] Knapp, R. T., Daily, J. W., and Hammit, F. G., *Cavitation*, McGraw-Hill, New York, 1970, p. 369.

DISCUSSION

*A. F. Conn*¹ (*written discussion*)—Did you examine the interaction between optimum standoff distance and chamber pressure? We have done some limited elevated ambient pressure tests, in the Cavijet, and found that the optimum standoff decreases with increasing ambient pressure.

A. Lichtarowicz (*author's closure*)—I have done a few tests at higher downstream pressure and I have found, as you have, that the optimum standoff distance decreases as the pressure is increased. For constant upstream pressure the erosion decreases at optimum standoff as the ambient pressure is raised. Some more information on the subject can be found in Ref 6 of the paper.

¹Hydronautics, Inc., Pindell School Road, Laurel, Md. 20810.

Faint, illegible text at the top of the left page, possibly bleed-through from the reverse side.

Faint, illegible text in the lower half of the left page, possibly bleed-through from the reverse side.

Liquid Jet Applications

Faint, illegible text on the right page, possibly bleed-through from the reverse side.

Mechanism of Fracture of Hard Rock Using a Drag Bit Assisted by Waterjets

REFERENCE: Hood, Michael, "Mechanism of Fracture of Hard Rock Using a Drag Bit Assisted by Waterjets," *Erosion: Prevention and Useful Applications*, ASTM STP 664, W. F. Adler, Ed., American Society for Testing and Materials, 1979, pp. 553-561.

ABSTRACT: It is shown that the mechanism of rock fracture is similar both when a blunt drag bit is used to cut strong rock and when a flat-bottomed punch is pressed into the rock surface. In order to study this fracture mechanism an experimental technique was developed which involved indenting the rock specimen in a quasi-static manner, using a drag bit as the punch. The effect of directing waterjets adjacent to the bit was investigated and it was found that these jets caused a rock chip to form with lower than normal forces applied to the bit. This finding agrees with results of previous experiments where lower forces were applied to the bit during the cutting operation when waterjets were used. A hypothesis is proposed to explain the action of the waterjets on the rock to produce this reduction in the indentation force.

KEY WORDS: drag bits, waterjets, hard rock, cutting, indentation, rock fracture, erosion

In recent years considerable attention has been paid to the development of techniques for cutting in hard rock, for application both in the mining and tunneling fields.

This work has concentrated largely on improvements to roller cutter technology, but drag bit cutting tools have been employed successfully in certain applications. For example, drag bits are used both on the Atlas-Copco tunneling machine and on the rock-cutting machines developed by the Chamber of Mines of South Africa [2]. Research work related to this latter project has shown that when a blunt drag bit was used to cut in hard rock, the forces acting on the bit were reduced dramatically when coherent water-

¹Assistant professor, Department of Materials Science and Mineral Engineering, University of California, Berkeley, Calif. 94720; previously, project leader, Mining Technology Laboratory, Chamber of Mines of South Africa.

jets at moderate pressures (50 MPa) were directed immediately ahead of the bit [1]². These reductions in the bit forces were greater than had been expected in the light of existing knowledge that waterjets by themselves, at these moderate pressures, would not cause damage to the rock [3]. An interesting aspect of the influence of waterjets on these reductions in the bit forces was that the force normal to the direction of cutting, known as the bit penetrating force (Fig. 1), was more sensitive to parameters such as the pressure of the waterjets or the point of impingement of the jets relative to the bit than was the force in the direction of cutting, known as the bit cutting force. An explanation of this behavior was sought. This paper discusses the results of an investigation directed toward establishing details of the action of waterjets on the rock adjacent to a drag bit.

Mechanism of Fracture of Strong Rock, Using a Drag Bit with No Waterjets.

In order to understand how waterjets assist a drag bit when cutting in hard rock, it is necessary first to examine the mechanism of rock fracture caused by drag bits without waterjets.

Previous research work [4], has suggested that a drag bit cutting in strong rock acts in a fashion similar to a flat indenter moving through the rock. The results of this work indicated that the rock spalled ahead of the leading face of the bit and that this leading face, therefore, did not affect the rock breaking process.

In order to investigate this proposal, experiments were designed by the author to determine whether the leading face of the bit was ever in contact with the rock during the cutting operation. A series of high-speed films was made of a bit cutting in a block of Witwatersrand quartzite in order to study, in a slow motion, the method of fracture of the rock adjacent to the bit. These films, which were taken at 3000 frames a second using a revolving-prism type camera showed that initial fracture was caused by indentation of the rock by the bit wearflat. A rock chip was formed ahead of the bit and this was observed to rotate while being ejected at a high velocity in the cutting direction.

It was observed also that the cemented tungsten carbide inserts deformed plastically ahead of the leading face of the bit (Fig. 1). If this leading face had functioned as a cutting surface, it would not have been possible for plastic deformation of the tungsten carbide to occur by flowing ahead of the bit. It was concluded, therefore, that the leading face of the bit was not in contact with the rock at any time during the cutting process.

It was concluded from these tests that the mechanism of rock failure during the cutting operation might be similar to that produced by a flat-bottomed indenter pressing into a rock surface. This proposal was in-

²The italic numbers in brackets refer to the list of references appended to this paper.

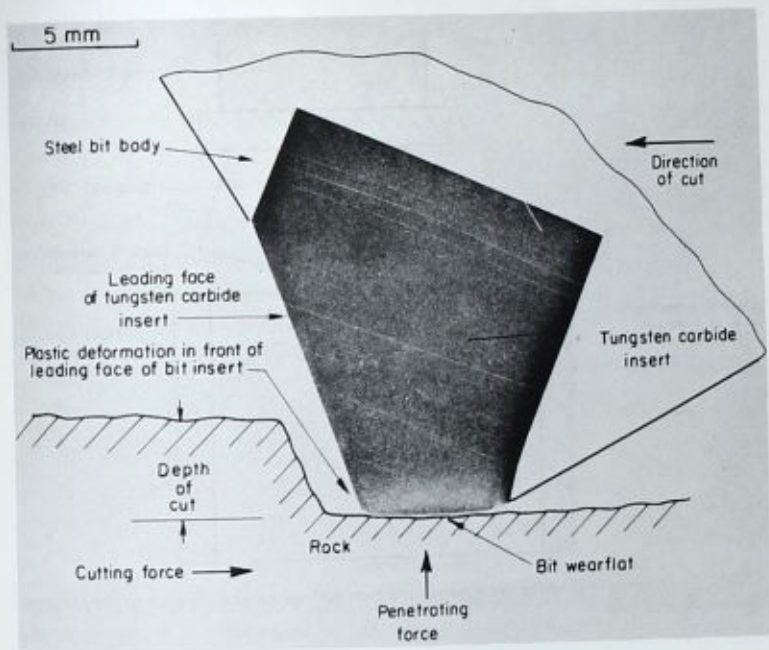


FIG. 1—Magnified section of a cemented tungsten carbide bit insert, showing plastic deformation of the insert ahead of the leading face.

investigated further by conducting experiments to find out whether the rock chip that was formed when a quasi-static indentation force was applied to a rock surface (using a drag bit as the punch) resembled the rock chips that were formed during the cutting operation. It was considered that if rock chips of similar geometry could be produced by these two different methods, then this would be a strong indication that rock fracture during the cutting process could be simulated, in a controlled fashion, by conducting a suite of indentation tests.

A stiff, 2-MN compression testing machine was used for these experiments. A detailed description of this machine has been given in Ref. 5. The bit was placed between the machine loading piston and the cylindrical rock specimen, with the bit wearflat in contact with the rock (Fig. 2). Force was applied to the rock specimen using a fixed rate of displacement of the machine loading piston.

Small rock chips about 2 mm in diameter and 0.5 mm thick were observed to form next to the corners of the bit when the force applied was between 100 and 150 kN. Increasing this load produced a situation where a major rock chip was formed immediately ahead of the leading face of the bit. No damage

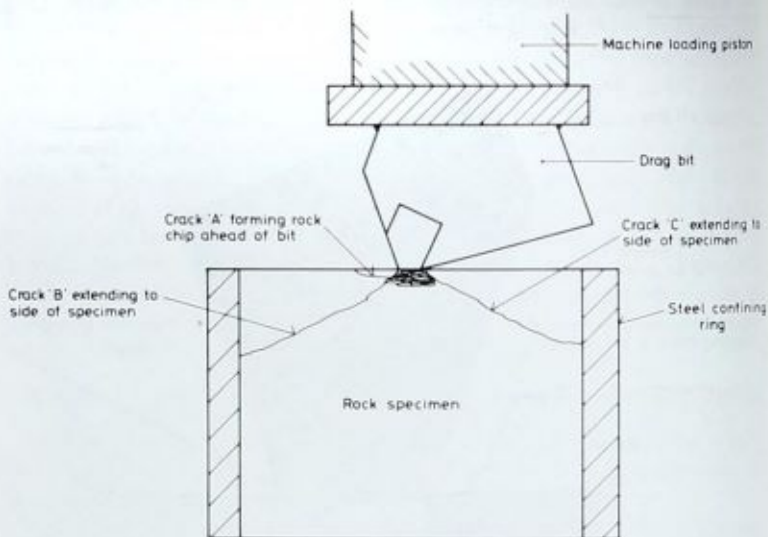


FIG. 2—Diagram illustrating the method used to mount the bit and the rock in the compression testing machine.

to the specimen in the form of cracking, other than the minor chipping in the vicinity of the bit corners, was visible until this major chip was formed. This large chip in front of the bit extended across the full 35-mm thickness of the bit and for some 10 to 15 mm ahead of the bit. The force required to form this rock chip, in both the norite and the quartzite specimens, was between 250 and 350 kN. Examples of curves showing the applied load plotted against bit penetration for a norite specimen is given in Fig. 3.

Rock chips would be expected to form symmetrically on either side of a flat-bottomed rectangular punch which was pressed against a flat rock surface. With all of the specimens tested during this experimental program, however, the large rock chips were formed always on one side of the bit and ahead of the leading face. The reason for this preferential cracking ahead of the bit is found in the asymmetrical bit geometry which permits the steel bit body behind the rear face of the tungsten carbide insert to press against the rock, thereby applying a confining force in this region during the indentation process.

Examination of the rock chips which formed ahead of the bit during these quasi-static indentation tests showed that geometrically they resembled very closely the rock chips that were formed during the cutting process (Fig. 4). It was concluded that rock fracture while cutting was duplicated reasonably well by these indentation tests.

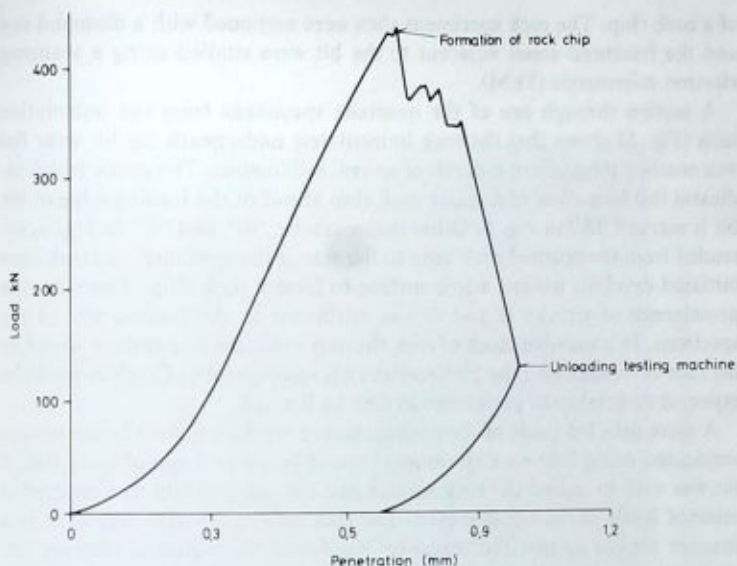


FIG. 3—A typical curve taken from the indentation test series showing the indentation force plotted against the bit penetration.



FIG. 4—Geometric similarity between rock chips formed during the cutting operation and those formed during indentation tests.

Rock Fracture Adjacent to a Blunt Drag Bit

In order to examine the cracks as they were developed in the rock, a further series of tests was carried out where the indentation was stopped at predetermined intervals during the loading operation prior to the formation

of a rock chip. The rock specimens then were sectioned with a diamond saw and the fractured zones adjacent to the bit were studied using a scanning electron microscope (SEM).

A section through one of the quartzite specimens from the indentation tests (Fig. 5) shows that the rock immediately underneath the bit wear flat was crushed intensely to a depth of several millimetres. The crack which indicates the formation of a major rock chip ahead of the leading edge of the bit is marked "A" in Fig. 5. Other major cracks, "B" and "C" in Fig. 5, extended from the crushed rock zone to the side of the specimen. A crack once initiated develops toward a free surface to form a rock chip. Therefore the prominence of Cracks B and C was attributed to the limited size of the specimen. In a massive block of rock the only available free surface would be the face in contact with the bit wearflat and, consequently, Crack A would be expected to develop in preference to Cracks B and C.

A more detailed study of the propagation of cracks adjacent to the bit was conducted using four rock specimens, two of norite and two of quartzite. A bit was used to indent the rock surface and the compression was stopped at selected levels of the applied load. The rock specimens were sectioned in a manner similar to that illustrated in Fig. 5 and the region of interest, immediately underneath the bit wearflat and ahead of the leading face of the bit, was mounted on an SEM specimen holder.

Figure 6 is an SEM micrograph of a section through one of the norite

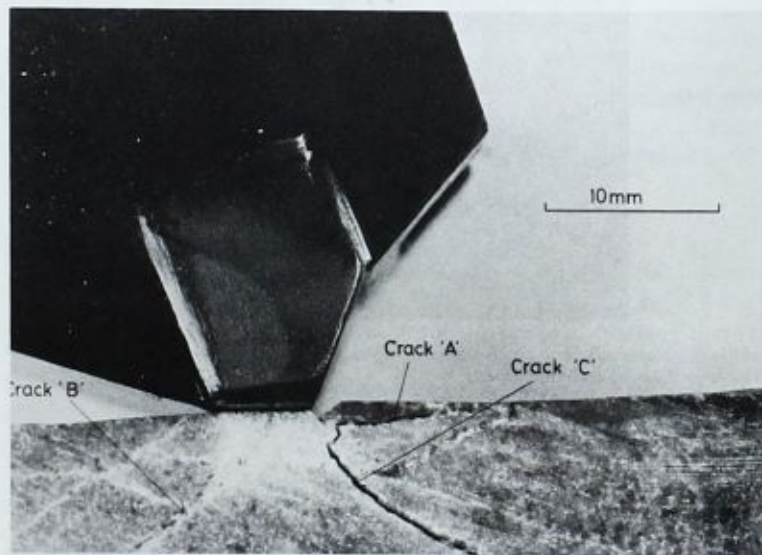


FIG. 5—Section through a rock specimen illustrating the cracks which formed during the indentation tests.

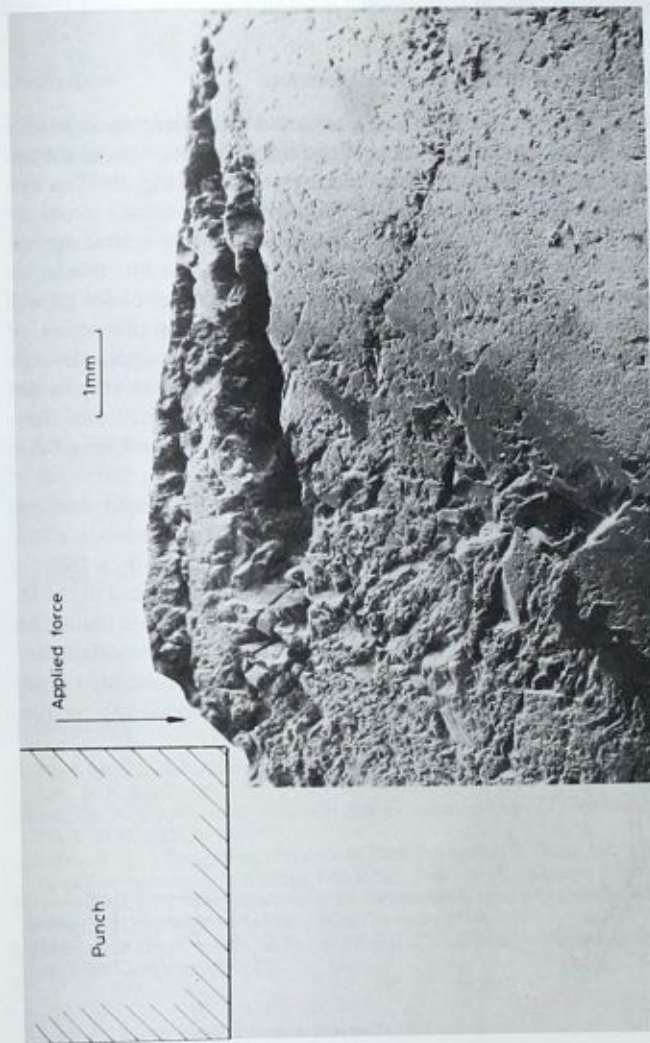


FIG. 6—Micrograph of a section through a norite specimen, illustrating the cracks which developed adjacent to the punch.

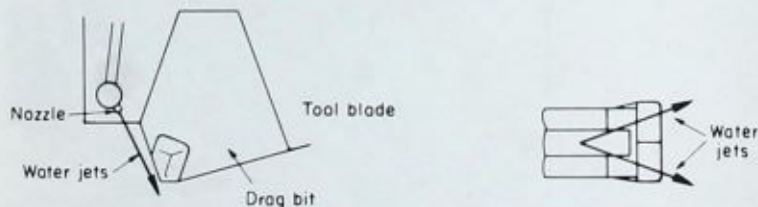
specimens. The most clearly defined fracture in Fig. 6 is that closest to the rock surface. If the force applied to the bit had not been removed but increased, this crack would have extended to form a large rock chip. The geometric similarity between this chip and those from other indentation and cutting experiments (Fig. 4) is apparent.

Indentation Tests Using High-Pressure Waterjets

A series of indentation tests was then conducted with waterjets at 50-MPa pressure directed 2 mm ahead of the leading face of the bit, toward the corners of the cemented tungsten carbide cutting elements (Fig. 7). The tests were performed with both norite and quartzite rock specimens.

The procedure followed was to apply the load slowly to a level approximately half that required to form a rock chip ahead of the bit, that is, between 150 and 200 kN. The stress in the rock at the corners of the bit with this applied force was sufficient to form small rock chips in this region. At this juncture the waterjets were applied at 50-MPa pressure with a flow rate of 0.5 litres/s. When these jets struck the rock surface the rock chip formed ahead of the bit almost immediately. Since the water spray prevented direct observations of the formation of the rock chip, this was sensed by a fall in pressure of the hydraulic fluid in the press.

This experiment was repeated a number of times and the results were consistent in demonstrating that when waterjets were used, the indentation force necessary to form a rock chip ahead of the bit was reduced by a factor of about two. Additional tests, with waterjets directed 10 mm ahead of the bit, showed that the indentation force was not measurably reduced. Limitations of the test equipment made it impractical to carry out more detailed experiments. Nevertheless it is felt that these tests have demonstrated clearly that when suitable waterjets are used to assist the rock breaking operation,



Two jets directed 2mm ahead of the tungsten carbide inserts, inside the corners of the inserts

FIG. 7—Diagram illustrating the position and point of impingement of the waterjets relative to the bit.

the force normal to the rock surface required to form a rock chip ahead of the bit is reduced substantially.

The mechanism for this force reduction appears to be that cracks, initiated ahead of the bit with a relatively low applied force, are propagated when the water is forced into them to form a rock chip.

Conclusions

The investigation of the mechanism of fracture of strong rock using blunt drag bits showed that the bit penetrating force caused the bit to indent the rock and form rock chips ahead of the leading face of the bit. In addition, it was shown that the leading face of the bit is not in contact with the rock during the cutting operation.

A series of indentation tests showed that when 50-MPa waterjets were directed immediately ahead of the bit, the force required to form a rock chip was reduced by a factor of at least two. Previous experiments cutting the rock [1] had shown that the most effective point of impingement of the jets was immediately ahead of the leading face of the bit. It was in this region that cracks were initiated in the rock. Taken together, these experiments indicate that the mechanism by which the waterjets assist the rock breaking process is by the water penetrating and then propagating the cracks which develop ahead of the bit.

Acknowledgments

This work was carried out as part of the research program of South African Chamber of Mines, Mining Technology Laboratory.

References

- [1] Hood, M., *Journal of the South African Institute of Mining and Metallurgy*. Vol. 77, No. 4, Nov. 1976, pp. 79-90.
- [2] Joughin, N. C., *Journal of the South African Institute of Mining and Metallurgy*. Vol. 76, No. 6, 1976, pp. 285-300.
- [3] Labus, T. J., "Energy Requirements of Rock Penetration by Water Jets," Third International Symposium on Jet Cutting Technology, Paper No. E3, Chicago, 1976.
- [4] Riemann, K. P., "Die Zerspanung von Hartgesteinen Beim Schlitzhobeln," Dissertation, Technical University of Hanover, West Germany, 1974.
- [5] Hojem, J. P. M., Cook, N. G. W., and Heins, C., *South African Mechanical Engineer*. Vol. 25, No. 9, 1975, pp. 250-270.

CAVIJET Coal-Cutting Parameters

REFERENCE: Conn, A. F. and Rudy, S. L., "CAVIJET Coal-Cutting Parameters," *Erosion: Prevention and Useful Applications*, ASTM STP 664, W. F. Adler, Ed., American Society for Testing and Materials, 1979, pp. 562-581.

ABSTRACT: Laboratory coal-cutting experiments with CAVIJET cavitating waterjets have demonstrated the feasibility of this technology for hydraulic coal mining applications. The objective of the first phase of a developmental program, as described in this paper, was to determine the system and operating parameters required to cut coal with CAVIJETS, and to compare the results with those observed for noncavitating jets.

Comparable coal cutting was achieved with the CAVIJET, relative to high-pressure, noncavitating jets, using one-fifth the pressure and one-half the specific energy. These results suggest that CAVIJET-augmented mining devices can be developed with compact, low-pressure pumps. Thus, CAVIJET should be capable of operating with safer, lighter, more suitable support equipment, while providing all of the advantages (reduction of dust and sparks; decreased damage to cutters) of conventional hydraulic mining methods.

KEY WORDS: CAVIJET, cavitation, waterjets, coal, hydraulic mining, erosion

There is growing interest in the use of waterjets for mining, drilling, and cutting applications because of the high levels of deliverable power, the potential for reducing tool damage, the elimination of spark creation which might ignite gas deposits, and considerable reduction in dust levels [1].² Most of the hydraulic mining has been done either with low-pressure, very-high-flow sluicing jets, high-pressure waterjets [68.9 to 689.0 MPa (10 000 to 100 000 psi)], or with pulsating waterjets in which there is an intermittent ejection of slugs of water [2]. In contrast to these jets a unique, cavitating waterjet called the CAVIJET³ is now being developed. This device is one of the very few successful techniques in which the destructive power of cavitation is harnessed to do useful work. The basic difference between a cavitating waterjet and a high-pressure steady or pulsating waterjet is that the damage

¹Principal research scientist and head, and associate research scientist, respectively, Material Sciences Division, Hydronautics, Inc., Laurel, Md. 20810.

²The italic numbers in brackets refer to the list of references appended to this paper.

³CAVIJET is a trademark of Hydronautics, Incorporated, Laurel, Md.

in the former case is amplified by the collapse of cavitation bubbles and is not merely due to the high pressure or velocity of the jet. The CAVIJET method has been successfully demonstrated for various cutting, cleaning, and drilling applications [3].

The experiments reported herein were undertaken in order to investigate the feasibility and energy effectiveness of using the CAVIJET method for cutting coal. The ultimate objective of this investigation is the design, fabrication, testing, and evaluation of prototype equipment capable of use in the field to cut coal by the CAVIJET method. Under the first-phase contract a laboratory experimental program was defined to provide controlled test conditions, so that feasibility may be established and values determined of the parameters required for CAVIJET coal-cutting devices.

The CAVIJET method and the Hydronautics CAVIJET test facility are described in the next section. The acquisition and preparation of test specimens are then outlined, followed by a summary of the experimental procedures and parameters. Some typical test results are presented, and the performance of CAVIJET is compared with noncavitating waterjets for coal-cutting applications.

The CAVIJET Cavitating Waterjet Method

CAVIJET is a turbulent waterjet in which vapor and gas cavities are stimulated to grow in order to enhance the destructive power of a relatively low-velocity steady jet. By proper adjustment of the distance between the nozzle and the surface to be fragmented, these cavities are permitted to grow from the point of formation and then to collapse on that surface in the high-pressure stagnation region where the jet impacts the solid material. Because the collapse energy is concentrated over many very small areas at collapse, extremely high, very localized stresses are produced. This local amplification of pressure provides the cavitating waterjet with a great advantage over steady noncavitating jets, which are operated at the same pump pressure and flow rate. Further details about the basic principles for the operation of a cavitating waterjet may be found in Ref 4.

The CAVIJET Test Facility

The primary components to this facility (see Fig. 1a) include a pump, reservoirs to recover and store the water, suitable filters, controls, pressure and temperature gages, flow measuring devices for precisely measuring all system parameters, and a new large test chamber with the means for translation of the CAVIJET nozzle relative to test specimens either in air or in a submerged configuration. During this program, because of the large coal specimens which were to be used, it was decided to design and build a new test chamber. The overall dimensions of this test chamber (Fig. 2) are length

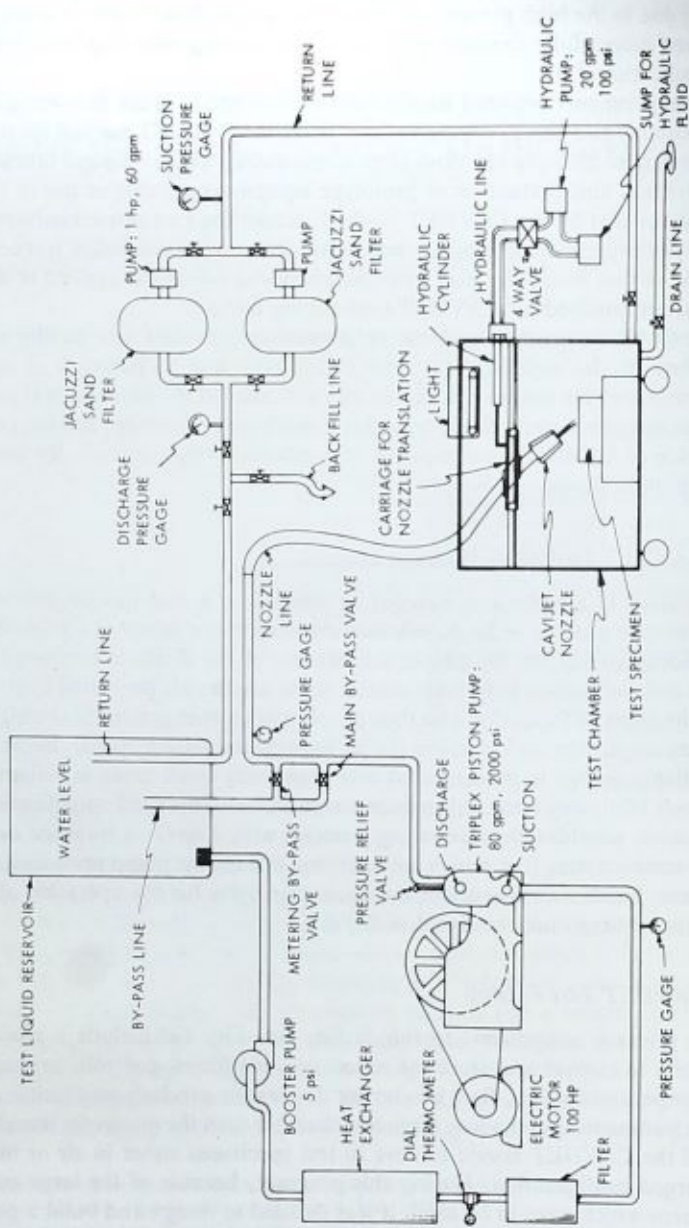


FIG. 1. Schematic of CAVIJET cavitation waterjet test facility.

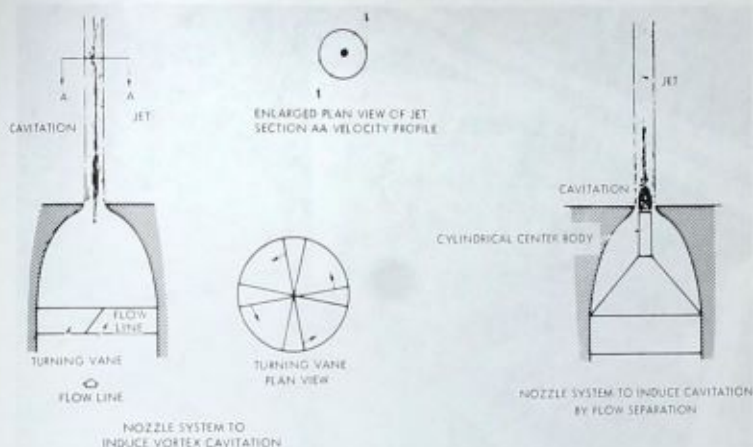


FIG. 1b—Typical cavitating waterjet nozzle configurations.

1.8 m (6 ft), width 1.5 m (5 ft), and height 1.8 m (6 ft) from the floor of the chamber to the ceiling of the roll-away cover. The height of the lower, water-containing section of the test chamber is 1.2 m (4 ft). Further details about this facility are given in Ref 5. Some typical CAVIJET nozzle configurations are shown in Fig. 1b.

Acquisition and Preparation of Test Specimens

Coal segments were acquired from the Fire Creek Coal Seam near Anjean, W. Va. The medium-hard, low-sulfur bituminous coal seam in this location lies below an overburden of sand stone which is about 9.1 to 10.7 m (29.8 to 35.1 ft) thick. The seam has an average thickness of 1.5 m (4.9 ft).

The test specimen developed for these tests consisted of as many as nine coal segments, each roughly a cube about 0.3 m (0.98 ft) on a side. The coal segments were imbedded in concrete, to provide an overall testing area of about 0.7 m² (7.5 ft²), as seen in Figs. 2 and 3. A steel "girdle" was fabricated to surround the coal-and-concrete specimen to provide compressive loading, and hence some simulation of the actual overburden loading on the coal seam. Thus, any given test run involved cutting across several pieces of coal. The concrete block with imbedded coal specimens was 0.76 by 0.91 m (2.49 by 2.98 ft) by at least 0.25 m (0.82 ft) deep and weighed about 3.5 to 4.0 kN (800 to 900 lb).

Experimental Procedure and Parameters

After the concrete block, containing several coal specimens, was placed in

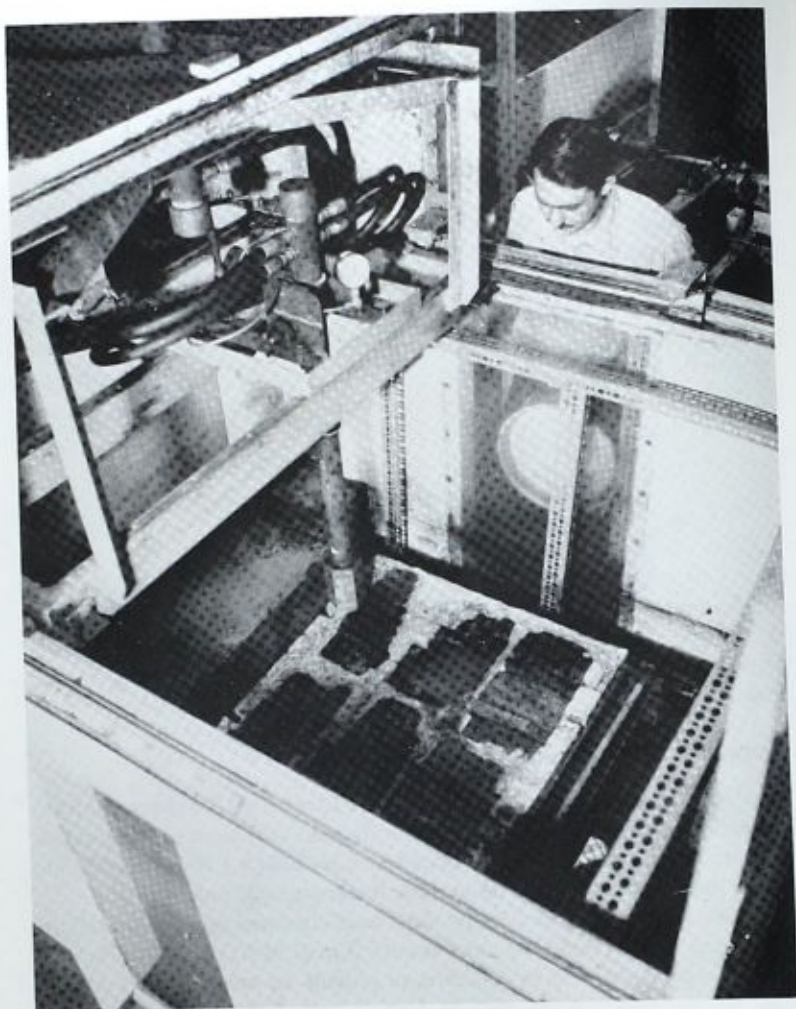
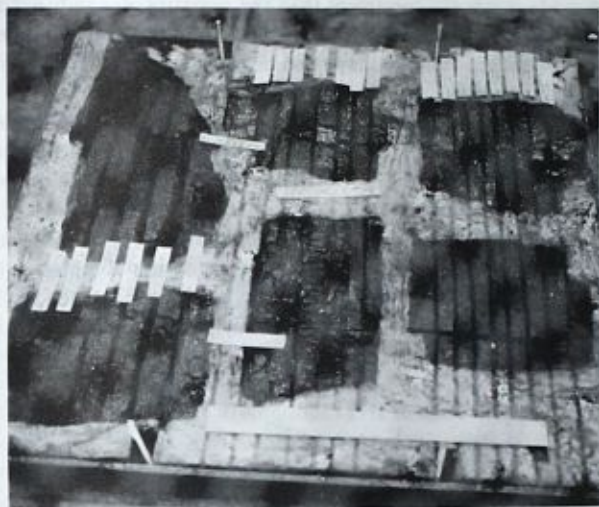
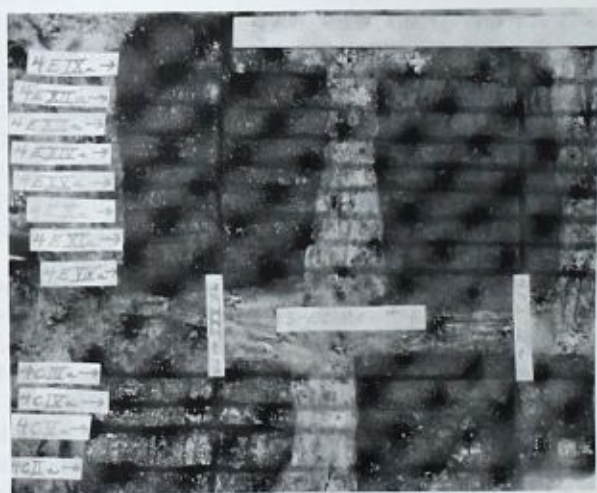


FIG. 2—Test chamber of CAVIJET cavitating waterjet facility.

the test chamber, it was properly oriented so that the bedding planes were either parallel or perpendicular to the direction of translation of the CAVIJET. To begin each test, the chamber cover was closed and, with no pressure at the nozzle, trial runs were made to set the desired translation velocity. Once these settings were established for the hydraulic system, the required nozzle pressure was set by adjusting the amount of bypass flow. A single pass



(a) Overall View



(b) Close-up: Upper right-hand corner

FIG. 3—Specimen 4; tests with 3.2-mm ($1/8$ in.) and 6.4-mm ($1/4$ in.) CAVIJET.

was then made across the specimen; then the pressure was reduced and the cover opened so that measurements of the slots cut in the coal could be made. Sketches were also made of the shape and position of each coal segment, and the location and configuration of each slot.

For each test run the following system parameters were noted: nozzle size, nozzle type, number of nozzles, and relative placement of multiple nozzles; as well as operating parameters: translation velocity, v ; angle of impingement, θ ; nozzle pressure, p ; flow rate, Q ; standoff distance, that is, the distance between the nozzle face and the coal surface, l ; and the mode of operation, which was in-air for all of these tests. At the completion of each test run the slot depth, Z , and the slot width, W , were measured.

From these dependent and independent variables, the following performance parameters were determined:

$$\begin{aligned} \text{Rate of area cutting, } \dot{A} &= Z \cdot v \\ \text{Rate of volume removal, } \dot{V} &= Z \cdot W \cdot v \end{aligned}$$

$$\begin{aligned} \text{Kerfing effectiveness, } e_a &= \dot{A}/P \\ \text{Volume removal effectiveness, } e_v &= \dot{V}/P \end{aligned}$$

where P is hydraulic power, and e_a and e_v are the measures of area of slot created per unit energy and volume of coal removal per unit energy, respectively.

As is evident from Fig. 3*a,b*, the slots were very clearly defined in almost all the tests, thereby making it quite easy to measure the widths and depths. Several measurements along the length of the slot were made to establish a "typical" or "modal" value, and this value is used for analyses in the next section. Maximum and minimum were also recorded. The slot depths were measured to within ± 6.4 mm ($1/4$ in.), and the widths to within ± 3.2 mm ($1/8$ in.). The translation velocity was measured over a predetermined distance of 0.616 m (24.25 in.). Microswitches at two positions started and stopped an electric timer, measuring the time of travel to within ± 0.02 s.

Although no attempt was made to control the moisture content of most of the coal segments used in this study, a few tests were run to assess the importance of this parameter. A batch of coal blocks was removed from the mine, kept continuously moist by completely covering them in wet newspapers, and encased into the concrete specimen format within 48 h after being mined. Testing was done after the concrete block was cured for two days under several inches of water in the mold. The experimental data showed that the widths and depths for these tests were well within the scatter for comparable tests without any moisture control.

Test Results

In this section a summary of the experimental results for coal cutting with

single and dual CAVIJET nozzles is presented. Three nozzle orifice diameters were utilized, namely, 2.2, 3.2, and 6.4 mm (0.086, $\frac{1}{8}$, and $\frac{1}{4}$ in.), and for each, the centerbody CAVIJET configuration was utilized (see Fig. 1b). The centerbody was cylindrical in shape, flat ended, and had a diameter one half of the nozzle orifice diameter in each case. The measurements were made over a translation velocity range of 5 cm/s (12.7 in./s) to about 100 cm/s (254 in./s). Three nozzle pressures were utilized in the tests, namely, 10.3, 13.2, and 14.8 MPa (1500, 1910, and 2150 psi).

The standoff distance was varied from 1.3 to 6.4 cm (0.5 to 2.5 in.) for the 3.2-mm ($\frac{1}{8}$ in.) CAVIJET, and from 1.3 to 12.7 cm (0.5 to 5 in.) for the 6.4-mm ($\frac{1}{4}$ in.) CAVIJET. Over these ranges of standoff, the slot dimensions were constant to within measurable accuracy. Thus, all subsequent tests were run at a standoff of 3.8 cm (1.5 in.) for the 3.2-mm ($\frac{1}{8}$ in.) nozzle, and 10.8 cm (4.25 in.) for the 6.4-mm ($\frac{1}{4}$ in.) nozzle. The angle of impingement parameter was varied from 0 deg (perpendicular to the surface of the coal) to 30 deg, in increments of 10 deg. These tests were run with the 3.2-mm ($\frac{1}{8}$ in.) nozzle, and over this range no measurable differences (see tolerances given in the foregoing) were detected. Thus, all subsequent tests were run at normal incidence to the surface of the coal.

Data Reduction

Before deriving the various performance parameters, it was first necessary to define the variation of slot depth, Z , and slot width, W , with respect to nozzle size, d , nozzle pressure, p , and translation velocity, v . In order to reduce the uncertainty due to the inherent variations in the coal properties and the randomness associated with the statistical processes that cause cavitation erosion, kinematic scaling concepts were used to process the raw data for Z . The raw data were plotted for different nozzle sizes, but at the same pressure, by introducing the variables: nondimensional slot depth, $\bar{Z} = Z/d$, and nondimensional translation velocity, $\bar{v} = v\tau/d$, where τ is the "intrinsic erosion time" for coal, which is assumed to be constant. Thus a large set of data points was used to estimate the average slot depth as a function of translation velocity. A typical nondimensional plot of \bar{Z} versus \bar{v} is presented in Fig. 4. Since the intrinsic erosion time τ is taken to be constant for a particular material, it was arbitrarily set at one second for these analyses. The solid curve in Fig. 4 was faired through the average values of all the data points at each nondimensional velocity. Thus, by this method of pooling the data, the uncertainty in determining the mean value of the slot depth at each translation velocity was reduced. The dependence of mean slot depth, Z , on the jet translation velocity, v , for each nozzle size was then obtained from these nondimensional curves by multiplying each \bar{Z} and \bar{v} by the respective nozzle diameter, d . A typical set of curves derived by this procedure is shown in Fig. 5.

It should be noted that over the range of translation velocities covered in

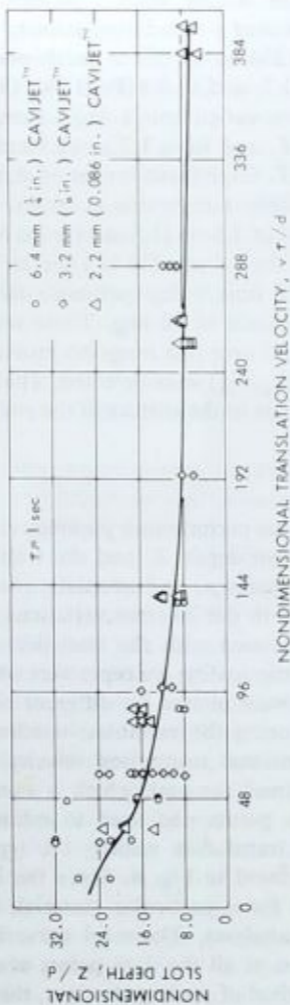


FIG. 4—Nondimensionalized CAVIJET performance at 13.2 MPa (1910 psi).

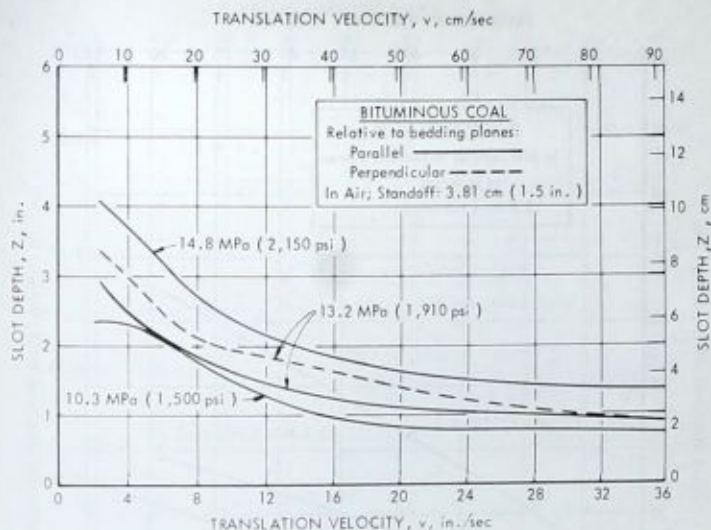


FIG. 5—Effect of pressure on slot depth; 3.2-mm ($1/8$ in.) CAVIJET.

these tests the slot widths were found to be essentially constant. Moreover, the slot width was the same when cutting was done either parallel or perpendicular to the bedding planes. The width of the slot for the 3.2-mm ($1/8$ in.) jet at 14.8 MPa (2150 psi) was 8.9 mm (0.35 in.), slightly bigger than the 7.9-mm (0.316 in.) width at 13.2 MPa (1910 psi). The width was 16 mm (0.64 in.) for the 6.4-mm ($1/4$ in.) jet at 13.2 MPa (1910 psi). Hence, in all the derivations of performance parameters, the slot width was a fixed value over the entire velocity range for each test pressure and nozzle size.

Performance Parameters

Typical curves showing the effects of pressure, nozzle size, and translation velocity on volume removal rate are given in Figs. 6 and 7. Results for each nozzle size, showing the effects of the operating parameters on \dot{V} and \dot{A} , were obtained [5]. A compilation of some results for volume removal effectiveness, e_v (or specific energy, E_v , which is the inverse of e_v), is shown in Fig. 8. These data indicate that larger nozzles provide larger e_v 's, but an inverse dependence on pressure is observed at velocities below 65 cm/s (25 in./s). A similar pressure effect was seen for the kerfing effectiveness, e_k ; that is, lower pressures correlate with higher e_k 's. However, smaller nozzles were observed to allow higher e_k values (see also Fig. 11).

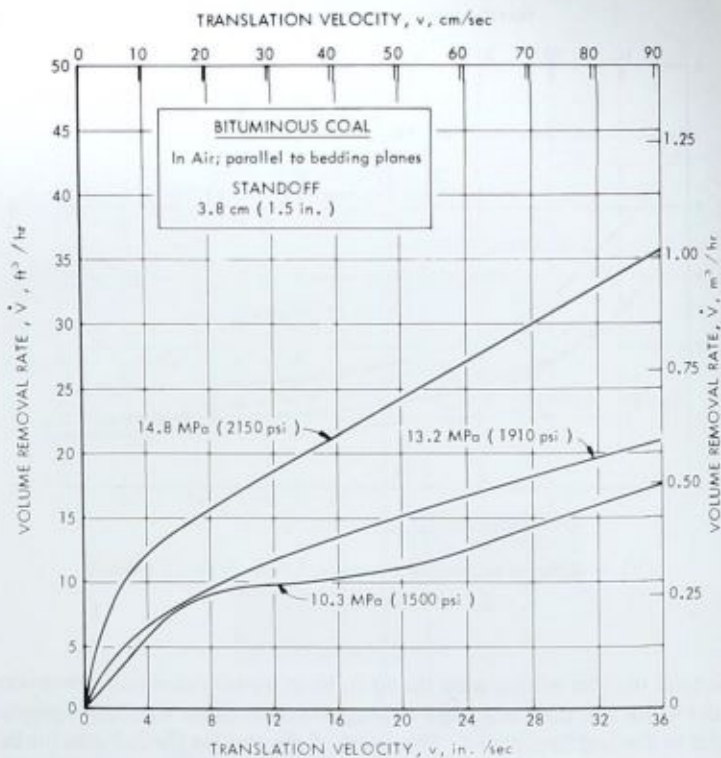


FIG. 6—Effect of pressure on volume removal rate for 3.2-mm ($1/8$ in.) CAVIJET.

Testing with Dual Nozzles

Tests were also conducted with two 3.2-mm ($1/8$ in.) CAVIJET nozzles "side-by-side," and with one jet following immediately after the other along the same slot. The center-to-center distance between the two jets was varied from 3.18 to 3.81 cm (1.25 to 1.50 in.). Based upon the results of more than 40 tests [4] in the side-by-side operation, there exists a strong possibility for consistent removal of the lands between the kerfs, particularly if one or both of the jets are suitably angled inward to provide a cutting action and removal force on the base of the land.

The optimum orientation of two side-by-side 3.2-mm CAVIJETS, at suitable angles and center-to-center spacings, might be expected to produce volume removal rates of 2.8 to 5.7 m³/h (100 to 200 ft³/h). Using a density for the Fire Creek coal of 12.9 kN/m³ (82 lb/ft³), this extrapolates to a cut-

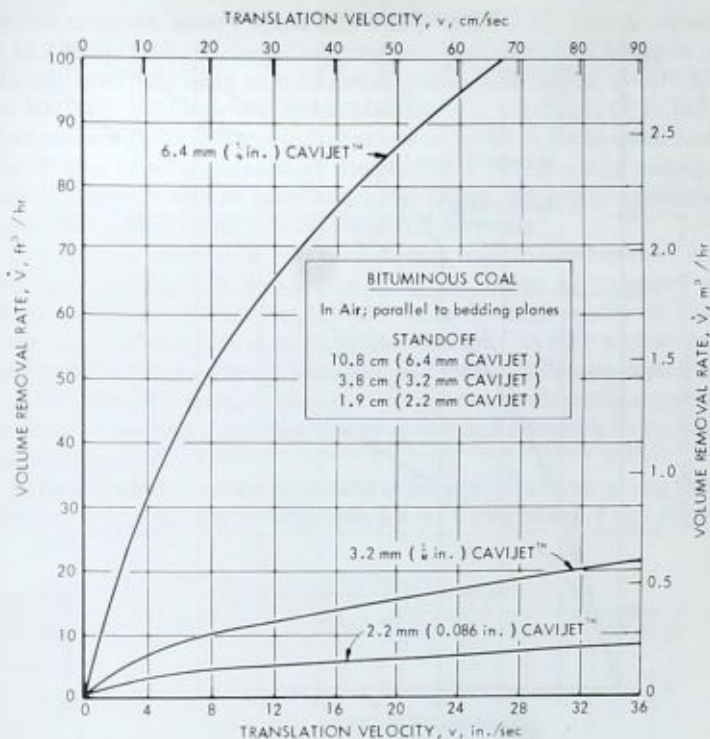


FIG. 7—Effect of nozzle size on volume removal rate at 13.2 MPa (1910 psi).

ting rate of 0.6 to 1.2 kN/min (0.07 to 0.13 tons/min), and energy requirements of 0.33 to 0.67 kWh/kN (3 to 6 kWh/ton).

To compare the performance of dual-nozzle cutting with the analogous cutting by a *nonsimultaneous* jet, the results of cutting parallel slots with a single jet, when the land width between the fresh slot and the previous slot was smaller than 3.18 cm, were studied. It was found that the blowout for the land, for side-by-side cutting by a single jet, occurred about 35 percent of the time. This should be compared with the results for simultaneous dual-CAVIJET tests, where blowouts occurred 49 percent of the time over the full velocity range, and even more frequently for lower velocities [6 cm/s (2.36 in./s)]. Thus, these results suggest that there may be an advantage to using dual simultaneous jets for optimizing coal removal rates. These dual-nozzle tests were not extensive, and further tests, preferably on *in situ* coal, should be performed before final conclusions can be drawn.

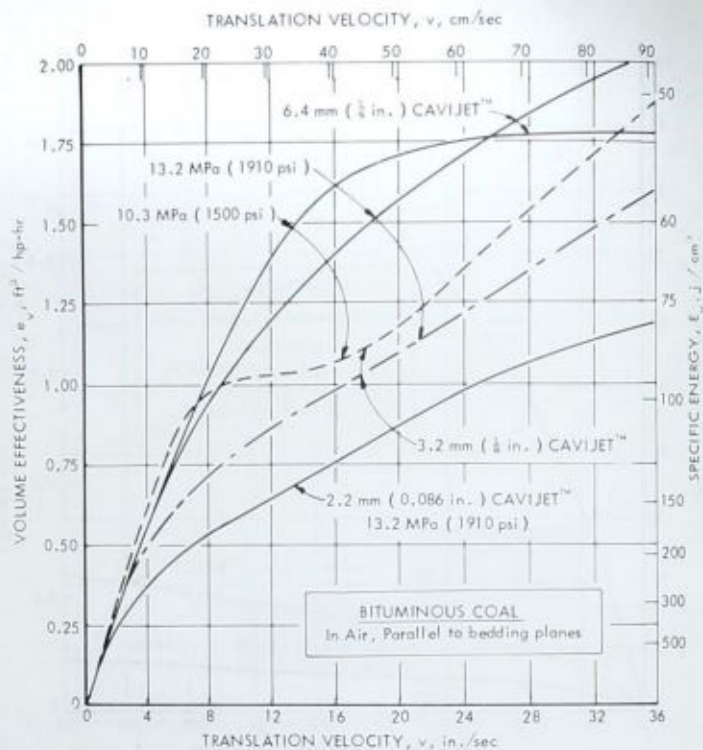


FIG. 8—Comparisons of volume removal effectiveness: 2.2-mm (0.086 in.), 3.2-mm (1/8 in.), and 6.4-mm (1/4 in.) CAVIJETS.

In contrast to these simultaneous dual-nozzle, side-by-side tests, the results from simultaneous testing of two 3.2-mm (1/8 in.) CAVIJETS, operated so that one jet followed the other at a distance of 3.18 cm (1.25 in.), do not indicate any advantage over tests with a single jet when the second pass is made at a later time by the same nozzle along the same slot.

Evaluations of Test Results

Coal Cutting Comparisons

In this section the results of the coal-cutting tests with the CAVIJET method, as summarized in the previous section, are compared with similar tests conducted with noncavitating jets. The noncavitating jet data are from two sources: (1) tests run in the HYDRONAUTICS laboratory during the

present program, using a nozzle with a 1.78-mm (0.070 in.) orifice diameter at 12.2 MPa (1910 psi), and (2) a recent coal-cutting study by Summers and Mazurkiewicz [6], using an 0.80-mm-diameter (0.035 in.) jet at 68.9 MPa (10 000 psi). Although the nozzle geometry was not described in Ref 6, discussions with the authors indicated it was similar to the so-called Leach and Walker [7] configuration we used for the 1.78-mm nozzle, namely, a conical transition with an included angle of 14 deg, followed by a cylindrical exit section with a length equal to 2.6 orifice diameters.

It should be emphasized that the following comparisons between CAVIJET coal cutting and the noncavitating jet studies by Summers and Mazurkiewicz are not on identical coal under identical conditions. These comparisons are made in order to indicate that the CAVIJET method shows the capability, at much lower pressures, of creating similar slot depths, and with lower specific energies. However, any more exact comparisons can only be obtained for tests in the same pieces of coal, and preferably under actual mining conditions.

In Figs. 9 and 10 we have plotted slot depth and rate of area cutting versus translation velocity, respectively, both for the CAVIJETS [6.4 and 3.2 mm

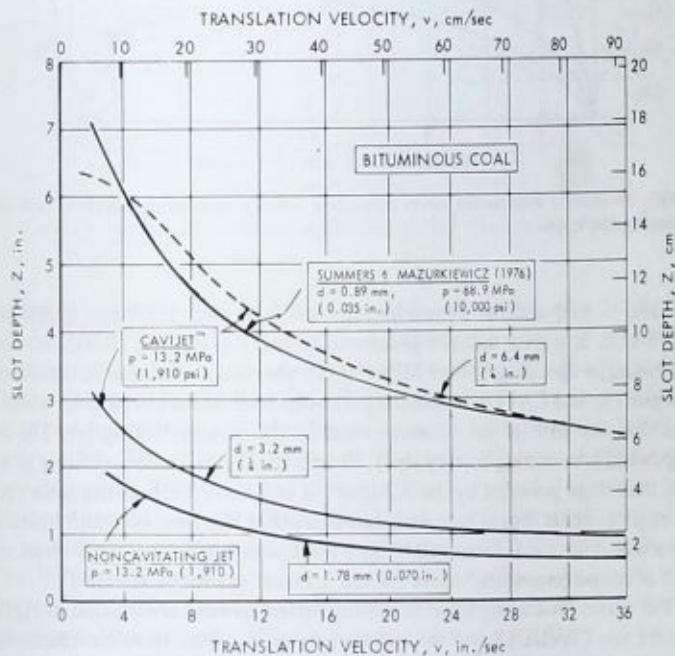


FIG. 9—Slot depth versus translation velocity, comparing CAVIJET with noncavitating jets (in air).

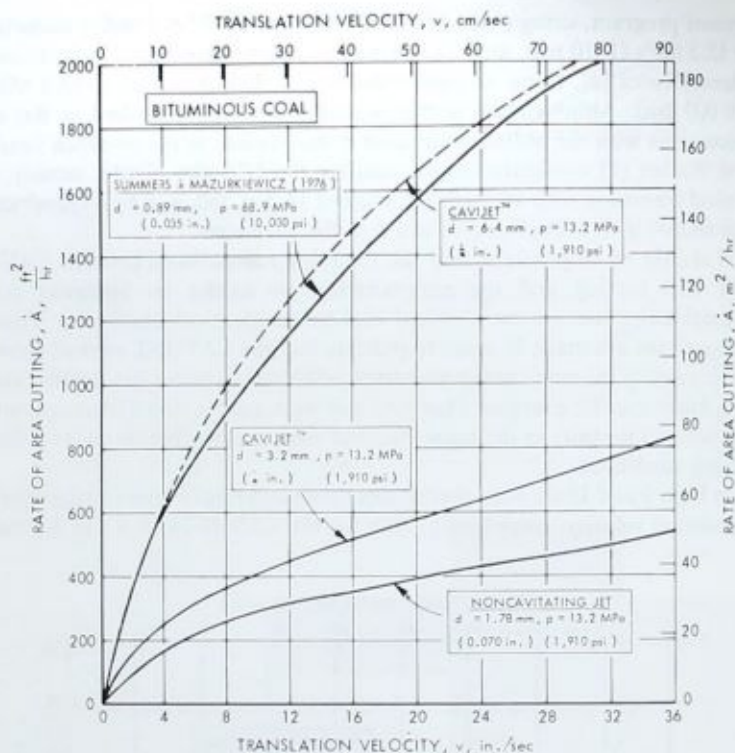


FIG. 10—Rate of area cutting versus translation velocity, comparing CAVIJET with noncavitating jets (in air).

($1/4$ and $1/8$ in.)] and the noncavitating jets [0.89 and 1.78 mm (0.035 and 0.071 in.)]. It is seen that the performance of an 0.89-mm (0.035 in.) noncavitating jet operating at 68.9 MPa (10 000 psi) is comparable to that for the 6.4-mm ($1/4$ in.) CAVIJET operating at only 13.2 MPa (1910 psi), which is less than one fifth of the pressure used in the noncavitating jet. The slot depth and area cutting rate by the 1.78-mm (0.071 in.) noncavitating jet are less than those provided by the 3.2-mm ($1/8$ in.) CAVIJET at the same operating pressure. It should be noted, however, that the flow rate and hydraulic horsepower for the 1.78-mm (0.07 in.) noncavitating jet are only about one half of the corresponding values for the 3.2-mm ($1/8$ in.) CAVIJET.

The curves for kerfing (or area cutting) effectiveness are plotted in Fig. 11 for the two CAVIJETS and the two noncavitating jets. Here we observe the trend mentioned earlier of smaller-diameter jets providing more area cutting effectiveness. The slot width is not a factor in deriving this particular

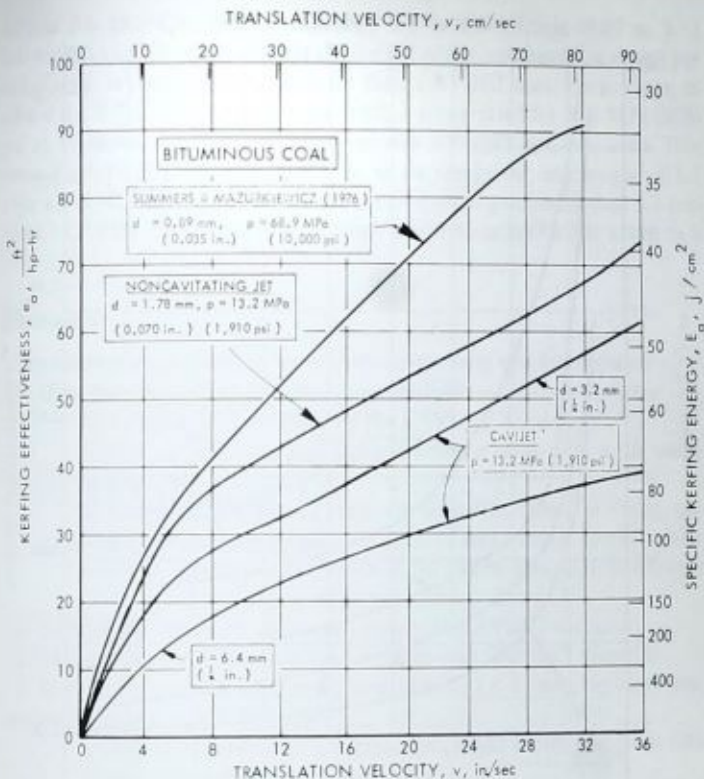


FIG. 11—Area cutting effectiveness, comparing CAVIJET with noncavitating jets (in air).

parameter. However, because the slot width was only about 3.5 times the 0.89-mm (0.035 in.) noncavitating nozzle diameter, or about 3.1 mm (0.12 in.) wide, this width was too narrow for subsequent mechanical fracturing. Thus, a dual nozzle was developed [6] which, of course, requires twice the power and hence halves the kerfing effectiveness for this noncavitating jet configuration. The slot width for the 1.78-mm (0.071 in.) noncavitating jet was 4.83 mm (0.19 in.), or 2.7 times the nozzle diameter. As cited earlier, this factor is about 2.5 for the CAVIJET nozzles. The curves plotted in Fig. 12 compare the specific energies (or volume removal effectiveness) for the CAVIJETS and the noncavitating jets. It is seen, over this range of velocities, that the CAVIJET is more than twice as effective in volume removal, despite operation at less than one-fifth the pressure used for the 0.89-mm (0.035 in.) noncavitating water jet. The 1.78-mm (0.071 in.) noncavitating jet at 13.2 MPa (1910 psi) produces a more effective volume removal as compared with

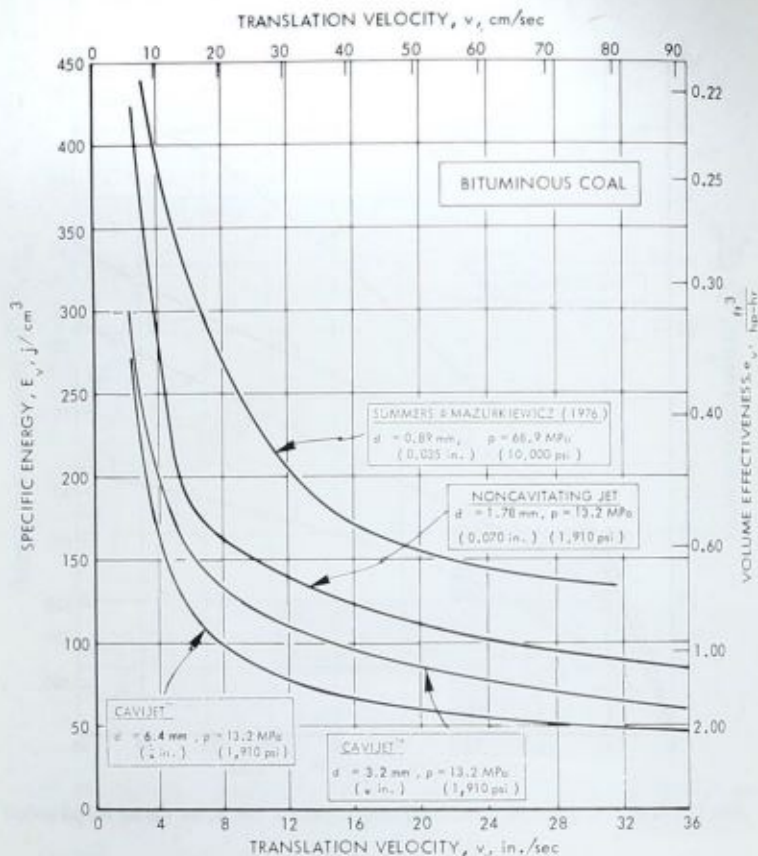


FIG. 12—Specific energies for coal cutting, comparing CAVIJET with noncavitating jets (in air).

an 0.89-mm (0.035 in.) jet operating at 68.9 MPa (10 000 psi). These trends seem to be consistent with earlier coal-cutting work by Summers and Peters [8].

Coal Removal Comparisons

In a review paper on hydraulic mining, Frank [9] summarized a variety of coal mining projects using noncavitating waterjets, at pressures up to 34.5 MPa (5000 psi). The removal rates in these tests ranged from 0.9 to 7.7 kN/min (0.10 to 0.87 tons/min). Although these removal rates are somewhat higher than those mentioned earlier for the slot-plus-land removal by two

3.2-mm ($1/8$ in.) CAVIJETS, namely, 0.6 to 1.2 kN/min (0.07 to 0.13 ton/min), it should be noted that the overall power, and hence the energy per unit of coal, is considerably lower for these CAVIJET tests. For instance, to achieve the 7.7-kN/min (0.87 tons/min), a pump rated for 34.5 MPa (5000 psi) at 19 litres/ s^{-1} (300 gal/min), or 625 kW (875 hp), was used. This removal rate was therefore produced at an energy per unit weight of 1.5 kWh/kN (13.3 kWh/ton) whereas the corresponding values for dual 3.2-mm ($1/8$ in.) CAVIJETS are 24 kW (32 hp) and 0.33 to 0.67 kWh/kN (3 to 6 kWh/ton).

Conclusions

The following conclusions have been drawn from this investigation:

1. Over the translation velocity range studied:
 - Slot depths are scalable by the CAVIJET diameter,
 - Effects of standoff are negligible in the range of 4 to 20 nozzle diameters.
 - Effects of impingement angle are negligible, from 0 to 30 deg, and
 - The performance parameters (rate of area cutting, rate of volume removal, kerfing effectiveness, and volume removal effectiveness) all improve with increasing translation velocity.
 2. Kerfing effectiveness varies inversely with CAVIJET diameter.
 3. Volume removal effectiveness increases with CAVIJET diameter.
 4. In comparison with laboratory tests of small (< 1 mm), high-pressure, noncavitating jets, the CAVIJET:
 - Cut slots of comparable depths, with larger widths, using one fifth of the pressure,
 - Has smaller kerfing effectiveness, and
 - Has larger volume removal effectiveness.
 5. In comparison with coal mining tests with large [up to 9.5 mm (0.38 in.)], high-pressure, noncavitating jets, the dual-CAVIJET laboratory tests:
 - Produced comparable coal-removal rates with much lower pressure and input power, and
 - Required about one-half the energy per unit weight of coal cut.
- These conclusions suggest that a CAVIJET-augmented coal-cutting device will be able to operate in a coal mine, with lighter and safer hardware, and still produce effective cutting rates with the same advantages of conventional hydraulic mining machines currently in use. In addition, utilization of lower system pressures should yield an increase in pumping-hardware life and reliability, and allow for a reduction of the energy consumption required to reach any given coal mining objective.

Acknowledgments

The authors are grateful to W. H. Engelmann and Hamilton Reese of the

U. S. Bureau of Mines for their encouragement and cooperation. We also thank Dr. T. R. Sundaram of HYDRONAUTICS, Incorporated for his many valuable suggestions during the course of this work; Dr. G. D. Mehta for assistance in the data reduction; and G. S. Frederick for his careful and dedicated efforts in creating and demolishing those test specimens.

The contents of this paper are based on a research project at HYDRONAUTICS, Incorporated, Laurel, Maryland, sponsored by the U. S. Bureau of Mines, Advanced Coal Mining Technology Program, under USBM Contract No. H0252025, with W. H. Engelmann, Twin Cities Mining Research Center, as the technical project officer.

References

- [1] Lohn, P. D. and Frank, J. N., "Airborne Respirable Dust Generated During Cutting of Coal with Water Jets," Twin Cities Mining Research Center, USBM RI 8014, U. S. Bureau of Mines, 1975.
- [2] *Proceedings*, Third International Symposium on Jet Cutting Technology, British Hydromechanics Research Association, Fluid Engineering, Chicago, Ill., May 1976.
- [3] Conn, A. F., Mehta, G. D., and Sundaram, T. R., "Cavitating Water Jets I. Review and Applications," ASME Cavitation and Polyphase Flow Forum, American Society of Mechanical Engineers, March 1976, pp. 12-15.
- [4] Mehta, G. D., Sundaram, T. R. and Conn, A. F., "Cavitating Water Jets II. Basic Principles of Operation," ASME Cavitation and Polyphase Flow Forum, American Society of Mechanical Engineers, March 1976, pp. 16-17.
- [5] Conn, A. F. and Rudy, S. Lee, "Parametric Study of Coal Cutting with the CAVIJET™ Cavitating Water Jet Method," Hydronautics, Incorporated Technical Report 7511-1, Laurel, Md., Sept. 1976.
- [6] Summers, D. A. and Mazurkiewicz, M., "The Effect of Jet Traverse Velocity on the Cutting of Coal and Jet Structure," *Proceedings*, Third International Symposium on Jet Cutting Technology, Paper D5, British Hydromechanics Research Association, Fluid Engineering, Chicago, Ill., May 1976.
- [7] Leach, S. J. and Walker, G. L., *Philosophical Transactions of the Royal Society*, London, Vol. 260, 1966, pp. 295-308.
- [8] Summers, D. A. and Peters, J. F., "Preliminary Experimentation on Coal Cutting in the Pressure Range 35 to 200 MN/m²," *Proceedings*, Second International Symposium on Jet Cutting Technology, Paper H2, British Hydromechanics Research Association, Fluid Engineering, Cambridge, England, April 1974.
- [9] Frank, J. N. in *Proceedings*, 34th Annual Mining Symposium, Annual Meeting of the American Institute of Mining Engineers and the University of Minnesota, Duluth, Minn. Jan. 1973, pp. 129-142.
- [10] Busch, J. W., "Hydraulic Mining of Anthracite: Engineering Development Studies," BuMines Report of Investigation 6610, U. S. Bureau of Mines, 1964.

DISCUSSION

*D. A. Summers*¹ (*written discussion*)—One of the controversial problems which crops up with the use of cavitating jets is the comparison of like with like. This is, I am afraid, true again here since in the comparison of Dr. Conn's results with those we got at University of Missouri-Rolla, we are not comparing equivalent items. In a paper we gave in 1974 [8] we indicated the benefits of increasing nozzle diameter as opposed to increasing jet pressure for obtaining more effective cutting at higher horsepower. (To put it crudely, if you double the jet energy by increasing pressure, you approximately double the material removed; if you double the energy by increasing the diameter, you quadruple the material removed). However, under the constraints of a system to fit into an existing underground operation with perhaps water-sensitive material in the vicinity, we imposed an upper limit of 3 litres/s⁻¹ (50 gal/min) through the system or perhaps 0.31 litres/s⁻¹ (5 gal/min) per orifice. Thus, while a comparison with our data can be made, it should be understood that at lower pressures and higher flow rates such as those used by Dr. Conn, the specific energy of jet cutting without cavitation would be at equivalent or possibly lower levels.

A. F. Conn and S. L. Rudy (*authors' closure*)—We appreciate the observations of Dr. Summers, which emphasize the importance of making "apples-to-apples" comparisons. We are well aware of the flow limitations inherent to his specific application, namely, the "Hydrominer," and did not intend in our comparisons to imply that this was the best specific energy which he could produce. As stated in our paper, however, the objectives of this CAVIJET study were much broader; that is, we were not limited to a particular mining device. This program required us to examine the feasibility and effectiveness of using much lower pump pressures plus cavitation phenomena to cut coal. We succeeded in reaching these objectives, and the comparisons made with Dr. Summers' earlier work serve only as an example of the results of our investigation.

¹University of Missouri-Rolla, Rolla, Mo.

Marine Applications of High-Pressure Waterjets

REFERENCE: Hilaris, J. A. and Labus, T. J., "Marine Applications of High-Pressure Waterjets," *Erosion: Prevention and Useful Applications*, ASTM STP 664, W. F. Adler, Ed., American Society for Testing and Materials, 1979, pp. 582-596.

ABSTRACT: High-pressure waterjets were investigated for hull cleaning, metal cutting, and concrete weight coating removal from submarine pipelines. All testing was performed in the submerged condition and a selective material removal capability was observed for the hull cleaning operation. This selective material removal capability was a sensitive function of jet pressure and jet angle at fixed cleaning rates. Results for the metal cutting indicated that positive jet angles and low concentrations of polymers could increase depth of cut significantly. Projected concrete weight coating removal rates were five times that achieved by conventional methods.

KEY WORDS: jet cutting, hull cleaning, metal cutting, underwater cutting operations, high-pressure waterjets, erosion

Offshore construction activities have increased dramatically as the energy industry continues to develop various ocean resources. This activity has defined the need for improved underwater construction tools and techniques to increase the efficiency of the working diver, and where possible introduce automation for cost reduction. Waterjets hold the potential for achieving these goals over a broad range of marine activities. Currently, waterjets are used for ship hull cleaning in drydock operation [1],³ offshore rig structural cleaning, cable trenching operations, and heat-exchanger descaling. This investigation deals with underwater ship hull cleaning, metal cutting, and the removal of concrete weight coatings from submarine pipelines.

The hull cleaning studies were aimed at establishing the proper jet parameter combinations that would allow the removal of marine fouling from metal surfaces having an antifouling coating, without damaging this coating.

¹Associate research engineer, IIT Research Institute, Chicago, Ill. 60616.

²Engineering consultant, SCIRE Corporation, Downers Grove, Ill. 60515.

³The italic numbers in brackets refer to the list of references appended to this paper.

A basic investigation of underwater metal cutting by waterjet was undertaken to establish performance levels for this method. The influence of nozzle size, jet pressure, cutting rate, jet angle, abrasive injection, and fluid additives was evaluated with the goal of increasing the cutting rate for a given power input. Abrasives were evaluated both in the submerged and ambient condition to establish the influence of the water environment.

Concrete weight coating removal studies were aimed at establishing the performance of the jet as compared with conventional methods, and to determine if a nonpenetrating nozzle could be used to achieve complete coating penetration. This process and the hull cleaning operation can be automated to greatly enhance the diver's work efficiency for a given bottom time.

Experimental Operations

The underwater testing for the cleaning and metal cutting studies was performed in the test tank shown in Fig. 1. A specimen carriage is mounted in the bottom of the tank and driven through a timing belt arrangement by a hydraulic cylinder. Limit switches were provided at the extreme points in the travel to provide automatic reversing of the carriage. The nozzle was mounted on a rigid bar with standoff distance maintained at 12.69 mm throughout the test programs. For the cleaning studies, two groups of test specimens were utilized: (1) plain steel specimens and (2) steel specimens

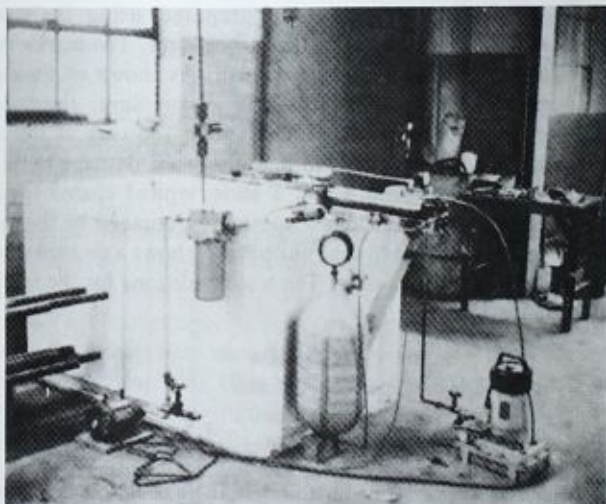


FIG. 1—Underwater test tank.

with an antifouling paint coating. An accumulator system was used for the cleaning studies. A 82.7-MPa pump was used to charge a large-volume accumulator to the appropriate test pressure. The accumulator was then discharged through a lance containing the cleaning nozzle, producing a high-pressure jet.

The main high-pressure laboratory intensifier was employed for the metal cutting and concrete weight removal studies. This unit is a gas-backed linear intensifier capable of 1379-MPa bars pressure and power outputs in excess of 447 kW. A detailed description of this unit is given in Ref 2.

Cleaning Test Results

The initial criteria established for evaluating the results of the cleaning tests were mass loss and damage caused to antifouling coating for specified test conditions. Areal exposure rates which relate to cleaning applications were not determined. Figure 2 shows the effects of jet pressure and jet angle on the mass loss for both coated and uncoated specimens (that is, with and without antifouling paint). Test pressures ranged from 51.7 to 65.5 MPa and jet angles from 0 (normal impact) to a positive 45 deg. Figure 3 shows a similar plot but with cleaning rate as the major independent variable. The uncoated specimens show the highest weight loss because the fouling, in general, was much greater on these specimens. The fouling was generated by exposing the specimens in a marine environment at the Naval Coastal Systems Laboratory in Panama City, Florida. Much of the scatter in the data for the uncoated specimens was due to nonuniform fouling distribution. The coated specimens were prepared using the standard anti-fouling paint and standard application procedures. The marine fouling consisted of barnacles and other marine growth. As shown on these plots, increased mass loss occurred with increasing jet pressure, cleaning rate, and shallow jet angles. This must be qualified in the case of the coated specimens, since jet angles less than 45 deg produced damage to the anti-fouling paint undercoat. Figures 4 and 5 show typical coated specimens cleaned by a waterjet. Figure 4 shows a specimen damaged by the waterjet when the jet angle was less than 45 deg, while Fig. 5 shows a cleaned specimen without damage to the undercoating. The test conditions for the specimens shown in Figs. 4 and 5 were

jet pressure:	65.5 MPa
nozzle diameter:	0.4 mm
cleaning rate:	30.5 cm/s
jet angles:	0 and 45 deg, respectively

The initial testing was performed with circular nozzles, but a rectangular slit nozzle was also tested. The rectangular nozzle had an opening of 1.52 by 0.25 mm with an initial entry angle of 13 deg and exit angle of 0 deg.

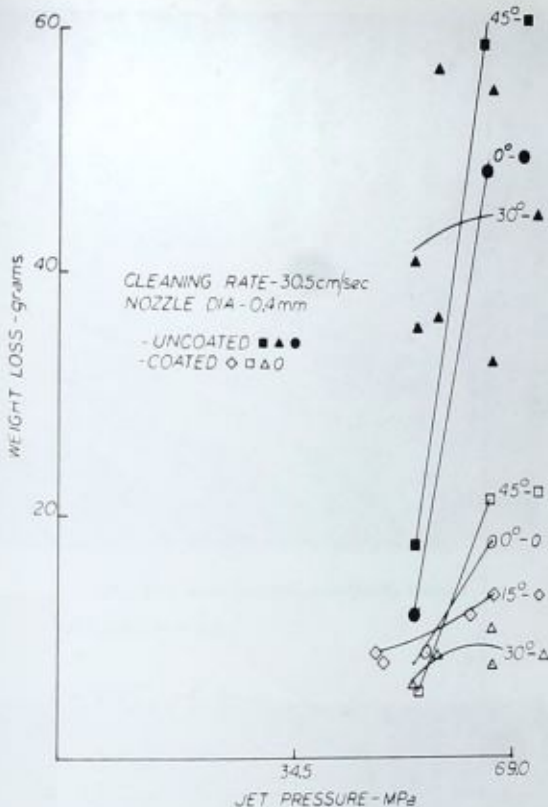


FIG. 2—Weight loss versus jet pressure for coated and uncoated specimens at various jet angles.

Testing was performed with the long dimension parallel and perpendicular to the direction of cleaning. This alternative design produced a 275 percent increase in mass loss as compared with the circular nozzles, but both designs had equivalent specific energies. This increase occurred regardless of the nozzle orientation since the jet was oscillated while it was moved across the fouled surface. Thus, both nozzles are approximately equal in mass removal efficiency at equivalent operating conditions, and the judgment on which nozzle to use will be based on other considerations such as cost, wear, thrust, areal exposure rate, and exposure rate/kilowatt-hour of energy input.

From the foregoing results, the operating conditions of a cleaning system should be at a rapid cleaning rate, a low jet angle, and an operating pressure

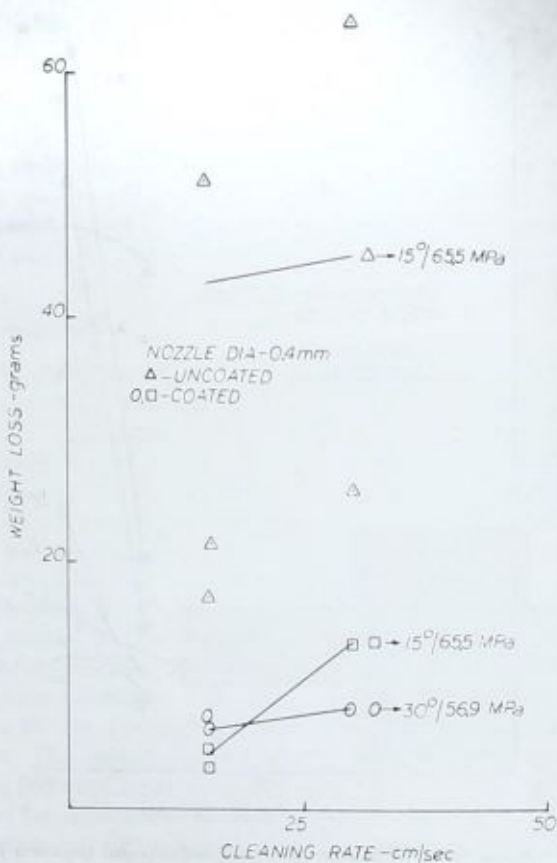


FIG. 3—Weight loss versus cleaning rate for coated and uncoated specimens for various jet angles and pressures.

consistent with power availability and the requirements for fouling removal. These conditions must be modified when cleaning hulls with anti-fouling paint, in that the jet angle should not be below 30 to 45 deg to insure consistent removal of the marine growth without causing damage to the antifouling undercoat. By keeping the antifouling undercoat intact, the benefits of low power consumption due to reduced fouling of the ship hull could be realized without the need for a repainting of the hull.

Metal Cutting Studies

In a second experimental study, the influence of the various jet parameters



FIG. 4—Coated specimen damaged by waterjet.



FIG. 5—Coated specimen cleaned and undamaged by waterjet.

laden tape on the surface of the metal along the cut path. The effects of standoff distance, which is a significant parameter in metal cutting, and abrasive effectiveness are illustrated in Fig. 9. For the current investigation, d/s (s is the standoff distance) lies in the range of 0.032 to 0.39, which is at the low end of the curve. All of the curves shown are for water only, except the water-sand curve, which illustrates the effect of sand particles (nominally 0.25 in mm size, rounded profile) injected into the jet stream at the exit of the nozzle, as opposed to cutting through a sacrificial material directly at the surface. Using the nozzle method of injection, the abrasive jet outperformed the water-only jet by 25 percent. This change was obtained at an increase of the power requirements by 0.13 percent. The data in Fig. 9 are for testing in air, hence they must be qualified for submerged operation. But past experience has shown that the trends are generally not altered substantially, hence the conclusions drawn should still be valid.

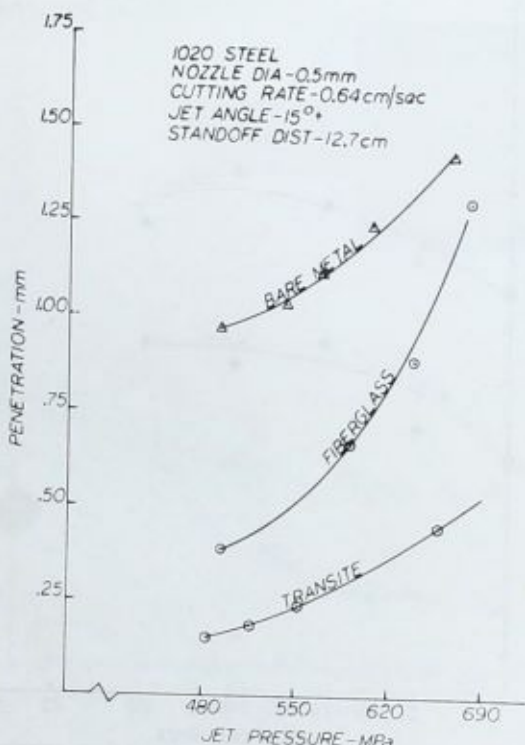


FIG. 8—Penetration versus jet pressure for 1020 steel and various abrasives.

Fluid additives have been investigated previously for other materials and have been found to contribute to the cutting capabilities of the jet. Figure 10 shows the effect of various concentrations of additive BX-254 (NALCO Chemical Co.) on the penetration. Similar tests were run on the 0.5-mm nozzle with similar results, but not as large as for the 0.4-mm nozzle. This decrease in additive effect with increasing nozzle size has been observed by other investigators [3].

Combining all these results together, a series of tests was performed on HY80 using various combinations of these best parameters. Figure 11 shows the results for the HY80 test specimens. As previously indicated, the additive augmented jet at a jet angle of 15 deg should give the best results, which Fig. 11 verifies. Note also that the abrasive jet does not enhance the cutting for HY80. This may be caused by the change in material properties of the HY80 versus the 1020 steel. (The abrasive was not changed.)

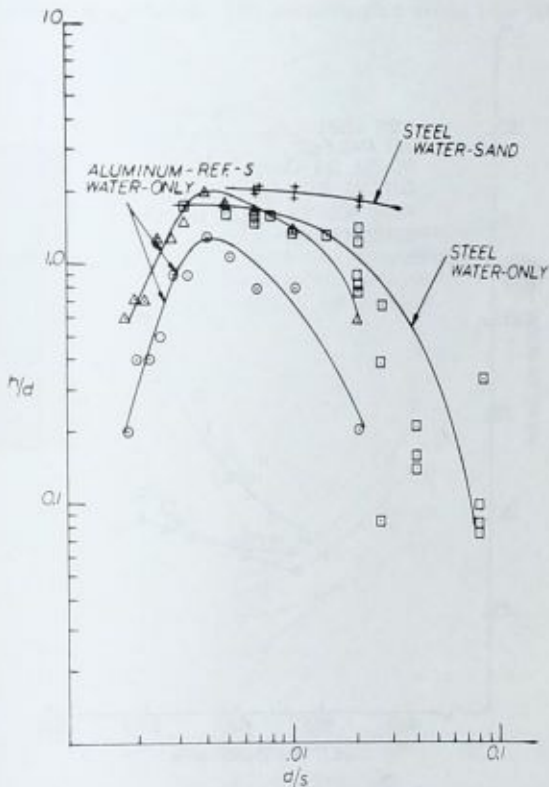


FIG. 9— h/d versus d/s for steel and aluminum.

The combined additive-abrasive jet was the least successful, indicating that these two augmentation techniques are not mutually beneficial under the stated operating conditions.

Concrete Weight Coating Removal Studies

Maintenance and construction of submarine pipelines present some unique problems due to the hostile work environment. Conventional methods of removal of concrete weight coatings are time-consuming, costly, and can cause physical damage to the pipelines. Jet cutting systems may provide a more cost-effective method of attacking these coatings. Figure 12 shows the required number of passes to achieve a full-depth cut (that is, to the surface of the steel pipe) for two typical concrete weight coatings. Coating No. 1 was a relatively weak concrete with a chicken wire reinforcing used.

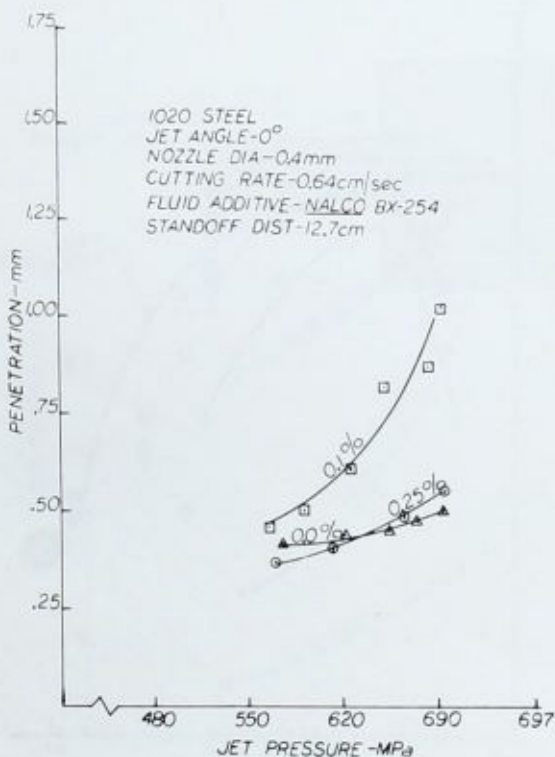


FIG. 10—Penetration versus jet pressure for 1020 steel and various jet augmentation combinations.

The almost uniform depth of cut per pass reflects this condition. Coating No. 2 was higher-strength concrete with 0.54-cm steel reinforcing rods. Note that the 0.5-mm nozzle takes one less pass to achieve full penetration, but requires 3.3 times the power of the 0.4-mm curve. Although more power is required by the larger nozzle, it may still be more cost-effective since the economics of this particular application are dictated by labor costs and overall time requirements. If an automated approach is taken, then the smaller nozzle diameter system would be the most cost-effective, since only the cycle-time would influence the operational costs significantly. Capital costs would also be less for the small system if a full 100 percent duty cycle were utilized. The performance curve shown in Fig. 12 is for a nonpenetrating nozzle (that is, a nozzle remaining outside the kerf, as opposed to a penetrating type, which follows into the kerf).

A bottom-operated system would provide the greatest flexibility of operation, but space and weight restrictions would most probably limit it to a duty-cycle type of operation. The intensification would take place on the

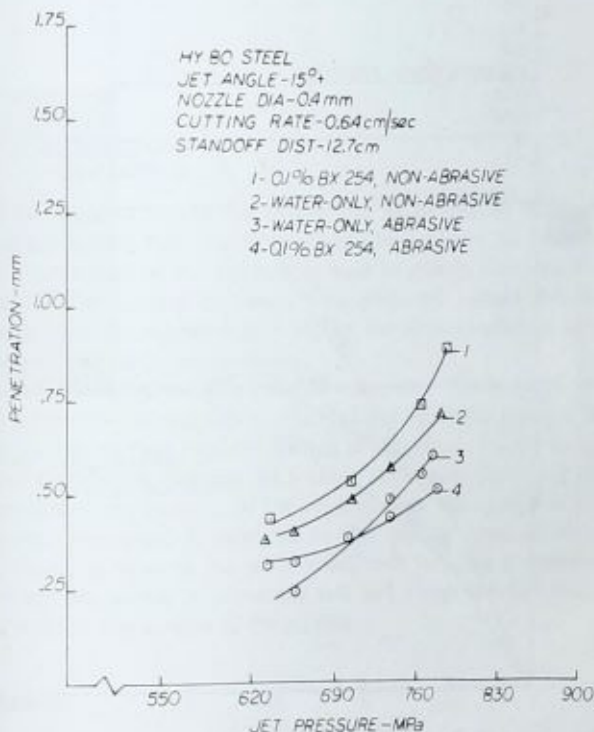


FIG. 11—Penetration versus jet pressure for HY80.

bottom with the high pressure transmitted to the work station via rigid tubing and swivel joint connections. The power source could be surface or bottom mounted. For buried or partially buried pipelines a manually operated low-pressure system could be used to remove the backfill from around the pipe prior to attaching the automated system to the pipe.

From the data in Fig. 12 the average exposure rate is $25.4 \text{ cm}^2/\text{s}$ (Coating No. 1); thus for the particular pipe tested (that is, outside diameter = 0.78 m with a 12.7-cm concrete/asphalt coating) a cutting time of 567 s per linear metre at continuous operating pressure is anticipated. The geometry of the cut is shown in Fig. 13. For a duty-cycle operation, the cutting time is given in Table 1 for various power levels. For a 2.43-m-long section of pipe, and working at an average power level of 22.4 kW, 177 min (2.95 h)

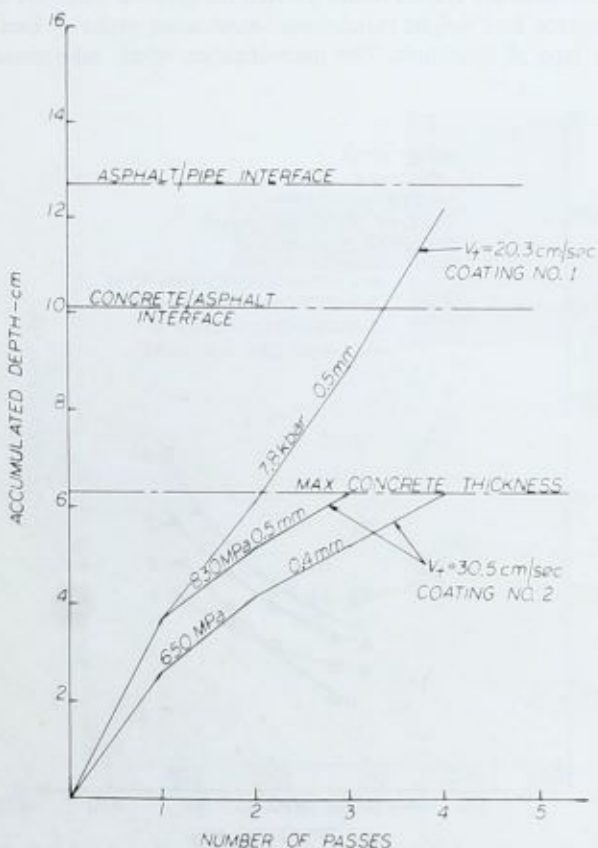


FIG. 12—Accumulated depth versus number of passes for concrete weight coatings.

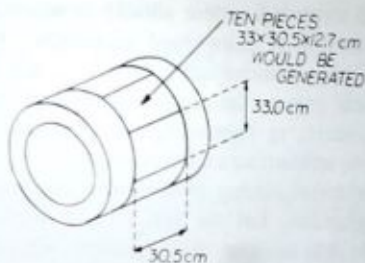


FIG. 13—Concrete weight coating cut geometry.

TABLE 1—Power requirements/cutting time summary for different duty cycles.

Average Power, kW	Duty Cycle, %	Cutting Time per 30.5 cm Length, s
176	100	173
112	63	274
75	42	412
37	21	823
22	13	1330
15	8	2162

would be required to cut the length into 33 by 30.5 by 12.7-cm blocks. The actual cutting time would be slightly longer since the jet would dwell at the intersection of the reinforcing bars to enlarge this area to create a tool access for cutting the bars. This projected cutting time compares favorably with the reported 16 h [4] for the same conditions using mechanical saws and chipping hammers.

One additional point is worthy of note, and that concerns the safety of this approach with respect to potential damage to the pipeline. Referring to Fig. 6, the cutting rate for steel is in the range of 0.64 to 1.29 cm/s and for the weight coatings 20.3 cm/s. This wide difference in cutting rate precludes any damage to the pipeline since the cutting of steel, even at elevated pressures, is restricted to slow cutting rates. At high cutting rates, the dwell time of the jet is insufficient to cause penetration. Thus the jet cutting system is inherently safe and allows complete material removal down to the surface of the pipeline.

Conclusions

The use of waterjets for submerged cleaning of ship hulls and other structures has been clearly demonstrated. Integration of the jet systems

with an automated traversing system should produce a viable technique for cost-effective cleaning of submerged structures. A selective removal capability has also been demonstrated, which is not currently available in present mechanical systems. Jet angle and pressure have been shown to be significant parameters in controlling the removal of marine growth without damaging the antifouling undercoating.

Results from the metal cutting studies are inconclusive to determine its commercial application, but the test data indicate that the process would be limited to thin sections. Also, positive jet angles and fluid additives increased penetration, while abrasive injection using a sacrificial material at the surface of the metal did not enhance penetration. In its present state, the continuous jet is not competitive with conventional techniques on an economic basis, but may be justified if an explosive environment exists where conventional techniques cannot be utilized safely.

A significant reduction in process time was established for stripping of weight coatings from submarine pipelines by using waterjets. The safety of the system should be also much greater due to the mutually exclusive cutting regimes for each material. Full penetration of the coating could be achieved using a nonpenetrating nozzle, which can simplify the operation considerably. The economics of the system are yet to be established, but at this point are worthy of serious consideration.

Acknowledgment

This work was partially supported by the Naval Training Equipment Center. Mr. R. E. Elliott of the Naval Coastal Systems Laboratory acted as program monitor and provided valuable input.

References

- [1] Pardey, P. H., "Notes On Marine Applications of Jet Cutting," *Proceedings*, First International Symposium on Jet Cutting Technology, Paper No. D2, British Hydromechanics Research Association, Fluid Engineering, Coventry, England, 5-7 April 1972.
- [2] Labus, T. J. and Hilaris, J. A., "An Experimental Investigation of an Underwater High Pressure Water Jet Metal Cutting Tool," for Naval Training Equipment Center, IITRI Report No. D6103, Illinois Institute of Technology, Jan. 1976.
- [3] Savanick, G. A., Ricketts, T. E., Lohn, P. D., and Frank, J. N., Bureau of Mines Report of Investigations No. 8095, 1975.
- [4] Guardiano, A., personal communication, Taylor Diving and Salvage Co., 1975.
- [5] Franz, N. C., "The Influence of Standoff Distance on Cutting with High Velocity Fluid Jets," *Proceedings*, Second International Symposium on Jet Cutting Technology, Paper No. B3, British Hydromechanics Research Association, Fluid Engineering, Cambridge, England, 2-4 April 1974.

Use of High-Pressure Waterjets in Utility Industry Applications

REFERENCE: Huszarik, F. A., Reichman, J. M., and Cheung, J. B., "Use of High-Pressure Waterjets in Utility Industry Applications," *Erosion: Prevention and Useful Applications*, ASTM STP 664, W. F. Adler, Ed., American Society for Testing and Materials, 1979, pp. 597-615.

ABSTRACT: During the past several years, waterjets with pressures up to 408 MPa have become a reliable tool for industry and have been used for a variety of factory applications. In addition, waterjets have been tested for rock cutting in mining and tunnel applications. The utility industries do a considerable amount of work that requires excavation in rock and concrete. The potential of using high-pressure waterjets to meet their field needs has been considered. To date, the telephone, electrical power, and gas industries have conducted studies on the use of high-pressure waterjets. This paper contains descriptions of the various applications of waterjets in the utility industry, descriptions of the appropriate equipment and cutting techniques, discussions of some possible systems and their operating parameters, and an economic analysis of waterjet methods for trenching and pole-hole drilling.

A study was conducted to examine the use of waterjets in utility industry applications. The study was a three-phase program. In the first phase, the possible applications and their significance to utility company operations were examined. In the second phase, a strategy for cutting rock and concrete with waterjets as well as a conceptual system design was developed. Various rock types were tested, and rates were predicted for two specific applications: trenching and pole-hole drilling. In the third phase an economic analysis of the cost of using waterjet methods for trenching and pole-hole drilling was performed and costs were compared with current methods on a per-hole or per-foot of trench basis. In addition, the advantages and disadvantages of waterjet methods on a system basis were compared with those of existing methods.

The study has demonstrated that there is a wide variety of applications for high-pressure waterjets in the utility industry. The study further shows that waterjet devices are both technically and economically feasible. The predicted rates and the costs indicate that, in rock, the waterjet system is better than current methods.

A detailed overview of this study as well as the results are presented in this paper.

KEY WORDS: high-pressure waterjets, utility applications, trenching, pole-hole drilling, deep-kerfing, hard rock, erosion

¹Manager, Construction Methods, Bell-Northern Research, Ottawa, Canada K1Y 4H7.

²Senior research scientist, Flow Industries, Inc., Kent, Wash. 98031.

Background

In North America, utilities such as power, telephone, water and sewer, gas, and more recently cable television deal with at least one common element in the construction of their distribution systems: the ground. Depending on the location, the ground can provide the ideal medium for cost-effectively constructing distribution systems, or it can be the major cause of high construction costs and inefficiency.

In order to fully appreciate the impact of ground conditions on utility construction, it is important to become aware of two basic facts. First, in recent years public and political pressure in both the United States and Canada has forced the power and communications utilities to construct more and more of their distribution systems below ground as opposed to aerial. This policy of "out-of-sight" distribution systems has had a major impact on both construction and maintenance costs, especially in areas where the ground is predominantly rock.

Secondly, from a geological point of view, only about one third of the populated areas of Canada and the United States can be considered to be good burying areas. These areas consist generally of the Canadian Prairies and the Midwestern and Southeastern parts of the United States. The rest of the continent is either bare rock or a mixture of rock and soil in various proportions. An example of the impact of these ground conditions on below-ground telephone cable installation costs is found by comparing cable installation costs in the Canadian Prairies with those in Eastern Canada. In the Canadian Prairies, cable can be installed by plowing at a cost of approximately 66 to 164 cents per metre. The cost of installing the same cable in the eastern part of Canada, where the ground is predominantly hard rock, can be as high as 49.2 dollars per metre.

These two prime considerations have forced utilities to reevaluate the construction methods which have traditionally been used to construct below-ground distribution systems. Obviously, cheaper and faster installation methods for poor ground conditions such as bouldery soil, hardpan, soft, and hard rock are essential requirements for reducing utility construction costs. High-pressure waterjetting, as applied to cutting rock for various utility construction applications, is one technology which may result in new space-age construction tools capable of meeting these requirements.

Waterjetting: Utility Construction Applications

Based on the present and predicted future capabilities of waterjets, several aspects of utility construction appear to qualify as potential users of this technology. A number of these, together with a system concept, are described in the following. It should be remembered that none of the tools described herein have yet been developed. Therefore, it is difficult to

ascertain the specific operational characteristics of each concept at this time.

Drilling Pole-Holes in Bedrock—A rotating nozzle head or waterjet-mechanical cutter, using one or more nozzles, could be used to cut a circular slot in bedrock to any diameter. The remaining rock cylinder would be mechanically fractured and removed, leaving a hole slightly larger than the pole diameter. The space around the pole could be efficiently backfilled with an expanding semirigid urethane foam.

Drilling Guy Rod Anchor Holes—The drilling device used for this application would probably be similar to the pole-hole cutting equipment just described. Most anchor holes need be only 5.08 cm (2 in.) in diameter and 45.72 cm (18 in.) deep. A hybrid system, combining waterjets with a mechanical cutter, would significantly increase penetration rates compared with standard drilling devices.

Frozen Soil Excavation—In most of Canada and the Northern United States, the extension of construction activities into the winter months is always a primary objective. To meet this objective, a waterjet system combined with a conventional frost saw or blade may be feasible. This type of hybrid system would not only increase the cutting speed, but also reduce both wear and general maintenance costs. Furthermore, this type of cutting operation would result in fewer cleanup problems.

Rock Trenching—A hybrid waterjet-mechanical cutter or rotating nozzle head system could be used for this application. The hybrid cutter would consist of a rolling-disk cutter assisted by waterjets located ahead of the cutting edges. The jets would cut narrow slots into the rock face, allowing the disk cutter to easily break to the unconfined rock kerfs. A mucking system incorporated into the unit would remove the fractured rock particles from the trench. Alternatively, a rotating nozzle head (or heads) could cut 1.27- to 2.54-cm ($\frac{1}{2}$ to 1 in.)-wide parallel slots into the rock surface to a depth which would allow a loaded wheel to break the remaining rock ridges between the slots. After removing the broken rock, the process would be repeated until the desired depth is achieved.

Road Crossings—Two alternatives appear feasible. The first method requires the waterjet to "slice" the concrete or asphalt into pieces, which are then removed by hand. A mechanical trencher or backhoe is then used to excavate the base material to the required depth. As with normal road crossings, only one lane at a time need be closed to traffic.

The second method would necessitate the digging of a pit if existing ditches were not deep enough or ditches were not present at all. If the road bed material was well compacted, the waterjet would be able to cut without fear of the hole collapsing. In the case of loose material, a pipe could be pushed behind the waterjets as it advanced.

Ice Cutting to Access and Install Submarine Cable—A low-pressure waterjet unit 69 to 138 MPa (10 000 to 20 000 psi) with a hand-held nozzle

head could be used to cut through ice buildups on rivers and lakes. This technique would be faster as well as less tedious than cutting with chain saws.

Concrete Cutting—Present research has shown that waterjets can be used effectively to clean and cut concrete surfaces. The jet erodes away the cement and fine aggregate content of the concrete, without cutting through the larger aggregate. The large aggregate can be cut, but the erosion method allows the use of lower pressures to penetrate any strength concrete.

A waterjet capable of cutting concrete would have useful application for cutting duct entrances in manholes or building walls or even removing entire wall sections to allow for building expansion.

Large-Diameter Tunneling (Utilidor)—This application would have an effect not only on utility construction, but also on subway construction and the mining industry. The large tunnel sizes dictate the use of many jets working simultaneously with mechanical cutters. The main advantages this method would have over drilling and blasting include higher productivity, and a reduction in the safety and health hazards, and weakened tunnel roofs due to blasting.

Duct Cleaning—Waterjetting machinery is available which is capable of cleaning and scouring cable ducts. Obstructions can be dislodged and soil buildup on duct walls removed. The nozzle head advances under its own power by means of low-pressure, high-volume jets directed backwards against the duct wall. At the front of the nozzle head, a high-pressure, low-volume jet cuts through obstructions, while radial high-pressure jets scour the duct walls. Dislodged material is carried out of the duct when the nozzle head is retrieved.

Research Scope and Objectives

In an effort to evaluate the technical feasibility of using high-pressure waterjets for utility construction, a study was conducted aimed specifically at rock trenching and pole-hole cutting. Cutting tests on nine different specimens of rock were performed. These rocks were representative of the types commonly found in Eastern Canada. They include limestone, sandstone, granite pegmatite, biotite granite, quartzite, and granite-quartz. Based on the cutting characteristics of these rocks, conceptual designs of a waterjet rock trencher and pole-hole cutter were developed. Details of the research program are presented in the following section.

In addition to the technical evaluations, the operational requirements and economics of waterjet construction tools were studied. This was achieved through a field survey which identified the field requirements and present construction costs commonly experienced in Eastern Canada. The results of this part of the investigation are also discussed.

System Concepts

Method of Cutting

Continuous waterjets can be used in two ways for the applications of interest to the utility industry. In the first method, waterjets can be used to cut narrow slots which assist mechanical cutters. In the second, a combination of jets, oscillating or rotating, can cut a wide, deep slot which completely defines the shape of material to be removed. The remaining material can then be removed by energy efficient mechanical means. For the study conducted by Bell-Northern Research Ltd. and Flow Industries, Inc., the wide-slot, deep-kerf method was examined. The applications considered were pole-hole drilling and trenching in soft and hard rocks.

To demonstrate the technical and economic feasibility of waterjet trenching and pole-hole drilling, it was necessary to conduct test cutting experiments to determine operational parameters and operating rates. It is only with data such as these that estimates of cost per foot or cost per hole can be made. To determine deep-kerfing rates, linear cutting experiments must be conducted. Typically, jet pressure P_o , nozzle diameter d_o , and traverse velocity v_t are varied so that optimum cutting can be determined and scaling factors established. Figures 1-3 show typical linear cutting curves for some of the rocks tested. The standoff distance, l_o , is also indicated on these figures.

The method chosen to cut the deep kerf utilizes a nozzle with two angled jets. The jets are angled so that they cut a slot that is wider than the nozzle. The wide slot enables the nozzle to enter the slot and to maintain an effective standoff distance for both cutting rate and slot shape. In order to cover the material in the slot, the nozzle is oscillated. The resultant coverage pattern is shown in Fig. 4. The method of motion chosen was oscillation because, by applying a torsional force to a length of tubing, the necessary motion can be obtained without the use of any dynamic seals or swivels. The cut made by this device is shown in Fig. 5.

For an oscillating nozzle, the conditions for the jet can be determined from linear cutting tests. The oscillation frequency is directly related to the traverse velocity v_t ; pressure and diameter of the jets are determined by the rock to be cut and available power. The cutting parameter that must then be optimized is the nozzle feed rate v_f . Such optimization curves are shown in Fig. 6 for different conditions.

From tests such as the linear cutting tests and the kerfing tests previously described, the cutting rates for the nine rock types indigenous to Eastern Canada were determined. These rates were incorporated into cutting schemes so that projected operational rates could be determined. The cutting equipment and rates are presented next.

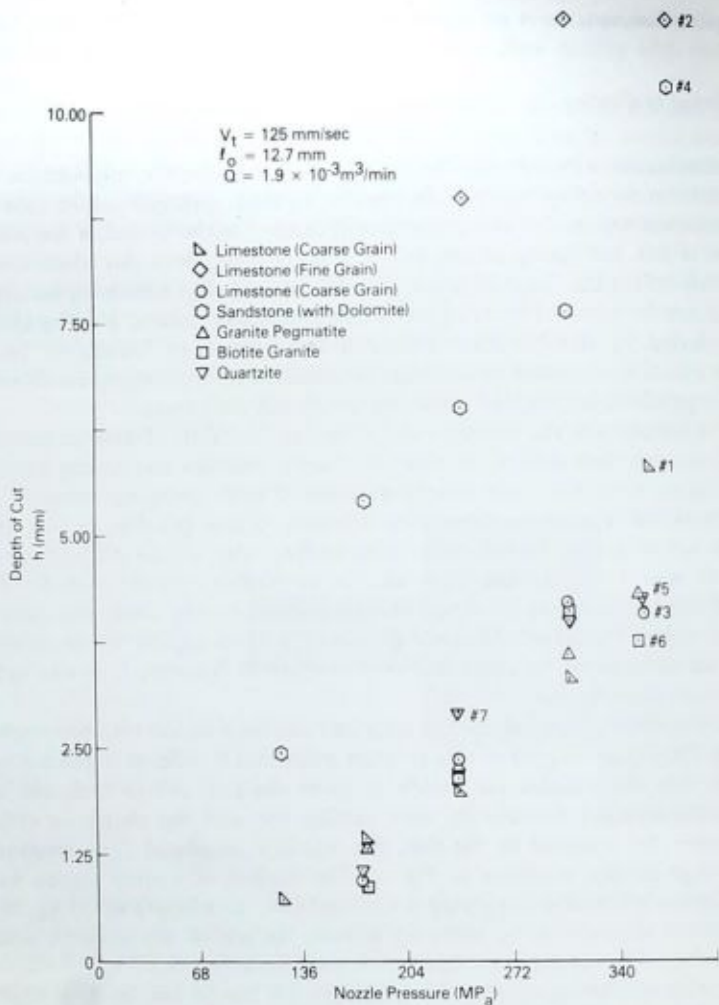


FIG. 1—Effect of pressure on depth of cut.

Operating Systems

Figure 7 shows a system concept for trenching and for drilling pole-holes with waterjets in rugged off-road terrain. The basic system components consist of a hydraulic power trailer, a water truck, a tractor, a trencher, and a pole-hole drilling device. Each component is described in the following.

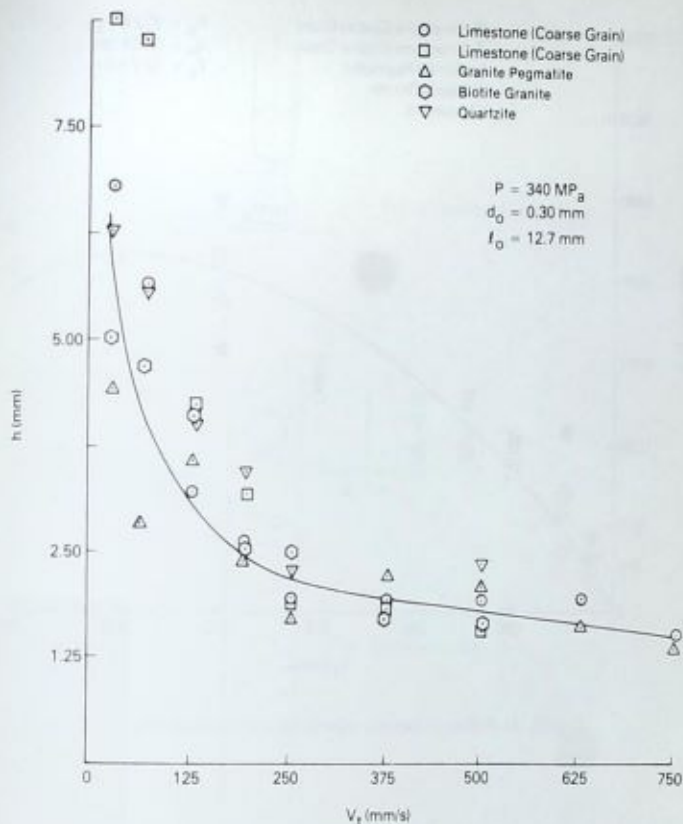


FIG. 2—Effect of traverse velocity on depth of cut.

The hydraulic power trailer consists of a diesel engine and hydraulic oil pump to power the intensifier, as well as an oil reservoir and oil cooler. The trailer also has space to place the tractor for transportation between sites. The engine on the trailer that is chosen must be able to power a 188-kW intensifier, which will be mounted on a tractor. These 188-kW intensifiers have been field-tested and have proven to be reliable pieces of equipment.

The tractor is used to carry the high-pressure intensifier and all trenching and drilling equipment, and to move it along the work area. The tractor is attached to the trailer by an umbilical cord, which contains an oil powerline, an oil-return line, and a water line. The umbilical cord is flexible and allows the tractor to move independently of the trailer, thus

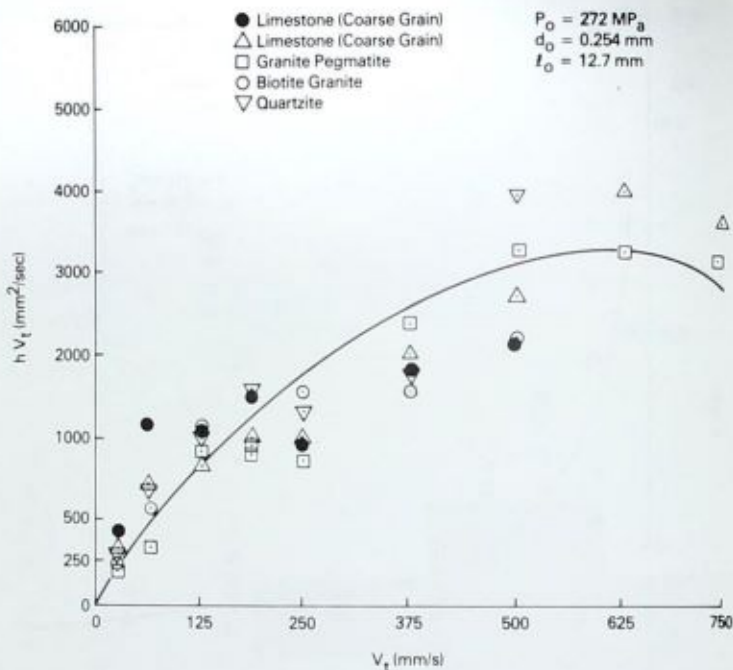


FIG. 3—Effect of traverse velocity on area removal rate.

minimizing the number of times the entire system must be moved. The intensifier is separated from the hydraulic power package for two reasons. First, flexible tubing can be used between the trailer and tractor instead of the rigid tubing that would be necessary if the intensifier were mounted on the trailer. Second, if both the hydraulic power package and the intensifier were mounted on the tractor, the tractor would have to be large, and its ability to move over very rugged terrain and to work in confined areas would be hampered.

The tractor and the hydraulic trailer form the heart of the system. With these two components, waterjet cutting systems for various applications can be mounted on the tractor to do the desired job. Devices for trenching and pole-hole drilling have been conceptually designed. Both systems, mounted on a tractor, are shown in Fig. 7. The details of these systems are presented in the following subsections.

The final component of the system is the water truck-trailer. This component supplies the water for the jets and the oil cooling water. It

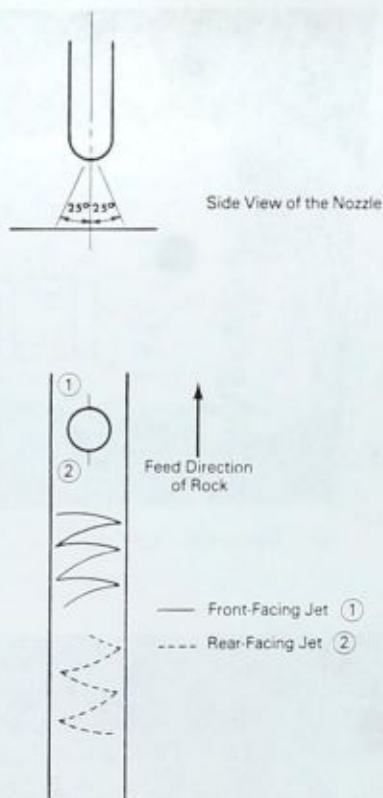
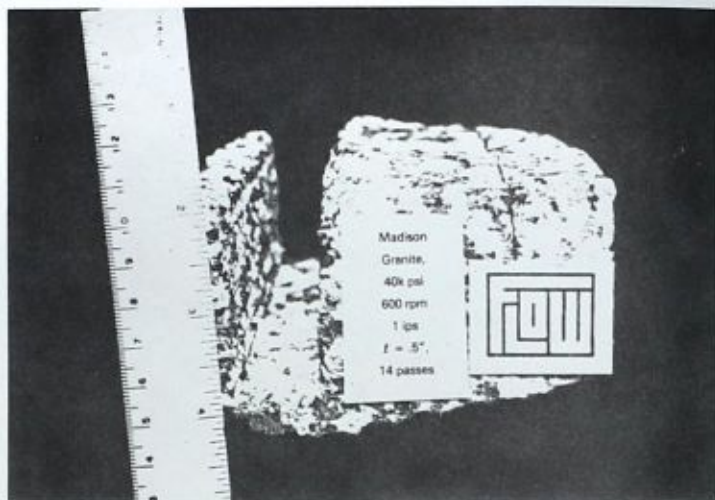


FIG. 4—Deep-kerf nozzle coverage pattern.

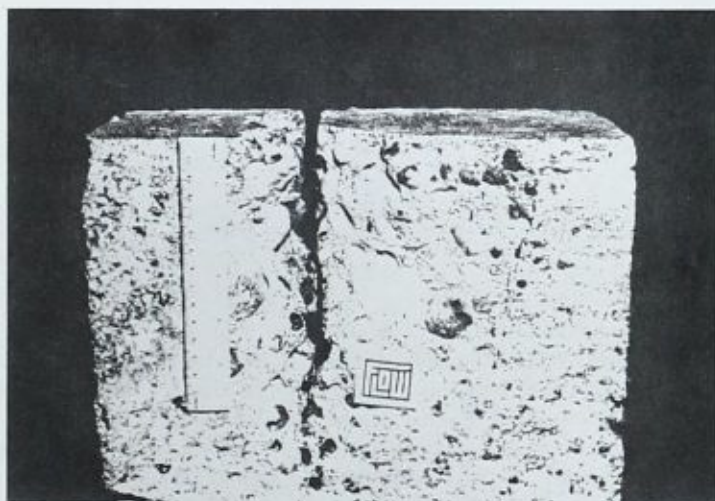
would require 0.028 m^3 of water per minute to provide 188 kW and a waterjet pressure of 374 MPa. Based on a running time of 6 h/day, 10 m^3 of water per day would be necessary. Since water may not be available at the work site, this amount of water can be supplied best by a water truck.

These three components—the water trailer, the tractor, and the hydraulic power trailer—make up the waterjet cutting system. When used in conjunction with special devices, this system can be used for trenching and hole drilling in addition to other applications.

Waterjet Trenching Device—Both the waterjet trenching device and the pole-hole drilling device operate on the same principle of cutting. Both devices use an oscillating deep-kerf device to cut the slot. In addition, both have a mechanical breakout device which removes large pieces of material,



(a) Deep-Kerfing Cut



(b) Three Parallel Cuts (Multiple Pass)
(Clear Slot Depth = 51 mm)

FIG. 5—Oscillating kerfing cuts and parallel linear cuts.

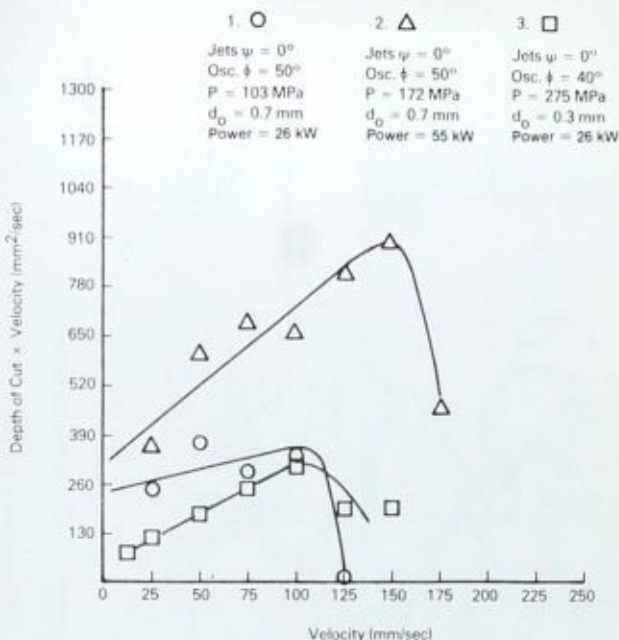
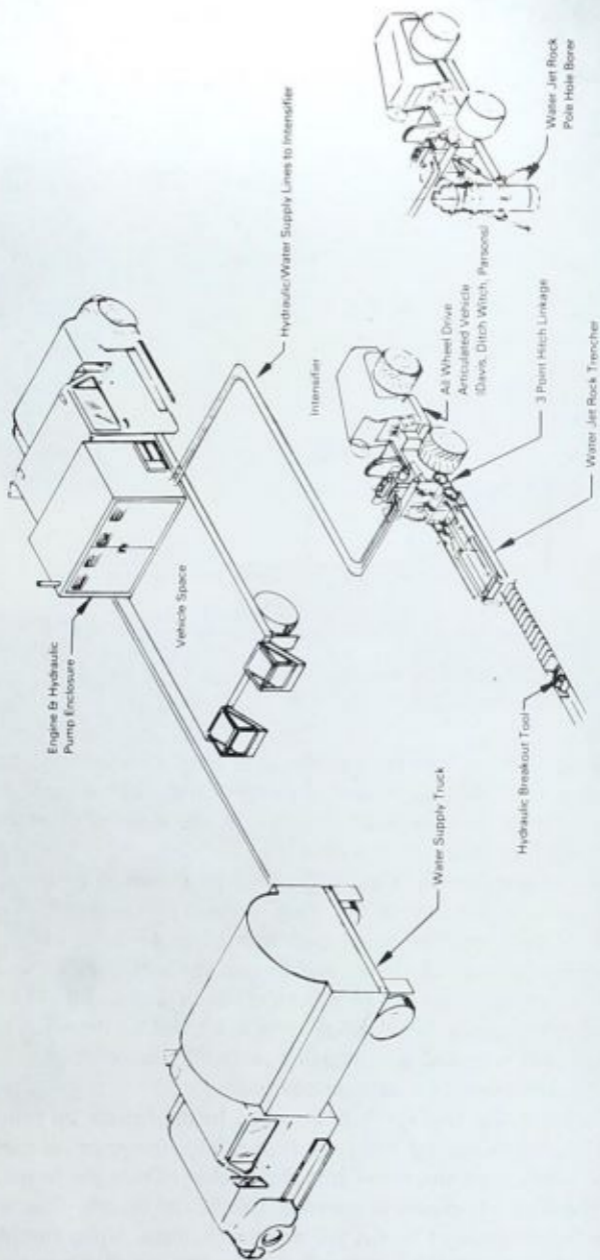


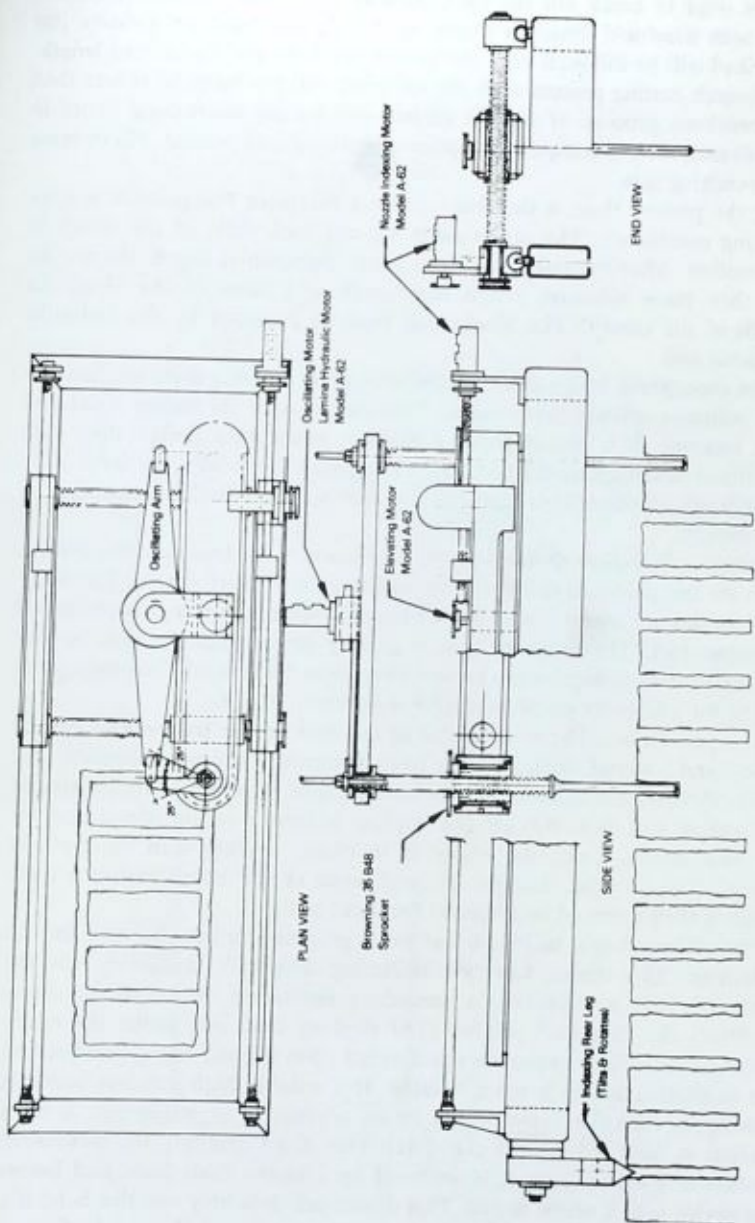
FIG. 6—Effect of horsepower on cutting performance.

thus minimizing the amount of material that must be excavated by the oscillating deep-kerf device. From laboratory and field experience, a combination waterjet and mechanical system is the most efficient system from both energy and time considerations.

Figure 8 is a conceptual drawing of the waterjet trenching device, which consists of a pair of oscillating nozzles, each of which is capable of delivering up to 94 kW to the rock. The nozzles are located on a frame, which gives them the necessary motion. Each nozzle has controls that allow x - y - z motion in order to cut a trench of a desired depth and width. The x - y - z motion is controlled hydraulically from controls located on the tractor. The nozzle oscillation is supplied by a rotating hydraulic motor which converts the rotation to oscillation by a cam-type arrangement.

The frame, as shown in Fig. 7, is attached to the tractor by hydraulic cylinders which can raise and lower the frame. This movement is used for adjusting the position of the frame and for leveling. Once the frame is in place, the trenching operation is controlled from the tractor. The trench is cut to the length allowed by the traverse mechanism. Upon completion of a given length of trench, the tractor raises the frame and moves forward





to the new position. While the tractor is being moved, a hydraulic breakout tool is used to break out the rock sections left by the waterjet trencher. One such handheld device is shown in Fig. 7. The basic progression just described will be followed until the trench has been cut the desired length. The trench cutting process with the waterjets will probably be slower than the breakout process. If so, the cutting will be the controlling factor in the advance rate. Consequently, optimizing the cutting process will increase the trenching rate.

At the present time, a trenching method that uses two pairs of nozzles is being considered. The two nozzles will cut both sides of the trench in one motion. After the sides have been cut to the desired depth, the nozzles will then move sideways across the trench and form blocks along the length of the trench. The blocks will then be removed by the hydraulic breakout tool.

The conceptual design in Fig. 8 includes some possible drive mechanisms and indicates various components. This design is by no means a detailed one; however, it is meant to be a realistic conceptual design that, with additional detailing, could be built. Changes to the design will have to be based upon considerations of the terrain, environment, and actual operating parameters.

Waterjet Pole-Hole Driller—As in the trencher, the basic cutting mechanism for the pole-hole driller is the oscillating deep-kerf nozzle. The deep-kerf nozzles are used to cut a core, which is then removed by a mechanical breakout tool. The resulting hole is slightly larger than the pole so that minimum work is required to secure the pole in the ground. The conceptual design for a waterjet pole-hole driller is shown in Fig. 9.

The pole-hole driller is mounted in the rear of the tractor and can be raised and lowered during moves from placement site to placement site. When the device is located over the desired spot, it is leveled by the tractor hydraulics, and three legs are put in place to form a secure tripod base for the hole driller. Once the tripod is in place, drilling with the waterjet begins. The waterjet cuts the circumference of the hole, leaving a core, which is then removed by a special breakout tool.

The device shown in Fig. 9 has been proposed to cut the core for the pole-hole. This device has two oscillating deep-kerf nozzles to cut the kerf and has, in addition, a secondary oscillating device which slowly oscillates the deep-kerf nozzles (180 deg) so that they cover the entire circumference. This approach was decided upon instead of a swivel because the oscillating device is more reliable. If a reliable high-pressure swivel is developed, then the swivel would be an alternative to oscillation. A third motion is required to cut the core. This third motion, the downward motion of the core barrel, is achieved by a motor that raises and lowers the device with a screw device. This device can drill only one size hole; if a larger or smaller hole is desired, then a new barrel would be required.

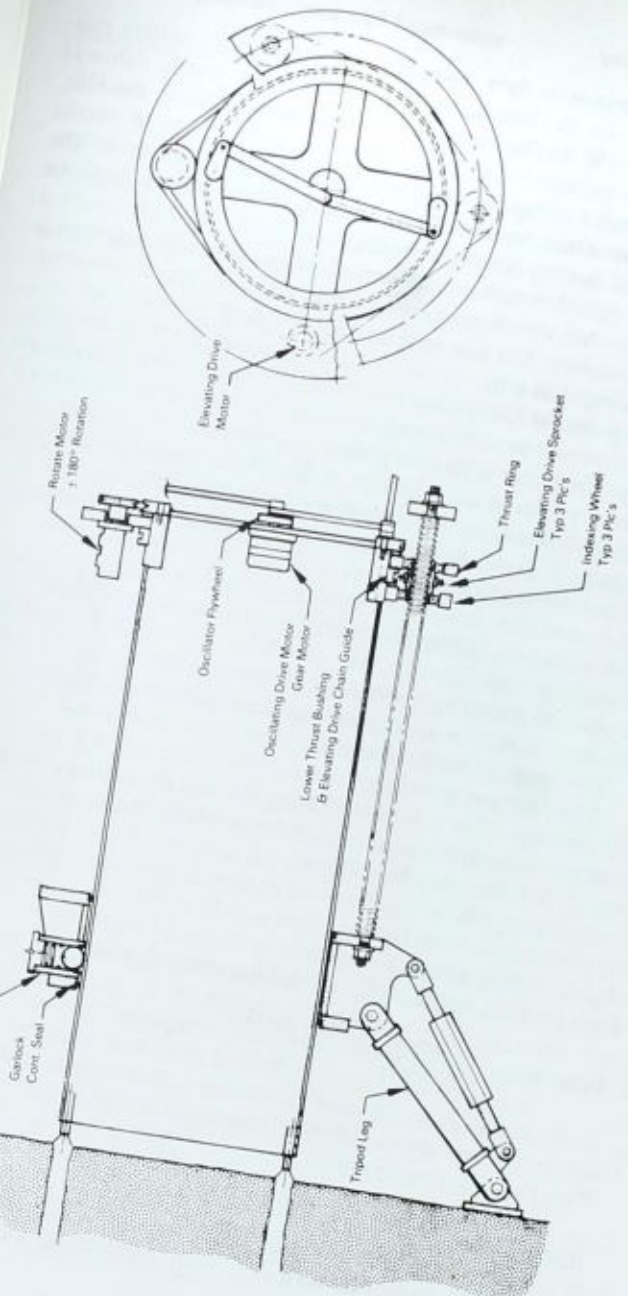


FIG. 9—Pole-hole driller schematic

Projected Cutting Rates

Based on the experimental data, rates can be predicted for cutting pole-holes and trenches. In the laboratory tests, the kerfing nozzle delivered approximately 22.5 kW to the rock. In the proposed trenching machine, 188 kW would be available to power the nozzles. If two pairs of nozzles were used, then each kerfing nozzle would have 94 kW to power it. The depth of cut is determined by direct linear scaling of the cutting data. An estimate of the field cutting rates is presented next.

Trenching—A typical trench would consist of two parallel cuts and a cross cut. Rates for two trench sizes are as follows.

1. Trench dimensions: 100 mm wide by 150 mm deep

Kerf spacing: 150 mm

2 nozzle pairs: 94 kW/pair

Nozzle traverse rate: 100 mm/s

Nozzle cutting rate: 3.75 mm/pass

Number of passes to cut: 150 mm = 40

Side cuts: 40 passes by 3 s/pass = 6.67 min/m

Cross cuts: 40 passes by 1 s/pass = 2.22 min/m

Total cutting time: 9 min/m

Advance rate: 6.67 m/h

2. Trench dimensions: 250 by 300 mm

Kerf spacing: 150 mm

Side cuts: 80 passes by 3 s/pass = 12 min/m

Cross cuts: 6 cuts/m by 80 passes by 2.5 s/pass = 20 min/m

Total cutting time: 33 min/m

Advance rate: 1.8 m/h

Pole-Hole Drilling—The pole-hole drilling consists of cutting a core of a given diameter to a specified depth. Rates for two hole diameters are

1. Diameter: 0.355 m; depth: 0.915 m

2 nozzle pairs: 94 kW/pair

Nozzle traverse rate: 100 mm/s

Nozzle cutting rate: 3.8 mm/pass

Path for each nozzle: 0.56 m (half the circumference)

$$\text{Time/hole: } \frac{560\text{mm}}{100\text{ mm/s}} \times \frac{240\text{ passes}}{60} = 22\text{ min}$$

Drill advance rate: 2.5 m/h

2. Diameter: 0.5 m; depth: 0.915 m

Path for each nozzle: 0.8 m

$$\text{Time/hole: } \frac{0.8\text{ m}}{0.100\text{ m/s}} \times \frac{240\text{ passes}}{60} = 32\text{ min}$$

Drill advance rate: 1.75 m/h

Operational Requirements and Economics

Operational Requirements

If high-pressure waterjets are to become practical construction tools for use in the field, they must be capable of meeting certain operational requirements. These requirements will of course vary with the specific application and field conditions. For example, in most of Canada and northern parts of the United States, waterjet tools should be capable of operating under winter conditions. This requirement is obviously not so important in the southern parts of the continent. Similarly, rock cutting tools may have to be capable of cutting a wide variety of rock types and strengths in some geographical locations, whereas in other locations the variation in rock properties over large areas may be relatively insignificant. Some of the more general operational requirements are as follows.

1. As a utility construction tool, the waterjet unit must be easily transportable and maneuverable.

2. Certain applications such as rock trenching, pole-hole cutting, frozen soil trenching, and guy anchor drilling will require the waterjet unit to have an all-terrain capability. This is particularly important in areas where large amounts of rural distribution systems exist.

3. The equipment must be capable of operating in all weather conditions. This implies that north of the 40 deg parallel the equipment should be operable in the temperature range of -30°C to $+35^{\circ}\text{C}$.

4. Additions to the water supply, such as deicers, must be nonpolluting.

5. The equipment must be designed so that a utility company crafts-person can operate and maintain the equipment after a nominal training period.

There are, of course, many other operational requirements specific to each application. From a utility construction viewpoint, however, one of the most important ingredients to the successful implementation of waterjet tools is public acceptance. Since utilities find themselves working virtually in the front lawns and backyards of the general public, the environmental impact of this technology is a major consideration. In fact, this aspect is deemed to be one of the major advantages of waterjet tools. Compared with jackhammers, concrete saws, and blasting, waterjet tools should create considerably less noise and air pollution. Furthermore, when used in a populated environment, waterjets impose considerably less physical danger and discomfort to the general public.

Economics

Since none of the waterjet tools described in this paper have yet been developed on a commercial basis, it is very difficult to establish a factual

economic history. The best one can do at this stage is to compare the present-day cost for various types of utility construction to the predicted or estimated cost of achieving the same end result using the appropriate waterjet concept. It is important to recognize that in this type of economic analysis the construction methods used in achieving the same goals, using conventional methods or the waterjet method, may be quite different. For example, trenching small cables in rock will normally require the excavation of a comparatively large trench using conventional blasting techniques. This is due to limitations on the smallest size of trench that can be practically blasted. Using the waterjet kerfing technique, however, allows one to cut trenches proportionate to the size of cable being placed. Therefore, although the same size of cable is placed, the total amount of rock excavated may be substantially less with the waterjet than by blasting. An economic comparison based strictly on conventional trench sizes is therefore misleading.

An analysis of rock trenching for distribution cable installations reveals that in Eastern Canada the total cost for installing small-diameter (less than 50 mm) cables is approximately \$15 to \$24 per metre. Based on the cutting rates described earlier and on the following assumptions.

1. A three-man operation—that is, one man operating the waterjet, and two men the water truck—preclean the trench, break rock kerfs, and place and backfill cables.

2. The trenching rate per hour is limited by the cutting rate of the waterjet. This means that precleaning and breaking rock kerfs can be performed while the trench is being cut.

3. The trenching rate is approximately 6 m/h; therefore, the labor cost for trenching at \$15 per man-hour is \$45 per 6 m or \$7.50 per metre. The cost of placing cable and backfill is estimated at \$4.00 per metre. Finally, the cost of moving and setting up the machine is estimated at \$0.50 per metre. This results in a total cost of approximately \$12 per metre for waterjet kerfing. For larger cables and pipes requiring larger trenches, that is, for greater than 0.05 m² in cross section, conventional blasting techniques are generally less costly than the waterjet kerfing technique. There is, however, some indication that a combination of waterjet kerfing and controlled blasting could result in a cost-effective method of creating larger trenches in rock. This technique has yet to be investigated.

The average cost for installing telephone or hydro utility poles by blasting in hard rock is \$180 per pole in Eastern Canada. In soft rock (for example, limestone, shale, sandstone), the present installation method costs approximately \$100 per pole. These costs do not include the price of the pole. The cost of installing poles in hard rock using the waterjet technique is broken down as follows.

1. Assume it is a three-man operation—that is, one man operating and cleaning the sites and two men placing and backfilling poles:

Preclean and set up	30 min
Drill 1.22 m	30 min
Excavate	15 min
Place pole and backfill	0 min
Move machine	10 min
	<hr/>
Total time per installation	85 min

2. The labor cost per installation at \$15 per man hour is

$$(3 \times 15) \times \frac{85}{60} = \$63.75$$

Operating expenses:

Gas and oil	\$ 3.50
Cost of moving machine/pole	\$ 9.50
Cost of backfill material	<u>\$12.00</u>

The total cost per installation using the waterjet is \$88.75.

These costs will of course vary across the continent. The relative cost difference between present construction methods and the waterjet methods should, however, remain approximately the same. These cost comparisons illustrate that substantial cost reductions can be achieved with high-pressure waterjet tools. What remains to be proven is the technical and practical capability of waterjet tools under field conditions.

Conclusions

The results of this research indicate the following:

1. Waterjetting technology has reached the stage where cutting various types of hard and soft rocks is a technically and economically viable application.
2. More specifically, to the utility industry, waterjetting can impact on the following applications: pole and anchor hole cutting, rock trenching, frozen ground excavation, ice cutting, and concrete cutting.
3. The use of waterjets for rock cutting applications could yield economic payoffs in the order of 20 to 50 percent over present methods.
4. Waterjets are cleaner, safer, and generally less destructive to the environment than existing rock cutting or excavating tools.
5. Waterjet systems have proven to be reliable and easy to operate in factory applications.
6. Using waterjets, the productivity rates for trenching and pole-hole cutting are an improvement over rates achieved with conventional methods.

Faint, illegible text in the upper half of the left page.

Faint, illegible text in the middle section of the left page.

Faint, illegible text in the lower half of the left page.

Summary

Faint, illegible text in the right page, appearing to be a summary or continuation of the text on the left.

Summary

The field of erosion encompasses a diversity of problem areas, and studies are initiated for a variety of reasons. The investigation of erosion phenomena has been motivated mainly by the appearance of a critical problem in a system which adversely affects the operation or minimum performance levels of that system. Excessive operating costs associated with helicopter rotor blades in sandy terrains, ingestion of particulates into gas turbines, liquid drop erosion in steam turbines, and cavitation erosion of ships' propellers have stimulated a fair amount of research into ways of reducing or eliminating the resulting erosive damage. Thus erosion of materials has not been investigated in a very organized manner. When the erosion problem becomes severe enough, something is done about it; but, once the need is satisfied or the initial requirements change, the ongoing investigations are terminated. Specialized equipment is constructed and used to get one result, then abandoned; testing programs are initiated for screening purposes, but the types of materials evaluated are far-ranging and so a coherent trend within a class of materials cannot usually be established. This lack of a continuing effort in relation to a particular erosive environment or material category has resulted in a fairly disjointed literature.

This trend is reflected in the contents of the four previous ASTM symposia on erosion [1-4].¹ The first *STP* on erosion [1] contained six papers with liquid drop, solid particle, and cavitation erosion about equally represented. The contents of the next three *STP*'s [2-4] are equally divided between papers on topics in liquid impingement and cavitation erosion. During the period covered by these three volumes (1966 to 1974), only one paper was included on solid particle erosion [5]. These observations are interesting in relation to the contents of the present *STP*, in which more than a third of the papers are devoted to solid particle erosion, followed by liquid drop erosion, with a much smaller representation of cavitation erosion investigations. The present volume also contains a significant number of papers covering waterjet technology and waterjet applications. These topics are included as constructive uses of controlled erosion damage.

Thus it would appear on the basis of this limited sampling that a de-

¹The italic numbers in brackets refer to the list of references appended to this paper.

cisive shift in the problem areas of major concern has taken place over the past few years. This is due in part to recognition and engineering experience in the magnitude of the erosion problems which will be encountered in coal conversion processes [6] and the need for improved mining procedures using liquid jets [7].

The objective of an erosion investigation is an important consideration in the research adopted and the level of effort required. For example, the erosion rates for specific materials may be needed to implement semi-empirical correlations for design purposes; screening of state-of-the-art or developmental materials or both may be required in order to select the best material for a particular application; or a material development program may be required to improve the erosion resistance of a restricted class of materials as dictated by other engineering considerations.

Material screening with respect to an erosive environment is represented in the papers by Hansen [8], Schmitt [9], and to a lesser extent in the papers by Gulden [10] and Barkalow et al [11]. Many of the general material screening programs in the past were based on the use of specialized erosion equipment which was not readily available. Therefore a considerable amount of the data generated are unique to the erosive environment utilized for the application of interest. The ASTM G-2 Committee has been active in trying to standardize the test conditions for widely used erosive devices and, when this is not possible, to at least standardize the data reporting procedure. These efforts should make the data obtained have more general utility than would otherwise be possible.

An important aspect of material screening, if it is to be reasonably independent of the laboratory conducting the tests, is characterization of the erosive environment. The paper by Maji and Sheldon [12] indicates that the initial characteristics of the solid particles used in a blast tube apparatus can be significantly modified in the apparatus itself before reaching the specimen's surface. This effect is dependent on the properties of the particles used, but it points out the need for detailed characterization of the erosive environment a specimen actually experiences even for a widely used test configuration. These effects are important with respect to establishing accurate correlations with the material properties of the material being tested.

Along these same lines one notes that there is a much stronger materials orientation represented in this volume compared with the previous volumes [1-4]. More work is devoted to examining the eroding material microscopically and to undertaking more basic investigations of the changes which occur in the material as well as identification of the microstructural features which may contribute to the onset and development of the erosion damage. The work of Ives and Ruff [13] provides understanding of the changing character of the eroding surface of copper specimens subjected to solid-particle impacts. Using metallographic procedures, they were able

to observe the role of particle embedding as a function of attack angle and length of exposure as well as the subsurface damage produced. On the basis of these observations a model is proposed to describe the embedding process. Their results emphasize the fact that the surface layer of highly ductile materials is transformed into a composite material as the erosion process proceeds, with properties which can be quite distinct from those of the initial material. The range of materials for which particle embedding is a significant effect and a quantitative evaluation of how it may influence the erosion rates for the initial target material require further investigation. The latter consideration may have important implications in attempts to correlate the measured erosion rates with the original thermomechanical properties of the target materials.

A number of conceptual models have been used as the basis for the development of analytical descriptions of erosion processes. Generally these models do not incorporate an accurate experimentally based representation of the material removal process into the analytical formulation. The mode of material removal is simply a conjecture or is not specified at all in several of these analyses. Within the past few years, however, experimental studies pertaining to erosion mechanisms have been pursued, so a better indication of what is actually responsible for material removal can be obtained. These approaches are represented in a number of the papers in this volume.

Finnie et al [14] and Hutchings [15] have provided reviews of much of the work on modeling solid-particle impact damage and the range of erosion mechanisms which have been proposed in the past. Professor Finnie's discourse on his modeling efforts over the past 20 years was a significant contribution to the symposium which was instructive to all in attendance. His perspectives are incorporated in the paper by Finnie et al [14], which explains recent extensions of his notable early contributions to the solid particle erosion literature.

Hutchings [15], on the other hand, idealizes the solid particle erosion process in a series of clever single-particle impact experiments which can be used to model the mechanics of particle impacts on metallic surfaces. This work is quite innovative in the field of solid particle erosion and a much needed new approach to advance understanding of the particle/target interactions, which are extremely difficult to identify for more conventional solid particle erosion test conditions.

Adler and Evans [16] have constructed a reasonably complete description of the impact process and the potential sources for the damage associated with hypersonic solid-particle impacts on carbon-carbon composite materials. This is the first time that a number of observations derived from microscopic examinations of the impacted specimens, high-speed photographic records of the impact event, idealized experimental conditions, and relevant analyses of the transient response of the target have been

ature erosion rate, and that the corrosive environment can also cause the results obtained are of limited interest, the scope of the investigative procedures used to obtain them is instructive as a productive methodology for wider-ranging problem areas in the field of particulate erosion.

The paper by Preece and co-workers [17] is somewhat unique in the field of cavitation erosion in that it examines the process by which material removal develops on metallographically prepared specimens of pure metals exposed to the cavitation field generated by an ultrasonic horn system. The influence of the microstructure of these metals, primarily grain size, on the material removal process is evaluated. An important conclusion from this work is that there is probably no simple correlation between bulk quasi-static mechanical properties and cavitation erosion resistance as was so often thought to be the case in the past [18]. This general conclusion—that any correlations between erosion resistance and material properties must also include the microstructural characteristics of the material and in some cases the surface condition—is becoming more widely recognized in the field of liquid drop impingement. These findings from detailed investigations of liquid drop and cavitation erosion mechanisms cast doubt on the universality of the correlations developed by Thiruvengadam [19,20] and Springer [21,22] based exclusively on mechanical properties of the material. The success of these latter approaches is that they consider a generic representation for a class of materials, emphasizing that a definite trend is established for an extensive range of materials. There are also more basic conceptual errors inherent in these correlations as pointed out by Adler [23]. Those investigators concerned with identifying actual erosion mechanisms and trying to improve the erosion resistance of a particular material are looking at a much more restrictive class of materials. The work of Preece et al is an example, among several, which demonstrates the magnitude of the change in the erosion rate which may result from modifications in the basic material. The data base is still too restricted to obtain an accurate quantitative estimate of how much the fabrication process, surface finish, microstructural features, and bulk mechanical properties can affect erosion resistance; however, the effect can be significant for both metals and nonmetals.

Relatively little of the solid particle erosion data pertain to elevated-temperature test conditions. However, the major impetus for the development of elevated temperature and corrosive environmental testing capabilities and procedures is the need for these data in the cost-effective operation of coal conversion plants [6]. The work presented by Finnie et al [14], Tabakoff and Wakeman [24] and Barkalow et al [11] is a small sampling of the work which will be appearing in these areas over the next few years. It is seen from these preliminary studies that elevated temperatures can increase the erosion rate for some metals compared with the room temper-

incorporated into a coherent picture of the crater formation process. While significant changes to occur, with the magnitude of the enhancement effect dependent on the size and properties of the erosive particles.

The addition of elevated temperatures and corrosive environments to the list of test parameters which must be considered in solid particle erosion testing expands to unmanageable proportions the screening test matrix to evaluate the effects of the test conditions on the erosion rate for a single material. Consideration should therefore be given to the information required and an organized and coordinated program should be established as soon as possible to optimize the data collection activities which may be required [6]. There are several functions the ASTM G-2 Committee can provide for this purpose: round-robin testing for evaluating the variability in test results due to the test procedures in different laboratories and for developing a broader data base than otherwise would be possible; standardization of the test reporting procedures for enhanced data interchange; and establishment of study groups to resolve general issues concerning a range of erosion/corrosion problem areas and to serve as a focal point for interaction among active workers in various erosion-related fields. Moreover, the magnitude of the erosion/corrosive conditions which may have to be considered warrants support for more detailed materials-oriented investigations for the purpose of identifying the commonality of erosion mechanisms and dominant material properties influencing the erosion rates. These investigations should provide guidance for the development of materials with improved erosion resistance and contribute to limiting the scope of the test evaluation required.

The work of Menguturk and Sverdrup [25] illustrates the steps required to use erosion (and ultimately erosion/corrosion) data for practical applications. A number of questionable assumptions are made in their analysis of particulate erosion of the blading in a gas turbine, however, in going through the available flow analyses and incorporating the available erosion data, although not completely relevant, they have demonstrated the weaknesses in the existing erosion data base. This paper represents an example of how much of the work contained in the other papers on solid particle erosion in this *STP* will be utilized and provides some idea of the directions for improving the form these data must have to be useful for design purposes.

The water drop impact damage modeling carried out by Rosenblatt et al [26] raises several interesting issues. For example, how well are the material properties controlling liquid impact damage in the subsonic regime represented in these computations? How much can be learned from a computer modeling effort of this type for improving the erosion resistance of a specific material, such as zinc selenide? Is the cost of these computations, which increases as more of the microstructural features of the material are in-

cluded in the computer model, justified in comparison with a more direct materials-oriented approach?

Numerical analyses of particle impact have been extensively developed for the hypersonic velocity regime where a hydrodynamic response of the material is assumed. A strong interaction between the impacting particle and penetration of the target material takes place; the final crater dimensions are to be determined. At subsonic impact velocities the water drop is much less damaging and subtle changes occur within the target material governed to a large extent by its microstructure and defects in its microstructure. Computational representations for a polycrystalline target material with an average grain size on the order of to two orders of magnitude less than the drop diameter become exceedingly complex if they are to simulate the microstructural features of the target, such as textural variations, solid inclusions, grain orientations, and grain boundary strengths. One therefore questions if the investigation of the contribution of these features to damage initiation can be more productively accomplished by well-conceived experiments and detailed materials characterization. Rosenblatt and co-workers have made a significant contribution to the evaluation of the spatial and temporal distributions of pressure for a water drop impacting rigid or elastically deformable surfaces at subsonic velocities. This pressure distribution, as described in their paper [26], can be used to provide some idea of the temporal development of the stresses in a homogeneous and isotropic elastic body as a guide in identifying those regions within the target where critical stress conditions are likely to occur; however, caution is advised in going beyond this basic model in that the novelty of the explicit computational results may overshadow the physical aspects of the actual fracture initiation and propagation process. Numerous computations can be made, but these have to be balanced against the real extent to which the numerical results contribute to improvement of the erosion resistance for a particular material.

The foregoing perspective on the role of finite-difference models in subsonic water drop impact damage would not be necessary if Rosenblatt et al [26] did not stipulate that one objective of their work is to identify the mechanisms responsible for internal crack formation and propagation in infrared windows subjected to *subsonic rain erosion*. However, there is nothing in the paper which is directed toward this objective. The relevance of a numerical analysis is to describe and provide quantitative data for a physically observed mechanism. A considerably more detailed computational model would be required before a crack formation mechanism could be *identified* in zinc selenide via a numerical simulation. The authors have not identified any mechanisms but have assumed a particular model and a critical crack length for their computer analysis of the damage due to a single water drop impacting a zinc selenide target. Once the model is accepted, then the sensitivity of the fracture response

can be computed in terms of the relatively few material parameters and the impact parameters entering the numerical analysis.

It is difficult to rectify on physical grounds the nature of the crack patterns shown in Fig. 19 and 22 of Ref 26, especially Fig. 22. (A question about this was raised by N. MacMillan (p. 000) and does not appear to have been adequately addressed by the authors.) The cracks produced in a real material would be discrete with a quantity of undamaged material separating these cracks. The numerical results imply that a large quantity of material would be highly fragmented and would in essence be free to fall loose from the specimen. This does not seem to be the case for actual drop impacts at velocities below 342 m/s (1120 ft/s). The manner in which the failure criteria are introduced in the numerical computations and the way in which the stress is redistributed in the computer code once a cell is fractured appear questionable. The cell size may be too large for the fracture response which is to be described. Therefore the stated fracture trends for the grain size and flaw size variations have no significance until the fracture patterns can be properly interpreted.

Furthermore, the final crack formations are on a scale such that comparisons with experimental data are almost meaningless. The authors have been adjusting their results to compare with experimentally observed fracture patterns as they become available [27]. In essence, they are simply describing general observations and not providing directions for optimization of material properties for increased erosion resistance. Modeling the dynamic fracture response of a polycrystalline material and the onset of fracture in homogeneous brittle materials due to water drop impingement are complex problems if the computational models are to reflect a realistic picture of the material and its surface condition [28,29].

There are many aspects to erosion modeling. The most prominent is the development of a predictive model. A predictive model provides the capability to prescribe the rate of material removal from a particular material exposed to a specified erosive environment. Although several examples of semi-empirical correlations can be found in the literature [14,15] and several attempts to derive definitive predictive models can be cited [30,31], it seems doubtful that a definitive predictive model will be forthcoming in the near future. A predictive model implies that the erosion rates can be determined entirely from data independent of erosion test data. All the models proposed for this purpose invoke empirical correlations at some point in their implementation. However, computer simulations (models) can be helpful in obtaining quantitative information on various aspects of the material removal process in all fields of erosion. In contrast to the approach of Rosenblatt et al [26], the computer analyses should be formulated on the basis of materials-oriented models which characterize the dominant failure modes that can occur in a particular material or class of

materials [30,31]. With more investigators examining erosion damage on a microscopic scale, there is excellent potential for developing physically realistic computer analyses for small portions of the general erosion process.

The papers herein pertaining to waterjets are concerned with concepts to improve their cutting or fragmentation capability [32-34] and with some of the applications for waterjets [35-37]. At the present time there is considerable emphasis on the development of systems for particular areas of application. The general approach is thus the reverse of that described in relation to particulate and cavitation erosion, where the response of the material and ways to improve its erosion resistance are of prime concern, since it is now the creation of a more effective erosive environment which is the major consideration. There is considerable breadth exhibited in the innovative systems for enhancing, concentrating, or pulsating a jet. However, the measure of its effectiveness is typically evaluated in terms of its gross cutting rate. To date, there does not appear to be any concentration of effort on just what is happening to the material as the jet penetrates or cuts it. Detailed investigations of the jet/material interaction should certainly contribute to customizing or selecting the jet configuration which would be most efficient for a particular material. Some initial evaluations along these lines were described by Vijay and Brierly [38].

There is a problem, however, in comparing one waterjet system with another in that criteria must be established which are acceptable to most workers in the field for making such a comparison. The ASTM G2 Committee is presently addressing this critical issue. A second area under consideration is the selection of standardized materials for specifying cutting rates.

In summary, there are several areas of erosion receiving attention at the present time which represent a change in emphasis from the recent past based on the contributions to this publication. The areas of current interest are solid particle erosion at ambient and elevated temperatures and in corrosive environments for metals and ceramics, limited applications of liquid drop impingement primarily for nonmetallic materials for high-speed aircraft and coupled erosion/ablation of reentry vehicles, with relatively little activity in cavitation erosion. The background of an increasing number of contributors to the erosion literature is in metallurgy or materials science, so basic materials investigations of erosion are becoming more prevalent. The identification of the damage modes in real materials coupled with accurate representations of the mechanics of the erosion process should be productive in advancing basic understanding of the of the erosion of materials. This general level of activity in several erosion problem areas (different from the past) is once again becoming substantial, so the prospects for many important advances in combating the erosion process in certain material systems and for the development of improved

erosion-resistant materials are most encouraging. It is hoped these new investigations will be undertaken in a more organized manner than in the past.

Waterjet technology is increasing at a rapid pace to meet the demands in the growing number of application areas for waterjets, although a sizable portion of the current support is connected with mining operations. Considerable emphasis is being placed on the development of more efficient waterjet systems; however, it is envisioned that once optimization of the general system parameters has been achieved, the material damage mechanisms will be considered in more depth to determine additional directions for improving jet operating efficiencies. The erosion process due to cavitating fields and water drop impingement may be helpful in understanding the damage produced in the material by various waterjet systems.

W. F. Adler

Effects Technology, Inc., Santa Barbara,
Calif. 93111; editor.

References

- [1] *Symposium on Erosion and Cavitation, ASTM STP 307*, American Society for Testing and Materials, 1962.
- [2] *Erosion by Cavitation on Impingement, ASTM STP 408*, American Society for Testing and Materials, 1967.
- [3] *Characterization and Determination of Erosion Resistance, ASTM STP 474*, American Society for Testing and Materials, 1970.
- [4] *Erosion, Wear, and Interfaces with Corrosion, ASTM STP 567*, American Society for Testing and Materials, 1974.
- [5] Adler, W. F. in *Erosion, Wear, and Interfaces with Corrosion, ASTM STP 567*, American Society for Testing and Materials, 1974, pp. 294-315.
- [6] *Erosion Control in Energy Systems*, Publication NMAB-334, National Materials Advisory Board, Washington, D.C., 1977.
- [7] Frank, J. N., "An Overview of the U.S. Bureau of Mines Hydraulic Mining Program," presented at the ASTM Symposium on Erosion: Prevention and Useful Applications, American Society for Testing and Materials, Vail, Colo., Oct. 1977.
- [8] Hansen, J. S., this publication, pp. 148-162.
- [9] Schmitt, G. F., Jr., this publication, pp. 376-405.
- [10] Gulden, M. E., this publication, pp. 101-122.
- [11] Barkalow, R. H., Goebel, J. A., and Pettit, F. S., this publication, pp. 163-191.
- [12] Maji, J. and Sheldon, G. L., this publication, pp. 136-147.
- [13] Ives, L. K. and Ruff, A. W., this publication, pp. 5-35.
- [14] Finnie, I., Levy, A., and McFadden, D. H., this publication, pp. 36-58.
- [15] Hutchings, I. M., this publication, pp. 59-76.
- [16] Adler, W. F. and Evans, A. G., this publication, pp. 345-375.
- [17] Preece, C. M., Vaidya, S., and Dakshinamoorthy, S., this publication, pp. 409-433.
- [18] Garcia, R., Hammit, F. G., and Nystrom, R. E. in *Erosion by Cavitation or Impingement, ASTM STP 408*, American Society of for Testing and Materials, 1967, pp. 239-283.
- [19] Thiruvengadam, A., in *Proceedings, Third International Conference on Rain Erosion and Associated Phenomena*, A. A. Fyall and R. B. King, Eds., published by the Royal Aircraft Establishment, England, 1967.
- [20] Thiruvengadam, A., Rudy, S. L., and Gunasekaran, M. in *Characterization and*

- Determination of Erosion Resistance. ASTM STP 474*, American Society for Testing and Materials, 1970, pp. 249-287.
- [21] Springer, G. S. and Baxi, C. B. in *Erosion, Wear, and Interfaces with Solids. ASTM STP 567*, American Society for Testing and Materials, 1974, pp. 10-15.
- [22] Springer, G. S., *Erosion by Liquid Impact*, Scripta Publishing Co., Washington, 1976.
- [23] Adler, W. F., "The Mechanics of Liquid Impact," to be published in *Materials Science and Technology*.
- [24] Tabakoff, W. and Wakeman, T., this publication, pp. 123-135.
- [25] Menguturk, M. and Sverdrup, E. F., this publication, pp. 193-212.
- [26] Rosenblatt, M., Ito, Y. M., Eggum, G. E., this publication, pp. 227-254.
- [27] Hackworth, J. V., Kocher, L. H., and Snell, I. C., this publication, pp. 255-270.
- [28] Adler, W. F. and Hooker, S. V., *Wear*, Vol. 48, 1978, pp. 103-119.
- [29] Adler, W. F. and Hooker, S. V., *Wear*, Vol. 50, 1978, pp. 11-38.
- [30] Adler, W. F., *Wear*, Vol. 37, 1976, pp. 345-352.
- [31] Adler, W. F., *Wear*, Vol. 37, 1976, pp. 353-365.
- [32] Eddingfield, D. L. and Albrecht, M., this publication, pp. 461-472.
- [33] Mazurkiewicz, M., Barker, C. R., and Summers, D. A., this publication, pp. 473-492.
- [34] Selberg, B. R. and Barker, C. R., this publication, pp. 493-511.
- [35] Conn, A. F. and Rudy, S. L., this publication, pp. 562-581.
- [36] Hilaris, J. A. and Labus, T. J., this publication, pp. 582-596.
- [37] Huszarik, F. A., Reichman, J. M., Cheung, J. B., this publication, pp. 597-616.
- [38] Vijay, M. M. and Brierley, W. H., this publication, pp. 512-529.

Index

A

- Ablation, 392, 400
- Ablation-erosion, 400
- Abrasion test, 38
- Acoustic impedance, 104, 117, 228, 250
 - Mismatch, 294

C

Carbon-carbon composites

- Cracks, 363
- Density, 347, 390
- Fiber bundle, 387
 - Dimensions, 347, 369, 386, 390
 - Kinking, 350, 351, 354, 355, 357, 361, 372, 373
 - Critical shear stress, 374
 - Density, 357
 - Matrix interface, 357, 363, 370
 - Volume fraction, 393-395
- Interfiber shear, 369
- Lateral fiber bundles, 348
 - Flexure, 369
 - Kinking, 355, 357, 367
 - Tension, 369
 - Transverse shear, 369
- Longitudinal fiber bundles
 - Flexure, 369
 - Fragmentation, 368
 - Kinking, 355, 357, 368-370
 - Tension, 369

- Transverse shear, 369
- Matrix pockets, 356, 369
- Particle impact
 - Crater dimensions, 368
 - Cratering process, 346, 351, 362, 365 ff., 621
 - Erosion resistance, 368, 392
 - Mass loss, 346, 351, 385, 387, 389, 392-397, 399
 - Material ranking, 385, 386, 389, 391, 395, 398, 405
 - Material removal process, 346, 368, 374
 - Material removal rate, 381, 383-386, 389, 391, 392, 399, 405
 - Pressure, 363
 - Porosity, 363, 369
 - Processing, 394, 400
 - Chemical vapor deposition, 392, 396
 - Graphitization temperature, 396
 - Impregnation cycles, 396
 - Matrix materials, 392
 - Unit cell, 347, 386, 392, 393, 400
 - Weave, 347, 383, 384, 387, 390, 394, 400
- Cavitation, 435
 - Back pressure, 530, 532, 540, 545
 - Bubbles, 431, 432, 513, 515, 525
 - Cloud, 432, 448
 - Dynamic stresses, 410
 - Flow velocity, 530-532

- Intensity, 454, 531, 535
 Number, 530-532, 535-538, 544-546
 Pressure, 530, 535, 536, 541
 Vapor, 532
 Cavitation erosion, 531, 541, 548, 562, 569, 622, 625
 Component lifetime, 409
 Mass loss, 454
 Acceleration period, 435, 448, 450, 454
 Attenuation period, 435, 448, 450, 454
 Incubation period, 411, 421, 424, 427, 435, 436, 439, 448, 450, 454
 Steady-state period, 435, 448, 450, 454
 Mechanisms, 410, 411, 418, 419, 422, 423, 427, 429, 435
 Rate, 410, 419, 429, 447, 535-537, 540
 Temperature dependence, 535
 Cavitation erosion resistance, 530, 544
 Armco iron, 437
 Body-centered cubic metals, 415 ff., 429
 Evaluation, 434, 435
 Face-centered cubic metals, 411 ff., 429, 430
 Hexagonal close-packed metals, 421 ff., 429, 430
 Mechanical property correlations, 409, 410, 430, 435, 622
 Mild steel, 437
 Nodular graphite cast iron, 437
 Cavitation erosion testing, 530, 544, 546
 Cavitating waterjet device, 532, 534, 541, 454, 546
 Erosion pattern, 536
 Magnetostrictive vibratory horn, 410, 434, 443-445, 447, 454-456, 530, 535, 541, 622
 Elevated temperature, 447
 Vibration amplitude, 447, 449-451
 Vibration frequency, 444, 445, 450, 454
 Rotating disk, 530
 Venturi, 530, 544
 Water tunnel, 436, 443, 444, 451, 454, 530, 544
 Cleaning, 536, 582 ff., 595, 600
 Coal conversion, 34, 36, 52, 54, 148, 149, 156, 157, 163, 165, 190, 191, 194, 218, 219
 Column buckling, 372, 373
 Corrosion (*see also* Oxidation), 49, 52, 162, 182, 449, 450, 454, 458
 Hot, 163, 164, 166, 189, 191
 Protective scales, 164, 166, 167, 170, 171, 173, 174, 188-190
 Scale removal, 165
 Test, 52, 55
 Crack (*see also* Fracture), 282, 288
 Blunting, 119
 Circumferential, 326, 330
 Configuration, 244, 246
 Flaw size, 113-115, 117, 228, 244, 246, 315, 624
 Distribution, 115, 117, 121, 246, 249
 Glass, 79, 80
 Weibull distribution, 85, 117, 118
 Intersection, 37
 Lateral, 109, 118, 120
 Nucleation, 227, 228, 280, 422, 424, 429, 623
 Pattern, 228, 246-249, 251-253, 624
 Propagation, 37, 227, 228, 280, 422, 623

- Radial, 109, 112, 116, 118, 120
 Subsurface, 57
 Tension, 228, 235, 236, 246, 250
 Velocity, 316
- Crater
 Cavitation erosion, 411
 Liquid impact, 309
 Solid particle impact, 12, 15, 25, 39, 42, 62-65, 67-71, 73, 145, 173, 189, 349 ff.
 Waterjet erosion, 515-519
- Cratering process, 346, 621
 In carbon-carbon composites, 349, 351, 362
 Penetration phase, 365, 367, 369, 370, 374
- Crystalline solid
 Body-centered cubic metals, 415
 Twin boundaries, 418, 429
 Twinning, 418
 Strain-rate sensitivity, 415
 Deformation twins, 22, 25, 29, 429
 Dislocations, 22, 24, 29, 413
 Barriers, 415, 433
 Cell structure, 24
 Concentration, 29
 Density, 22, 24, 25, 30
 Distribution, 24
 Generation, 25, 109
 Motion, 24, 25, 421, 430
 Network, 57
 Pile up, 413, 415
 Source, 415
 Type, 24
- Face-centered cubic metals, 411
- Grain
 Aspect ratio, 427
 Boundary, 119, 411, 413, 418, 419, 421, 422, 424, 429, 432
 Boundary triple points, 113, 422
 Deformed, 29
 Orientation, 411, 422
 Size, 7, 108, 115, 228, 244, 286-288, 295, 410, 411, 413, 415, 419, 421, 424, 427, 429, 430, 432, 622
- Linear intercept determination, 79, 86
- Structure, 28, 294
- Guinier-Preston zone precipitates, 49
- Hexagonal close-packed metals, 421
 Slip density, 422
 Twin density, 422
 Twinning, 427, 529, 432, 433
- Slip, 24, 109, 413, 421, 427, 432
 Band, 244
 Density, 422
- Stacking fault energy, 24, 413, 432
- Structure, 411, 430, 443
- Twinning, 418, 427, 429, 432, 433
 Band, 244
 Boundary, 418, 429
 Deformation, 22, 25, 29
 Density, 422
- Cutting, 300, 473, 474, 480, 490, 513, 544, 553, 554, 562, 563, 568 ff., 586 ff., 592 ff., 599, 600, 613-615
- ## D
- Deformation (*see also* Target material deformation)
 Elastic, 204
 Elastic-plastic, 86, 87, 99, 102
 Plastic, 72, 89, 109, 113, 118, 119, 122, 204, 322-324, 326, 333, 337, 429, 436, 438, 439, 445, 452, 554
 Shear, 29, 72, 323
- Degraded strength measurement
 Hydraulic device, 299, 315, 317
 Residual strength, 310 ff.

- Calcium aluminate glass, 314, 315
 - Soda lime glass, 312, 313
 - Silicon nitride, 314, 315
 - Drag bit
 - Cutting process, 556, 560, 561
 - Penetrating force, 554, 561
- E**
- Electron channeling, 21, 24, 25
 - Electron diffraction, 25, 28
 - Energy consumption, 579
 - Erosion-corrosion, 50, 52, 163, 165, 167, 185, 188, 622, 623, 625
 - Exploding foil particle acceleration, 348, 398
- F**
- Fiber reinforced composites, 320, 321, 326-339
 - Fluid dynamics
 - Bernoulli's equation, 495
 - Conservation of energy, 474
 - Conservation of mass, 474, 476, 496
 - Conservation of momentum, 474, 476, 496
 - Equations of motion, 462
 - Fluid density, 532
 - Helmholtz instabilities, 471, 498, 506
 - Shear gradient, 471
 - Stagnation pressure, 321, 471, 497
 - Stoke's law, 195
 - Turbulent jets, theory, 494
 - Fluid flow
 - Boundary layer, 134, 170, 183, 185, 204, 221, 462, 495, 503
 - Laminar to turbulent transition, 34
 - Separation, 506
 - Turbulent, 134
 - Choked, 471, 531
 - Laminar, 134, 476, 494
 - Pipe, 495
 - Reynold's number, 34, 195, 196, 495
 - Separated, 531
 - Turbulent, 134
 - Fluctuations, 470
- Fracture (*see also* Crack)
- Antireflectant coatings, 290
 - Auerbach's law, 86, 87, 95, 97-99
 - Brittle, 78, 89, 204, 415, 422, 429, 430, 437, 442, 445, 447, 448
 - Cleavage, 288, 419, 421, 458
 - Conchoidal, 316
 - Critical stress intensity factor, 86, 104, 113, 115, 117, 119, 120, 316, 329
 - Ductile, 50, 411, 413, 429, 439, 445, 447, 448, 458
 - Ductile to brittle transition, 418, 422, 427, 439, 443, 451, 454, 458
- Hertzian
- Ring, 79, 85, 87, 89, 102, 113, 117, 118, 120, 282, 286, 288, 290, 324, 340, 373
 - Test, 79, 86, 95
- Intergranular, 286
 - Microfracture, 324
 - Pattern, 109
 - Rock, 554-557, 561
 - Strength, 72, 74, 105, 113, 115, 116, 121, 122, 293
 - Dynamic, 74, 86
 - Elevated temperature, 50
 - Tensile, 324, 356

- Stress, 280, 293
 - Test
 - Four-point bend, 85
 - Tension, 55
 - Three-point bend, 85, 105, 113
 - Toughness, 86, 104, 113, 115, 117, 119, 120, 316, 329
 - Transgranular, 286-288
 - Zinc sulfide layers, 293
 - Fragmentation, 563
 - Friction, 64, 76
- G**
- Gas turbines, 34, 38, 102, 122-125, 135, 163-165, 167, 190, 191, 193, 194, 198, 200, 209, 218-221
- H**
- Hardness, 24, 65, 71, 86, 103, 117-120
 - Brinell, 143, 515
 - Indentation, 32, 86, 102
 - Knoop, 257
 - Rockwell, 140, 514
 - Test, 63, 72
 - Vicker's 38, 39, 47-50, 60, 104, 437-439, 443
 - High-speed photography, 60-62, 130-134, 137, 198, 299, 302, 305-307, 316, 321, 324, 334, 341, 346, 361, 366, 554
 - Hugoniot
 - Equations of state, 364, 374, 375
 - Pressure (*see also* Waterhammer pressure), 231, 233, 248, 321, 363
- I**
- Indentation evaluations, 554-556, 558, 560, 561
 - Infrared transparent materials, 102, 255, 623
 - Antireflection coatings, 280, 288, 290
 - Gallium arsenide, 262 ff., 280, 281, 289
 - Zinc selenide, 262 ff., 280, 281
 - Zinc sulfide, 262 ff., 280-286
 - Infrared microscopy, 288
- M**
- Material properties
 - Acoustic impedance, 104, 117, 257
 - Bulk modulus, 71
 - Coefficient of thermal expansion, 71, 156, 294, 296
 - Coefficient of friction, 64
 - Density, 71, 107, 119, 157, 257
 - Enthalpy of melting, 71
 - Fracture toughness, 86, 104, 113, 115, 117, 119, 120
 - Hardness, 65, 71, 86, 103, 117-120
 - Homologous temperature, 50, 53, 54
 - Index of reflection, 288
 - Interatomic bond energy, 71
 - Molecular weight, 71
 - Poisson's ratio, 257, 315, 323
 - Porosity, 107, 109, 112, 119, 154, 363, 369
 - Specific heat, 71
 - Strength, 50, 72, 74, 105, 113, 115, 116, 121, 122, 257, 265, 275, 536
 - Thermal conductivity, 71
 - Yield stress, 48, 49, 324
 - Young's modulus, 71, 86, 103, 104, 117, 257, 294, 315
 - Material property measurements
 - Fracture
 - Four-point bend test, 85
 - Three-point bend test, 85, 105, 113

- Hardness test, 65, 72
 Temperature, infrared pyrometer, 150
 Tension test, 55
 Mean depth of erosion, 536
 Mean depth of penetration rate, 381, 383-386, 389, 391, 392, 405
- Metals**
 Cold-working, 48, 49, 410
 Heat-treatment, 48, 49, 410
 Strain hardening, 48, 49, 438, 443, 451
- Microscopy**
 Infrared, 288
 Optical, 79, 105, 282, 525
 Optical, 79, 105, 282, 525
 Scanning electron, 6, 8, 11, 15-18, 29-31, 33, 34, 42, 48, 50, 60, 68-70, 79, 81, 89-91, 94, 105, 110-112, 122, 137, 143, 167, 173, 174, 180, 348, 411, 427, 436, 442, 447, 499, 503, 558
 Transmission electron, 6, 8, 11, 22-27, 29, 33, 105, 427
- Mining operations, 300, 317, 461, 490, 512, 553, 562, 563, 578, 579, 626
- Monroe jet, 304, 386
- N**
- Nozzle**
 Air-injected shroud, 463, 464, 470, 471
 Air velocity, 463, 467
 Aspirating shroud, 467, 471
 Convergent-divergent, 472
 Design, 461
 Diameter, 462, 532, 535, 545, 568, 569, 571, 577, 579, 581, 583, 588
 Discharge coefficient, 513, 532
 Dual-orifice, 494, 498, 499, 510
 Multiple-orifice, 494
 Nonpenetrating, 583, 593, 596
 Number, 568
 Oscillating, 601, 605, 607
 Oscillating-deep kerf, 605, 607, 610
 Penetrating, 593
 Pressure, 473, 569, 571, 583
 Rectangular slit, 584
 Rotating, 599, 601
 Shape, 462
 Supercavitating, 531
 Supersonic, 472
 Surface erosion, 498
 Surface finish, 499, 503, 506, 509, 511
 Type, 568
- O**
- Oxidation (*see also* Corrosion), 50, 52, 164-167, 171, 174, 180, 187, 191, 219
 Erosion, 170-172, 174, 176, 179, 180, 185, 187, 189, 191
- P**
- Photography (*see* High-speed photography)
 Plastic deformation (*see* Deformation)
 Plasticity
 Flow, 25, 415, 424
 Flow pressure, 37, 40, 48, 55, 57, 64, 70
 Flow stress, 24, 48, 178
 Slip line analysis, 75, 76
 Pressure transducer, 310, 317, 496, 497
 Profilometer trace, 43-46, 307, 309, 324

R

- Radome, 102, 298, 392
- Rain erosion
- Anti-reflection coating, 288, 290-292
 - Carbon-carbon composites, 346, 385-387, 389, 392-397, 399, 405
 - Gallium arsenide, 262, 263, 269, 271, 275, 276, 278, 280-281, 289
 - Graphite, 389, 391
 - Infrared transmission loss, 262, 263, 276, 279, 280, 292, 293
 - Layered window constructions, 280, 296
 - Mean depth of penetration rate, 381, 383-386, 389, 391, 392, 405
 - Zinc selenide, 262, 263, 269, 271, 275, 276, 278, 280, 281
 - Zinc sulfide, 262, 263, 269, 271, 275, 276, 278, 280-286
- Rainfield characterization parameters, 381, 382, 385, 399
- Reentry vehicle nosetips, 345, 385-387, 389, 392, 400
- Rock fracture, 555, 557
- Indentation, 555-557
 - Mechanism, 554, 561
 - Spallation, 554
- S**
- Screening tests
- Cavitation erosion damage, 434
 - Multiple water drop impact, 395
 - Waterjet impact, 338
- Shear, 370
- Adiabatic, 373
 - Band, 72
 - Deformation, 29, 72, 323
 - Stress, 324
 - Transverse, 367
- Shock waves, 365, 367, 369, 373, 374, 386
- Air, 303, 322
 - Elastic precursor, 366, 374
- Hugoniot
- Equations of state, 364, 374, 375
 - Pressure, 231, 233, 248, 321
- Impedance, 322
- Pressure, 258, 432
- Rarefaction, 366, 367
- Reflection, 366
- Release wave for liquid impact, 321, 341
- Water, 321
- Single solid particle impact, 6, 12, 60, 103, 105, 112, 113, 120, 621
- Contact area, 117-119
- Crater, 42, 69, 110, 111, 120, 173, 189, 349 ff.
- Energy loss, 65, 67, 71
 - Formation, 12, 145
 - Lip, 15, 25, 39, 43, 62, 67, 71, 73, 173
 - Profile, 43-47, 60, 76, 341
 - Volume, 62-65, 67-71
- Elevated temperature, 346, 351, 357, 384
- Energy balance, 39, 83
- Equations of motion, 39, 64, 70
- Numerical computations, 64, 66, 138, 361, 373
- Exploding foil particle accelerator, 348, 398
- Fracture during target penetration, 366
- Gas gun accelerator, 60
- Hertzian analysis
- Contact radius, 108, 109
- Indentation, 15, 22, 38, 62, 63
- Mass loss, 346, 351

- Material crushing, 109, 366, 367
- Material ejection, 348, 361, 366, 368, 370
- Material ranking, 398, 405
- Material removal, 14, 22, 67, 72, 102, 349-357, 374
- Models, 5, 37, 57, 70, 83, 98, 102, 105, 117-119, 124, 136, 176, 179, 192, 194, 204, 206, 210, 212, 621
- Particle-target interaction, 366-368, 374, 375
- Plastic flow, 15, 24, 25, 37, 40, 48, 55, 57, 64, 70, 178
- Subsurface damage, 21, 24, 341-348
- Testing, 346
- Theory, 63-67, 70, 164
- Velocity, 346, 356
- Volume removal, 37, 38, 40-42, 49, 50, 83, 86, 106-108, 112, 119
- Single water drop impact
 - Analytical loading model, 235
 - Contact area, 236, 250
 - Contact radius, 232-235, 248, 250
 - Contact velocity, 232-234
 - Damage on gallium arsenide, 259, 260, 275, 277
 - Damage on polymethylmethacrylate, 259, 260
 - Damage on zinc selenide, 259-262, 275, 276
 - Damage on zinc sulfide, 259-262, 275, 276
 - Dynamic stresses in target, 236, 241-245, 256, 258, 265, 268, 271-278, 293, 294
 - Finite difference computations, 623, 624
 - Crack patterns in zinc selenide, 244, 246-254
 - Elastic half-space, 235 ff.
 - Rigid half-space, 229 ff., 250
 - Fracture, 259-268, 275-278
 - Gas gun/suspended drop arrangement, 299, 316, 321, 341
 - Lateral outflow jetting, 322, 324-326, 330, 340, 341
 - Rotating arm, 257-259
 - Waterjet simulation, 299, 305, 309, 316, 320, 340
 - Apparatus, 300 ff., 321
 - Basis for comparison, 306-310
 - Damage on epoxy, 325
 - Damage on polycarbonate, 322 ff.
 - Damage on polyester, 325
 - Damage on polyethersulfone, 324
 - Damage on polymethylmethacrylate, 306 ff.
 - Damage on reinforced polymers, 326 ff.
 - Jet characterization, 302-306
 - Stress wave generation, 303
 - Velocity, 227, 228, 256, 258, 271
- Slot cutting
 - Coal, 568, 569, 571, 573, 575-577, 579
 - Kerf, 572, 593, 599, 601, 605, 610, 612, 614
- Solid particle erosion (*see also* Single solid particle impact, Solid particle impacts)
 - Brittle materials, 37, 78, 83, 101 ff., 204, 205
 - Brittle (deformation) mode, 6, 7, 37, 38, 78, 136, 164, 178, 194, 205-210
 - Brittle to ductile transition, 80
 - Coatings, 156
 - Corrosion, 6, 50, 52, 163, 165, 167, 185, 188, 622, 623, 625
 - Elevated temperature, 52
 - Test, 55
 - Damage enhancement, 346, 351

- Deposition, 12, 122, 185, 187, 194, 195, 212
- Ductile materials, 48, 52, 59, 71, 72, 74, 78, 122, 204
- Ductile (cutting) mode, 6, 7, 15, 29, 37, 78, 136, 164, 178, 181, 188, 194, 205-210
- Elevated temperature, 6, 50-55, 57, 122, 153, 164, 622
- Erosion rate (*see also* Particle velocity dependence, this heading), 6, 8, 41, 70, 78, 80, 120, 136, 139-144, 147, 170, 179, 181, 189, 192, 209, 213-217, 220-221
- Erosion resistance, 49, 72, 74, 117, 189, 194
- Material screening, 149, 152 ff., 620, 623
- Relative erosion factor,
 - Cemented carbides, 155, 157-160
 - Ceramics, 154, 157-160
 - Coatings, 160-161
 - Definition, 152
 - Metals, 153, 157-160
- Exposure time, 78-80, 83, 89, 95, 99, 149, 156, 167, 181
- Finnie's model for ductile metals, 5, 7, 57, 70, 176, 179, 192, 621
- Hot corrosion, 163, 165, 185-187, 191
- Protective coatings, 164, 165
- Impingement angle dependence, 53-55, 57-59, 71, 78-80, 82, 98, 179-181, 183, 184, 189
- Mass loss, 11, 71, 74, 79, 80, 89, 105, 106, 113, 140, 171, 172, 191, 204
- Incubation period, 10, 11, 15, 19, 42
- Steady-state period, 11, 14, 15, 19, 24, 30
- Material ranking, 405
- Mechanisms, 6, 37, 38, 57, 59, 60, 67, 78, 86, 89, 105, 107, 108, 121, 143, 180, 623
- Adiabatic shear, 39, 71, 72
- Brittle crack intersection, 83, 89, 164
- Delamination of surface material, 49, 50
- Grain ejection, 113, 156
- Low-cycle fatigue, 49, 50
- Metal cutting analogy, 40, 49, 53, 70, 164, 173, 176, 178, 180, 189
- Particle fracture and fragmentation, 49, 50, 137, 140
- Surface extrusion, 49, 50
- Thermal pressure, 71
- Work-hardening and embrittlement, 49, 50
- Natural dust environments, 102, 117, 120-123
- Oxidation, 170-172, 174, 176, 179, 180, 185, 187, 189, 191
- Particle mass dependence, 106, 119
- Particle size dependence, 55, 78, 79, 83, 98, 99, 106-108, 113, 185
- Size effect, 38, 42, 74, 80, 117, 118, 120
- Particle velocity dependence, 55, 58, 63, 78-80, 83, 84, 89, 95, 98, 106-108, 113, 119
- Power law relationship, 8, 10, 78, 83, 120
- Velocity exponent, 42, 58, 65, 67, 78, 83, 85, 88, 89, 99, 106, 117, 118, 120, 138, 140-142, 146, 147, 210

Problem areas

- Bearings, 102
- Coal conversion
 - Fluidized bed coal combustion, 34, 163, 165, 190, 191, 194
 - Gassifier cyclone, 218, 219
 - Lockhoppers, 148
 - Valves, 148, 149, 156, 157
- Coal-fired boilers, 123
- Coal hydrogenation, 36, 52, 54
- Gas turbines, 34, 38, 102, 122-125, 135, 163-165, 167, 190, 191, 193, 194, 198, 200, 209, 218-221
- Heat exchangers, 102, 122
- Infrared transparent windows, 102
- Radomes, 102
- Rocket nozzles, 123
- Ripple pattern, 33, 42
- Testing, 346, 620, 623
 - Ambient temperature, 7, 79, 103, 123
- Apparatus
 - Dynamic combustor, 165-167, 170, 185, 186, 191
 - Elevated temperature wind tunnel, 124 ff., 131, 134
 - Rotating arm, 124
 - Sand blaster, 7, 8, 79, 103, 105, 123, 138, 140, 149, 162
 - Elevated temperature, 7
 - Standard, 149
 - Two-stage erosion process, 38, 137, 138, 140, 145
- Solid particle impacts (*see also* Single solid particle impact, Solid particle erosion)
- Abrasive (*see* Shape, angular, this heading)
- Chemical stability, 167
- Composites, 336
- Concentration, 32, 78, 200, 212, 213, 218, 220
- Debris, 139
- Density, 14, 38, 86, 118, 200, 217
- Distribution, 8, 79, 168, 173
- Embedding
 - Copper, 10, 14, 15, 18-21, 26, 30, 32, 34, 620
 - Model, 19, 621
 - Reaction bonded silicon nitride, 107, 117, 119
- Flow rate, 34, 50, 124, 149, 168
- Fragmentation, 15, 35, 38, 49, 70, 137, 138, 140-142, 145, 146
- Hardness, 167, 185
- Impact velocity, 14, 22, 35, 37, 50, 60, 62, 67, 86, 103, 115, 124, 132, 133, 137, 138, 140, 149, 168, 169, 194, 197, 199, 204, 208
- Measurement
 - Laser velocimeter, 125, 133, 140, 168, 191
 - Multiple flash photography, 140
 - Rotating disk method, 7, 53, 79, 103, 140, 149
- Impingement angle, 14, 22, 41, 42, 49, 60, 62, 66, 67, 131, 137, 169, 170, 171, 192, 204, 206-208, 212, 216, 217
- Kinetic energy, 38, 63, 67, 71, 185
- Orientation, 76
 - Rake angle, 62, 63, 66-68
- Particle velocity in gas stream
 - Aerodynamic effects, 125
 - Gas velocity, 103, 124, 133, 192
 - Profile, 134
 - Trajectory, 37, 70, 130, 135, 168, 185, 191, 192, 194, 200, 201
 - Fluid flow calculations, 169, 170, 194 ff., 212
- Rebound characteristics, 124, 125, 131, 198-200, 210

- Coefficient of restitution, 207, 208
- Shape, 35, 42, 68, 78, 81, 86, 136, 167, 194
 - Angular, 9, 33, 35, 40-42, 59, 60, 67, 69, 71, 72, 76, 79, 85-87, 109, 118, 125, 136 ff., 140, 165, 178, 187
 - Spherical, 35, 60, 62-64, 67, 71, 72, 85, 86, 136 ff., 147
 - Square plates, 60, 62, 63
- Size, 38, 42, 50, 81, 86, 88, 103, 105, 115, 124, 134, 137, 138, 194
- Strength, 50
- Temperature, 194
- Type
 - Hard, 59, 67
 - Rigid, 38, 39, 55, 59, 65
- Solid particle materials
 - Aluminum oxide, 8, 14, 15, 28, 34, 52, 79, 80, 83-85, 88, 90-97, 149, 152, 167, 168, 173 ff.
 - Cast iron, 83
 - Coal ash, 148, 163-165, 191, 193, 198, 200, 204, 210, 212, 214, 215, 220, 221
 - Coal char, 198
 - Dolomite, 200-202, 210, 212, 217
 - Glass, 60, 68, 69, 83, 88, 346, 348, 368, 374, 375
 - Ice, 368, 398, 399
 - Magnesium oxide, 167, 184, 185, 187
 - Nylon, 346, 350, 368, 374, 375
 - Quartz, 60, 68-70, 72, 83, 85, 103, 104, 106, 107, 109-111, 117, 118, 120, 121, 198
 - Rigid, 363, 368
 - Salt, 165, 172, 185
 - Sand, 590
 - Silicon carbide, 43-46, 52, 57, 60, 68, 70, 83, 85, 88, 89, 101, 103, 104, 106, 107, 109, 110, 117, 118, 122, 133, 210, 212, 213, 218, 220, 221
- Sorbent, 164, 165, 191, 220
- Steel, 60, 64, 83, 85, 88, 89, 138, 139, 141-145
- Sound speed
 - Water, 232-235
 - Waterhammer pressure, 306, 309, 310, 316, 317, 322, 341
- Strain
 - Elastic, 65
 - Hardening, 48, 49
 - Plane, 57, 60, 62, 71, 75
 - Plastic, 21, 22, 65
 - Rate, 48, 50, 65, 72, 74, 323, 325, 410, 415, 418, 421, 422, 425, 427, 430
- Stress waves, 365
 - Acoustic impedance, 104, 117, 228, 250
 - Mismatch, 294
 - Amplitude, 316
 - Attenuation, 336, 337, 363
 - Dilatational, 294
 - Dispersion, 363
 - Duration, 316, 328
 - Elastic-plastic, 366, 373, 374
 - Fiber bundles as wave guides, 365
 - In polymethylmethacrylate, 303
 - Preferred directions in fiber reinforcements, 328
 - Rayleigh, 247, 315, 325
 - Shear, 247, 294
 - Velocity, 257, 430
- Stress wave interactions
 - Flaws, 293, 315
 - Surface scratches, 325
- Submerged cables and pipelines, 582, 592, 594-596, 599
- Surface rippling, 33, 42, 326
- Surface roughness, 34, 35, 405, 444, 445, 499, 503, 506

T

- Target material deformation
- Catering
 - Cavitation erosion, 411
 - Liquid impact, 309
 - Solid particle impact, 12, 15, 25, 39, 42, 62-65, 67-71, 73, 145, 173, 189, 349 ff.
 - Waterjet erosion, 515-519
 - Crushing, 109, 366, 367
 - Cutting, 39-41, 47-49, 53, 60, 62, 63
 - Type I, 62, 63, 67, 68, 70-74
 - Type II, 62, 63, 66-68, 70, 74
 - Elastic, 204
 - Elastic-plastic, 86, 87, 99, 102
 - Penetration, 365, 367, 369, 370, 374
 - Plastic, 72, 89, 109, 113, 118, 119, 122, 204, 322-324, 326, 333, 337, 429, 436, 438, 439, 445, 452, 554
 - Plowing, 15, 39, 60, 62, 63, 67, 68, 70, 71, 73-75
 - Shear, 29, 72, 323, 367, 373
 - Subsurface, 21, 24, 70, 105
- Target materials
- Cavitation erosion
 - Aluminum, 411, 443, 445, 447
 - Armco iron, 436-439, 442, 443, 458
 - Brass, 443, 451
 - Copper-30 zinc, 410, 411, 413, 421, 429, 432, 433
 - Cast iron, 443, 445, 448, 451, 458
 - Cobalt, 410, 424, 429, 430, 432, 433
 - Copper, 411
 - Iron, 410, 415, 418, 424, 427, 429, 430
 - Mild steel, 436-439, 443, 458
 - Monel metal, 435
 - Nickel, 410, 411, 429, 430
 - Nodular graphite cast iron (NGCI), 436-438, 443, 445, 456, 458
 - Hypervelocity particle impacts
 - Carbon-carbon composites, 345, 346, 348, 364 ff.
 - Graphite, 381, 382, 385, 386, 389
 - Material properties, 104, 157-161, 257, 410, 430, 457
 - Solid particle impact
 - Aluminum
 - 1100-0, 41, 43-46, 48, 50, 51, 53-55, 57, 178
 - Al-4.75Cu Alloy, 49
 - Alloy, 56
 - 2024, 52, 132, 198
 - 6061-T6, 138-145
 - Aluminum oxide, 154, 178
 - Aluminum oxide, glass bonded, 101, 104, 105, 107, 112, 114, 117, 119-121
 - Beryllium copper, 52
 - Boron carbide, 153, 156
 - Boron nitride, 154, 156
 - CoCrAlY, 167, 171, 179, 180, 184
 - Copper, 6, 8, 10, 21, 25, 28, 34
 - Annealed, 47
 - Diamond, 154
 - Glass, Pyrex, 77-80, 85, 90-98
 - Haynes 188, 167, 179
 - IN MA-754, 167, 171, 186, 187
 - IN738, 166, 174, 177, 179, 186, 187
 - IN738, aluminide coated, 167, 171, 180, 186, 187
 - Magnesium fluoride, 101, 104, 106, 107, 109, 110, 118-120
 - Molybdenum, 152, 156, 157
 - Nickel
 - Alloy, 52
 - Cobalt alloy, 210, 220
 - Electrolytic, 156
 - INCO 718, 132

- Silicon carbide, 153, 156
 - Silicon nitride, 52, 101, 122, 154, 156
 - Hot-pressed, 102, 104-107, 109-114, 117-121, 167, 171, 184, 186-188
 - Reaction-bonded, 102, 104-107, 109, 111, 113, 114, 119-121
 - Steel, 25, 52, 57
 - AISI 1075, 49
 - 410 stainless, 52
 - Low carbon, 60, 67, 69, 71, 72
 - 17-7PH, 52
 - Type 304 stainless, 165, 210
 - Type 310 stainless, 52-55, 57, 165
 - Stellite, 148, 152, 153
 - Titanium alloy, 52
 - Ti-6Al-4V, 52, 132
 - Titanium carbide nitride, 156
 - Titanium diboride, 156, 157
 - Tungsten, 152, 156, 157
 - Tungsten carbide, 154, 156, 157
 - Udimet 710, 210
 - X40, 167, 179, 186, 187
 - Yttria stabilized zirconium oxide, 167
 - Water drops
 - Gallium arsenide, 255-257, 259, 262
 - Polymethylmethacrylate, 256
 - Zinc selenide, 228, 240, 246, 247, 250, 255-257, 259-262, 340
 - Zinc sulfide, 255-257, 259-263
 - Water jet simulation of single water drop impacts
 - Aluminum, 306
 - Fiber-reinforced thermoplastic polymers, 320, 331 ff., 334
 - Fiber-reinforced thermosetting polymers, 320, 326, 330, 331, 334
 - Glass, 306
 - Calcium aluminate, 314, 315
 - Soda lime, 312, 313, 315
 - Polymethylmethacrylate, 302, 306-308, 340
 - Silicon nitride, 312, 314
 - Thermoplastic polymers, 320
 - Polycarbonate, 322 ff., 339
 - Polyethersulfone, 324, 339
 - Thermosetting polymers, 320
 - Epoxy resins, 325, 335, 339
 - Polyester, 325, 335, 339
 - Waterjets
 - Aluminum, 485, 514, 535, 536, 538
 - Brass, 514
 - Coal, 563, 565, 568, 572
 - Concrete, reinforced, 592, 593
 - Copper, cold-rolled annealed, 514, 515
 - Granite pegmatite, 600
 - Granite-quartz, 600
 - Lead, 515, 525
 - Limestone, 600
 - Norite, 556, 558, 560
 - Polymethylmethacrylate, 536
 - Quartz, biotite, 600
 - Quartzite, 600
 - Witwatersrand, 554, 556, 558, 560
 - Sandstone, 600
 - Berea, 488, 490
 - Steel, 536, 541, 583
 - HY80, 591
 - 1020, 588
 - Tunneling, 512, 553
 - Advantages of waterjets, 600
- ## U
- Underwater jet operations
 - Concrete removal from pipelines, 582, 584, 592 ff., 596
 - Economics, 585, 592, 593

- Metal cutting, 583, 586 ff., 596
- Ship hull cleaning, 584 ff., 595
- Utility construction, 598
 - Advantages of waterjets, 615
 - Environmental impact, 613
 - Pollution control, 613
 - Construction costs, 598
 - Economics, 600, 601, 607, 613-615
 - Operational requirements, 600-605, 607-610, 613
 - Waterjet applications, 598 ff.

V

- Velocity exponent, 42, 58, 65, 67, 78, 83, 88, 89, 99, 106, 117, 118, 120, 138, 140-142, 146, 147, 210, 385, 397, 405
- Vena contracta, 515

W

- Water drop impact (*see* Rain erosion, Single water drop impact)
- Water drop impact testing, 257, 280
 - Ballistic range, 299, 316, 321, 341, 346, 398, 399
 - Rocket sled, 378, 389, 397, 398
 - Rotating arm, 257, 281
 - Waterjet simulation, 299, 309, 316, 321, 341
- Water drops, 346, 350, 368, 374, 375
 - Diameter, 256, 258, 307, 308, 381, 431
 - Formed in waterjets, 515, 525
- Waterhammer pressure (*see also* Hugoniot pressure), 306, 309, 310, 316, 317, 322, 341
- Waterjet
 - Abrasive injection, 583, 588-590, 592, 596

Analysis, 474 ff.

Applications

- Borehole mining of coal, 461, 490
- Cleaning, 563, 582, 583, 600
 - Preferential, 582
 - Ship hull, 584 ff., 595
- Cutting, 473, 474, 480, 513, 544, 553, 554, 562, 563, 583
 - Asphalt, 599
 - Coal, 568, 574, 578, 579, 581
 - Bedding planes, 568, 571
 - Overburden pressure, 565
 - Slot, 568, 569, 571, 573, 575-577, 579
 - Concrete, 592 ff., 596, 599, 600, 615
 - Ice, 599, 615
 - Metal, 586 ff., 596
 - Rock, 300, 490, 598-600, 613-615
- Drag bit cutting augmentation, 553, 560, 561
- Drilling, 562, 563
 - Utility pole holes, 597, 599-602, 610, 612, 615
- Frozen soil excavation, 599, 615
- Heat-exchanger descaling, 582
- Mining, 300, 317, 512, 553, 562, 563, 578, 579, 626
- Trenching, 582, 597, 599-602, 612, 615
- Tunneling, 512, 553, 600
- Uranium mining, 341
- Breakup length, 462, 464, 467, 470, 471, 482, 509, 510, 515
- Cavitating, 513, 525, 529, 532, 536, 549, 562, 563, 566, 569, 572-577, 579, 581
- Coherent, 553
- Continuous, 318, 319, 342, 462, 485
- Cutting effectiveness, 462, 570, 588, 503, 509

- Cutting efficiency,
 - Rate of area cutting, 568, 575, 576, 579
 - Rate of volume removal, 568, 571, 573, 578, 579
 - Kerfing effectiveness, 568, 571, 576, 577, 579
 - Volume removal effectiveness, 568, 577, 579
- Cutting rate, 583, 612
- Damage efficiency evaluation, 513, 520
- Diameter, 495
- Dual orifice, 493, 496, 503, 506, 509, 510
- Erosion augmentation, 513, 592, 625
- Evaluations, 463
- Flow pattern, 535
- Flow rate, 568, 581
- Fluid additives, 583, 589, 591, 592, 596
- Fluid properties, 462
- Impingement angle, 568, 569, 579
- Interacting (jet accumulation), 474, 488, 490
 - Coanda effect, 490
 - Primary jet, 476, 480, 484, 486, 488
 - Secondary jet, 474, 476, 479-481
- Kinetic energy, 479-481, 484, 485
- Lateral outflow jetting, 515, 536
- Mass loss
 - Duration, 529
 - Erosion damage, 515, 521-528, 531, 536, 537, 584, 585
 - Incubation period, 537
 - Material fragmentation, 461, 470
 - Mechanical cutting augmentation, 599, 601, 605, 607
 - Noncavitating, 513, 525, 563, 574-576, 578, 579, 581
 - Operating pressure, 461, 462
 - Penetration, target materials, 525, 529, 536
 - Pressure profile, 474, 494, 497, 498, 509
 - Pulsating, 562
 - Stagnation region, 536, 563
 - Standoff distance, 461, 467, 470, 474, 515, 525, 529, 532, 535, 536, 540, 541, 545, 549, 563, 568, 569, 583, 590, 607
 - Submerged, 513, 531, 590
 - Surface shear stress, 470
 - Test facility, 563, 564
 - Translation velocity, 568, 569, 571, 575, 579
 - Turbulent, 563
 - Underwater operations
 - Concrete weight removal, 592 ff., 596
 - Metal cutting, 586 ff., 596
 - Ship hull cleaning, 584 ff., 595
 - Velocity, 464, 480, 538, 544
 - Augmentation, 480, 486, 490, 491
 - Profile, 474, 482, 494-496, 510